Supersonic Combustion Modelling Using the Conditional Moment Closure Approach

Mark PICCIANI

MRes Final Thesis
Supervisors : Dr. Ben Thornber, Prof. Dimitris Drikakis

Division of Engineering Sciences
School of Engineering
Cranfield University
Cranfield, United Kingdom

2014

Abstract

This work presents a novel algorithm for supersonic combustion modelling. The method involved coupling the Conditional Moment Closure (CMC) model to a fully compressible, shock capturing, high-order flow solver, with the intent of modelling a reacting hydrogen-air, supersonic jet.

Firstly, a frozen chemistry case was analysed to validate the implementation of the algorithm and the ability for CMC to operate at its frozen limit. Accurate capturing of mixing is crucial as the mixing and combustion time scales for supersonic flows are on the order of milliseconds. The results of this simulation were promising even with an unexplainable excess velocity decay of the jet core. Hydrogen mass fractions however, showed fair agreement to the experiment.

The method was then applied to the supersonic reacting case of ONERA. The results showed the method was able to successfully capture chemical non-equilibrium effects, as the lift-off height and autoignition time were reasonably captured. Distributions of reactive scalars were difficult to asses as experimental data was deemed to be very inaccurate. As a consequence, published numerical results for the same test case were utilised to aid in analysing the results of the presented simulations. Due to the primary focus of the study being to assess non-equilibrium effects, the clustering of the computational grid lent itself to smeared and lower magnitude wall pressure distributions. Nevertheless, the wall pressure distributions showed good qualitative agreement to experiment.

The primary conclusions from the study were that the CMC method is feasible to model supersonic combustion. However, a more detailed analysis of sub-models and closure assumptions must be conducted to assess the feasibility on a more fundamental level. Also, from the results of both the frozen chemistry and the reacting case, the effects of assuming constant species Lewis number was visible.

Acknowledgements

First and foremost, I would like to thank my family and friends back home for continuously showing me love and support during the past 17 months of being away. Their patience and understanding of me missing birthdays and family is greatly appreciated. I love you all more than words can describe.

I would like to thank Dr. Ben Thornber, Prof. Dimitris Drikakis, and Dr. Andy Aspden for their guidance, support, and unparalleled knowledge and ideas throughout the duration of my masters. To Charles specifically, I can't even begin to quantify how much you have helped me develop since arriving at Cranfield. If it wasn't for your support, guidance, brain, and our countless discussions, I wouldnt have been able to achieve half of what I have, as quickly as I have. I am forever grateful. I look forward to working with you all in the future.

To my colleagues of F51 and Cranfield: Francis, Charles, Mike, Mudassir, Hernan, Henry, Ramey: You all made the late nights in the office that little bit more tolerable, and the university, that little more enjoyable. Thank you.

Fabio Furlan, you left the university too early. All those late nights in Mitchell Hall watching YouTube videos, head-banging to heavy metal, nights out, and our vacations, were beyond memorable. If it wasnt for those bits of relaxation and laughs, I would have gone insane and lost my mind ages ago.

Charles, Francis, Hernan, thank you for giving me a place to stay the last few months, letting me sleep on your couch, and tolerating me using up one of your communal rooms. Being at home with you guys has provided a great, and much needed distraction in the last few months: cooking/eating together, watching movies, and most importantly, the countless nights screaming at our computers getting owned in BF3/BF4 by 12 year old kids. The most memorable of times hearing Francis scream when his computer would crash, providing hours of laughter at his expense. You all alleviated a major stress by offering me a place to stay when I had none, and for that, I am forever grateful and in you debt.

Contents

List of Figures

List of Tables

CHAPTER 1

Introduction

1.1 Current State of Scramjets

Ramjets and supersonic combusting ramjets (scramjets) primary advantage over conventional air breathing propulsions systems such as turbofans and turbojets is that they have a higher operational velocity (Mach $\sim$ 7). This extends the operating limits of air breathing propulsion into high Mach regimes where other forms of propulsion dominate (i.e rocket propulsion) as shown in Fig. 1.1. The image also shows the performance characteristics of the various propulsion systems. It is clear that ramjets and scramjets offer an alternative to rockets at high Mach numbers, and are the only solution for the air breathing class of propulsion to achieve these high velocities.

However, it is not to say that scramjets overall are more efficient than conventional air breathing systems. As with any form of propulsion, there are specific operational envelopes that each type of engine can operate efficiently within. With all forms of propulsion there are design restrictions based on predicted operating conditions. Both the ramjet and scramjet share similar components (or sections) and the engines themselves are comprised of three main sections as shown in Fig. 1.2; the inlet ramp, the combustor and the nozzle.

Unlike conventional air breathing engines that use a series of compressors to compress the air before combustion, the ramjet class of engines use their forward velocity and a specific inlet geometry to "ram" compress the incoming air as it passes into the combustor. The inlet ramp is designed in such a way that it uses specific geometry to create shockwaves that turn the flow towards the combustion chamber, and compress it. Shockwaves will have different properties depending on the incoming freestream velocity, and it is therefore a crucial design parameter to know the minimum operating Mach number of the jet in order to design an efficient inlet section. The absence of moving parts and active compressors means a much simpler overall engine design. However, the primary issue arising from this is that in order to achieve this ramming effect induced by generated shockwaves, the vehicle (or engine) must have an high initial velocity. With the lack of active engine components this can prove to be nearly impossible, and in order for the engine to achieve/utilise its only form of compression, there must be an additional propulsion system to give it its initial forward velocity. That is why the

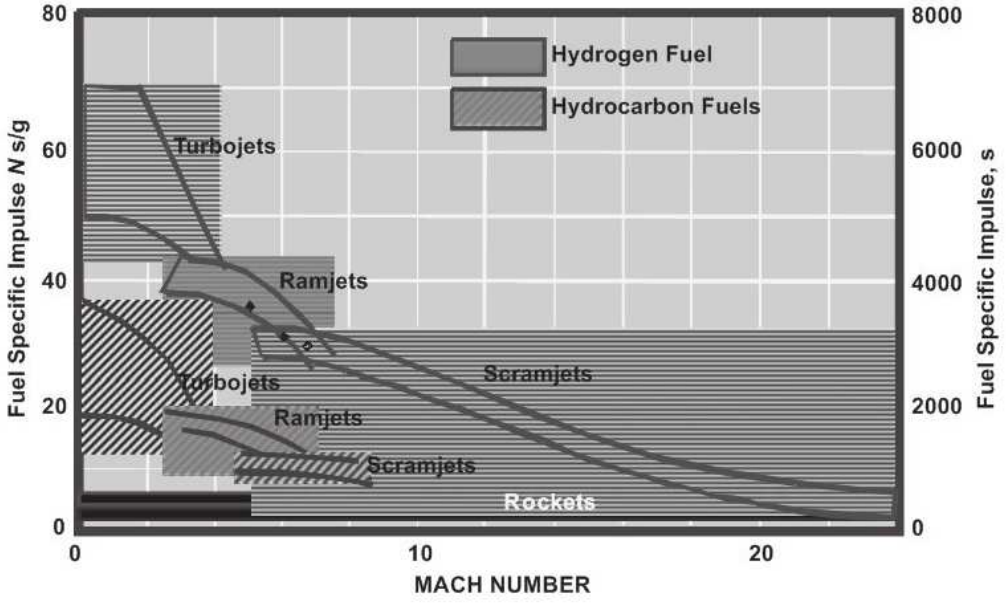

Figure 1.1: Efficiencies of Propulsion Systems [81]

general idea behind ramjets and scramjets is to couple it with another form of propulsion to give the vehicle its initial forward velocity.

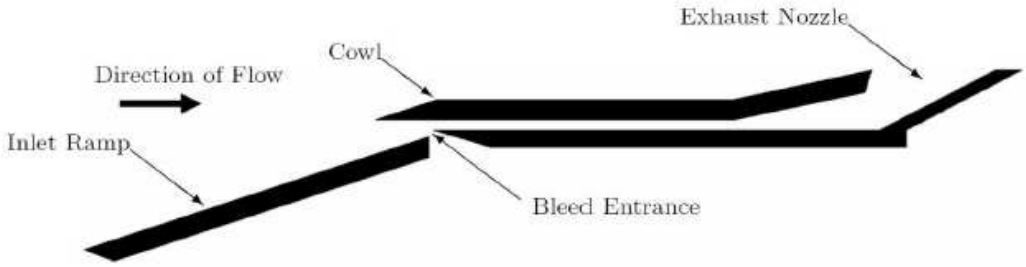

Figure 1.2: Schematic diagram of ramjet and scramjet [77]

One of the main differences between the ramjet engine and the scramjet, is that for the ramjet, which tends to operate at supersonic velocities, the incoming air is diffused to subsonic speeds upon entering the combustion chamber. Consequently, combustion takes place with locally subsonic air. For operation at hypersonic speeds (typically above Mach ~ 5), it is not efficient to diffuse the incoming air to subsonic velocities, therefore the scramjet allows supersonic air to pass into the combustion chamber (typically around Mach ~ 2) and the combustion process takes place with locally supersonic air.

Supersonic flow within the combustion chamber leads to many design issues and challenges. Firstly, due to the high speeds of the flow entering the combustion chamber, the flow residence time within the combustor is on the order of milliseconds. This proves to be a challenge for proper mixing of the fuel and air, and for combustion to occur. As a result of this short residence time, the typical fuel chosen in these engines is hydrogen. It is chosen specifically for its tendency to auto-ignite when exposed to high temperatures such as those already present in the combustion chamber. This avoids the need to incorporate conventional ignition mechanisms such as flame holders which may alter the flow and generate shocks which add unnecessary complications and inefficiencies to an already challenging problem.

1.1.1 Current Scramjet Projects

There have been, and continue to be, many research initiatives taking place all over the world that are attempting to learn more about the processes and physics behind scramjet operation and design. The FALCON (Force Application and Launch from Continental United States) is a joint project by DARPA (Defence Advanced Research Projects Agency) and the United States Air Force (USAF). The first part of the project involved the development of a reusable Hypersonic Cruise Vehicle (HCV). The second part of the project involved the development of a launch system for the HCV to attain hypersonic speeds. The Hyper-X program , headed by NASA, realised the X-43 unmanned hypersonic aircraft. It flew a total of 3 times, of which two of the flights failed. However the third flight in November of 2004, set a speed record achieving Mach ~ 9.65. The X-51 program is a collaboration between Boeing, Pratt & Whitney Rocketdyne, NASA, the Air Force Research Laboratory, and the Defence Advanced Research Projects Agency. The latest launch was in May of 2010 and successfully achieved Mach 5. LAPCAT (Long-Term Advanced Propulsion Concepts and Technologies) is funded by the European Union to develop Air-breathing propulsion systems for hypersonic passenger aircraft and is currently headed by Reaction Engines Limited.

The HyShot project is an initiative from the University of Queensland Australia to understand the relation between pressure measurements made during supersonic combustion in the University of Queensland's T4 shock tunnel, and those obtained in flight. It has developed into a large international project receiving support from Germany, South Korea, Japan, UK, and the USA. To date, there have been a total of 5 launches: HyShot (I-IV) and in 2007 the HyCAUSE. In-flight combustion was realised only in HyShot II and III. The next phase is the Hypersonic International Flight Research Experimentation (HiFire), where the aim of the program is to investigate the fundamental science of hypersonics and its use for future aerospace applications.

1.1.2 High Enthalpy Shock Tunnel Göttingen (HEG)

With the increasing complexity of modern aircraft, and the continually increasing flight speeds, standard wind tunnel testing becomes increasingly difficult. The inefficiency is compounded when breaking into the hypersonic flight range. The extreme temperatures and high pressures

(a) X-34A after release from the B-52B [3]

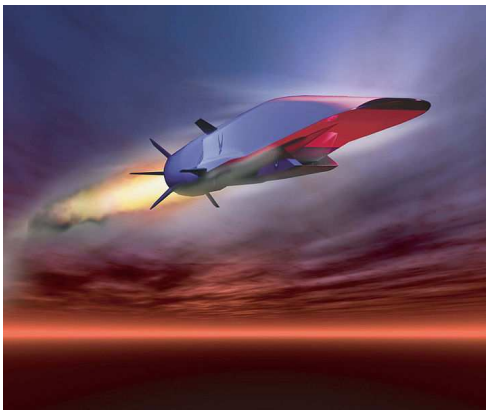

(b) Artists concept of the X-51A [4]

(c) HyShot-II flight test in 2002 [5]

Figure 1.3: Example of Scramjet Projects

are very difficult to recreate without specialized equipment. There only exist a few tunnels that are capable of operating at hypersonic velocities; The T4 Shock Tunnel at the University of Queensland in Australia, the NASA Langley Research Center in Virginia, USA, and the High Enthalpy Shock Tunnel Göttingen (HEG) at the German Aerospace Center (DLR).

The HEG is a free-piston driven shock tunnel and is capable of testing a full geometry scramjet with internal combustion and external aerodynamic effects. HEG has been utilised in numerous space programs and has been linked to many CFD investigations. The investigations ranged from basic aerodynamic configurations in high enthalpy flows, to complex re-entry regimes. HEG is designed to provide a pulse of gas to a nozzle at stagnation pressures of up to 200MPa and stagnation enthalpies of 24MJ/kg.

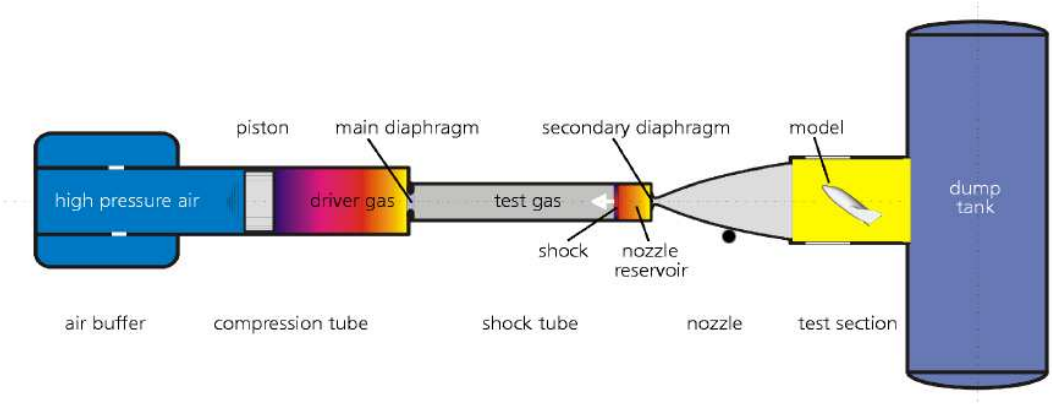

Figure 1.4: Schematic of the High Enthalpy Shock Tunnel in Gottingen [30]

1.2 Problem Description

1.2.1 Previous Studies

The scramjet combustion process is still being scrutinised, and studies have gone into attempting to simulate it. However, most of these simulations have been done and validated using the Reynolds Averaged Navier-Stokes (RANS) approach to turbulence modelling. In order to fully understand the processes that occur within the combustion chamber, flow studies need to be conducted on mixing mechanisms, fuel injection and penetration, and on general flow instabilities. The RANS method of flow modelling is inherently less capable of capturing and resolving instantaneous detailed flow attributes with respect to other methods such as Large Eddy Simulations (LES) for example.

Karl *et al.* [47] stressed the "necessity and urgency of precise validation experiments and of a close link between ground testing, CFD analysis and flight experiments". In 2011, Rana [77] began a study to model the mixing in the combustion chamber of a scramjet using a higher resolution turbulence modelling technique. The study comprised of two main parts:

1. An Implicit Large Eddy Simulation (ILES) case study of a transverse sonic circular jet injection into a supersonic cross-flow (JISC). This was done to validate a digital filter based turbulent boundary condition. The digital filter was analysed against other forms of turbulent data inflow generation methods to view its reliability and suitability. The filter was then used to study the JISC of a single hydrogen jet.

2. An analysis of the full geometry (internal and external) of the HyShot-II scramjet was conducted to get the inflow conditions to the combustion chamber in two dimensions. Once the inflow conditions were determined, they were applied as the inlet conditions in the simulating of a purely mixing (frozen chemistry) three-dimensional (3D) section of the Hyshot-II combustion chamber.

1.2.2 Goals/Objectives for Current Work

In response for a higher fidelity combustion model for scramjet applications, the primary objective of this work is to demonstrate a first approach and validation of a novel algorithm to successfully model supersonic combustion. This is to be achieved through the following steps:

- Validation of a proposed chemical mechanism
- Application of the numerical methods to simulate a inert hydrogen-air mixing case
- Simulate a simple supersonic reacting hydrogen-air jet

Once validated, the code will be used to simulate the flow within the a 3D section of a scramjet combustion chamber. The results can then be compared to the results obtained from the tunnel test at HEG at DLR.

1.2.3 Scientific Challenges

- Model Validation - The combustion model used has been extensively validated in the subsonic regime but not yet validated in the supersonic regime. This becomes problematic as its underlying assumptions, and the sub models used to close certain terms, may not be valid for high speed compressible flows.
- Supersonic Combustion - High speed combustion is a difficult phenomena to model. The chemical reaction time scales become comparable to flow time scales and thus, many assumptions used to model low speed combustion are no longer valid. The increased flow time scales can create combustion instabilities, and potential over-strain of flames can lead to areas of local or complete extinction.

1.2.4 Layout

Chapter 2 will give the reader an overview of the underlying theory behind the study. First, is an introduction to turbulence, where processes and important fundamental characteristics will be developed and explained, followed by a section on common turbulence modelling techniques. Following turbulence, combustion will be introduced to the reader. More emphasis will be placed on the non-premixed turbulent combustion within the chapter, as it is pertinent to the current study. This section will be followed by an overview of the more popular combustion models.

In chapter 3 the numerics and governing equations will be developed. Firstly, an overview of the governing flow equations used within the code will be presented, followed by the outlining of the specific combustion model used. The sub-models implemented within the code that are

used to close the system of equations and model specific terms will then be explained, followed by a discussion of the implemented numerical scheme.

Chapter 4 will present the results of the study, beginning with a frozen chemistry case to assess the implementation, and the mixing behaviour captured by the code and methods. This section is followed by a presentation of the reacting case, where the combustion model will be used and allowed to simulate the supersonic mixing and combustion process of a supersonic hydrogen jet.

CHAPTER 2

Literature Review

This chapter will explain the elementary concepts associated with turbulence. More specifically, the concepts of turbulence that are of more relevance to its modelling in engineering applications will be discussed: The transition of flow to turbulent from laminar, types of turbulent flow such as shear layers, the scales of turbulent, and the idea of energy dissipation in turbulent flows.

2.1 What is Turbulence?

Turbulence exists everywhere. It is rare that everything is laminar and smooth. It is visible in many things and everyday events, yet it is considered to be a normal phenomena and most people don't think anything of it; from doing laps in a pool, to pouring cream in a morning coffee, turbulence is all around. What is not realized is the inherent complexity within turbulent flows. By "definition" turbulence is chaotic, random, and unpredictable. The word definition is used loosely here, because there is no clear idea of what laws turbulence follows and thus, is difficult to define precisely. To better exemplify the chaotic nature of this flow, consider an experiment where the objective is to measure the velocity at a certain point in a field. If the same point in space were chosen as the measurement point, regardless of the number of times the experiment was run, there would be different temporal velocity distributions for every run. This irregularity of the flow means that is is very difficult to model explicitly. Hinze [40] and Davidson [20] both state that the definition and theory of turbulence must be statistical, and is possible to describe only by the laws of probability.

To make the modelling of turbulence easier, the velocity components in all three directions (one dimension considered in the processing example) can be broken down into a mean, and a fluctuating term as shown in Eq. 2.1.

$$u = \overline{u} + u' \tag{2.1}$$

where $\overline{u}$ is the mean velocity, and u' is the fluctuations at a given time. Fig. 2.2 shows a schematic diagram for the time history of a stream-wise velocity component for unsteady turbulent flow. This image depicts the instantaneous mean, and fluctuating velocities associated with this velocity component. The breaking up of the velocity into multiple components is an im-

Figure 2.1: Example of everyday turbulence [6].

portant relationship because certain turbulence modelling methods use this assumption in their construction. More of this is discussed in §. 2.1.3.

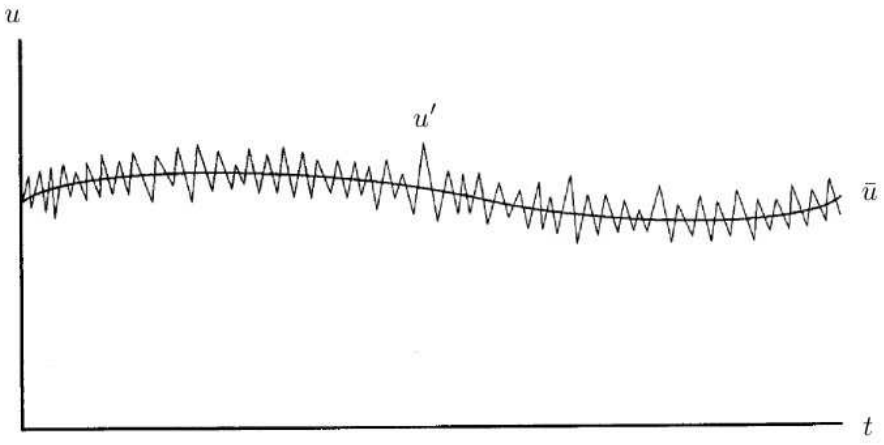

Figure 2.2: Streamwise velocity component at a given location in space for an unsteady turbulent flow.

Turbulence can be broken down into different categories, each with underlying assumptions as to how it behaves [76].

- Homogeneous turbulence, being the simplest and most general, assumes that the turbulence has the same structure in all parts of the flow field. The local velocity fluctuations may be different in the three principle directions (assuming a Cartesian coordinate system), but the respective magnitudes must be constant throughout regardless of spatial position. i.e. $\mathbf{u}'(x_1, t_1) = (1, 2, 3); \mathbf{u}'(x_2, t_1) = (1, 2, 3)$
- Isotropic turbulence is an extension of homogeneous turbulence, however, in the case of isotropic turbulence, there is no directional preference; The velocity fluctuations are the

same in all directions. Similar to homogeneous turbulence, the mean velocity possess no gradient i.e. $\mathbf{u}'(x_1, t_1) = (1, 1, 1); \mathbf{u}'(x_2, t_1) = (1, 1, 1)$

- Anisotropic turbulence, is the most complex method of describing turbulence, but also the most realistic. The statistical features have directional preference and the mean velocity exhibits a gradient.

These classifications are designated to make modelling easier, because in certain flow scenarios the flow can be approximated to have some of the properties previously discussed which makes analysis much simpler.

One of the most important properties in fluid dynamics is the Reynolds number (*Re*). It is defined as the dimensionless ratio between the inertial and viscous forces in the fluid, and has a profound ability to hint at what regime the flow may be experiencing (laminar, transition, or turbulent). It is not definitive that a certain Reynolds number flow will be experiencing a certain flow condition. Depending on the type of flow, the approximate critical Reynolds numbers separating the regimes will be different. The three main classifications of flows are shear layer flows, wall-bounded (boundary layer), and grid-generated turbulence. In this study, only the first will be considered and presented in §. 2.1.1

In certain engineering applications, turbulence is often preferred over laminar flows such as when fluids must be mixed. An important characteristic of turbulence is its ability to transport and mix fluid much more efficiently and rapidly than a comparable laminar flow. In aerodynamic flows (aircraft, automotive etc.), drag is of extreme importance as it is a characteristic parameter in assessing the efficiency of the system in question. In turbulent flows the shear stresses (and hence the drag) are much larger that it would be if the flow were laminar [76]. Therefore, care must be taken into aerodynamic design as to not allow unexpected transition into turbulence.

In order to understand turbulence and how it is formed, the three phases (or processes) must be understood. The first process *production*, is simply the initial process of producing the turbulence. This exact process varies for different flow regimes, but remains the same in the aspect that within the flow you will have formation of eddies of varying scales. Secondly, there is *diffusion*. This process defines the part of the turbulent flow that acts to transport the generated eddies, and thus mass, energy, and momentum, within the fluid. Lastly is the *dissipation* phase. As the eddies become smaller and smaller, eventually the viscous forces becomes larger and dominate consequently dissipating the eddies. The first two phases can also be considered to be part of the transition process from laminar to turbulent flow.

2.1.1 Transition to Turbulence

Returning to the definition of turbulence, Davidson [20] stated that “it is hard to give a definition to what turbulence is, it is better to simply note that when ν[viscosity] is made small enough, all flows develop random, chaotic component of motion”. Although this may not describe *what* turbulence is exactly, it is a very good definition of flow behaviour and its response

to changes in specific properties, with respect to Reynolds number. One of the general ideas behind transitional flow is stability. Several factors affect the transition to turbulence, such as surface roughness, heat transfer, pressure gradient, velocity gradient, and free-stream turbulence. These factors all culminate to produce perturbations in the flow, but what generally determines whether the flow remains laminar or transitions to turbulent, is the ability for the flow to naturally dampen out the excess energy caused by disturbances or instabilities. This is of course a very general stability criterion, but for the sake of explaining the concept behind transition it will be left as such. Based on the Reynolds number definition, assuming we have a low Reynolds number (common for laminar flows) with no additional varying flow parameters, it can be confidently assumed that the viscous forces are dominant and that any small perturbations within the flow will be dissipated. Thus, the flow is "stable". However, in very high Reynolds number flow (which is common for turbulent flows), the inertial forces can be considered to be dominant and thus, the same perturbations presented to the laminar flow *may* cause the flow to become unstable, and thus turbulent. The processes that turns flow turbulent is different for wall bound flows and free-shear flows, the latter is to be discussed in the next section.

Turbulent Shear Layer Flows

For shear flows, instabilities mainly arise from the mean velocity differences at the interface of two parallel flow fields. This instability is known as the Kelvin-Helmholtz (KH) instability. Hoffmann [41] exemplifies this instability by giving an example of two flows at different velocities separated by a splitter plate. When the flows pass the plate and come into contact, the instability occurs. The KH instability in the free shear layer is due to the inviscid characteristics of the flow, and viscosity has little effect on the phenomena [48] as long as it remains low.

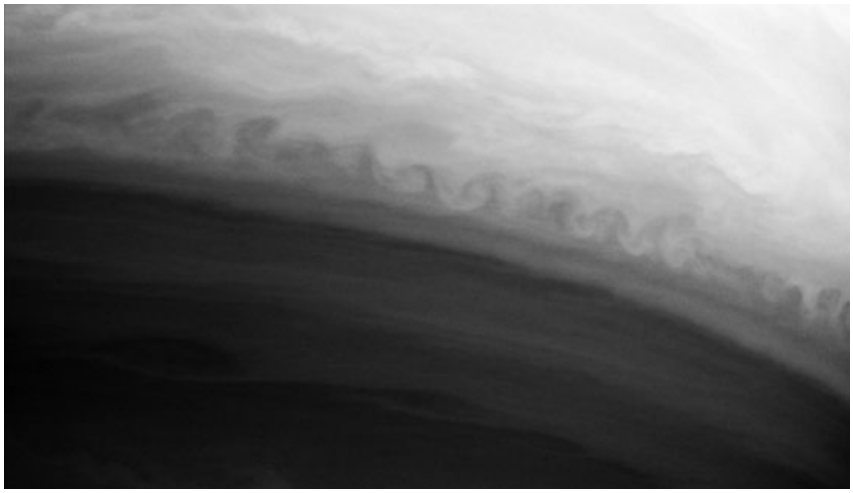

Figure 2.3: Kelvin-Helmholtz instability in the atmosphere of Saturn [2]

The stability criterion of parallel flows can be broken down by the following analysis. Two

parallel flows are given an infinitesimal perturbation, which itself, can be broken down into separate modes. Each mode is analysed to see its effect on the flow interface instability; whether it grows in amplitude, remains stable, or dissipates in time. The instability is defined below by the two modes where s is the instability shape, and k_x is the component of the wavenumber in the direction of the principle velocity. More information along with full detailed analysis can be seen in [25, 85]:

$$s = -ik_x \frac{\rho_1 U_1 + \rho_2 U_2}{\rho_1 + \rho_2} \pm \left[\frac{k_x^2 \rho_1 \rho_2 (U_1 - U_2)^2}{(\rho_1 + \rho_2)^2} - \frac{kg(\rho_1{}^2 - \rho_2{}^2)}{\rho_1 + \rho_2} \right]^{\frac{1}{2}} \tag{2.2}$$

Taking an example of a simple shear layer we can assume a simple case by setting $g = 0$ (gravity). This simplifies the above equation to,

$$s = -ik_x \frac{\rho_1 U_1 + \rho_2 U_2}{\rho_1 + \rho_2} \pm \frac{k_x \sqrt{\rho_1 \rho_2}(U_1 - U_2)}{\rho_1 + \rho_2} \tag{2.3}$$

Eq. 2.3 shows that the KH interface is unstable at all wavenumbers, as s always takes on a positive real component. To further exemplify the instability growth, the assumption of uniform density ($\rho_1 = \rho_2$) can be made to further simplify Eq. 2.3 to yield,

$$s = -\frac{1}{2} ik_x (U_1 + U_2) \pm \frac{1}{2} k_x (U_1 - U_2) \tag{2.4}$$

This form of the equation shows more clearly that the instability grows proportionally to the wavenumber i.e. larger wavenumbers grow more rapidly, and to the initial velocity difference between the parallel flows i.e. larger differences grow more rapidly. Since wavenumber is inversely proportional to wavelength, the instability grows faster for smaller wavelengths than for larger wavelengths.

Fig. 2.4 demonstrates the evolution of the KH instability. It is obvious that the instabilities grow in size with time. As the instabilities grow, they entrain the surrounding flow eventually turning the flow fully turbulent. From Fig. 2.4 it is apparent that the KH instability creates a great deal of mixing within the shear layer and thus, can be extremely beneficial for applications such as combustion where rapid mixing is required. In the case of industrial systems, jets are commonly used to inject fuel into combustion chambers, thus, the primary mechanism for jet breakdown and mixing, are shear layer instabilities. From the above analysis, it would seem that the jet injection velocity has a great influence on mixing and jet breakdown, and by simply tweaking the velocities, the mixing characteristics can be altered significantly. The effect on the initial stream velocities will be demonstrated in the proceeding chapters.

2.1.2 Scales of Turbulence and the Energy Cascade

Turbulence can be considered to be comprised of eddies of different sizes. An eddy is a turbulent motion with a local region of finite size and is a fairly coherent structure. Turbulent flows are generally characterized by a wide range of eddies varying in size and vorticities, and the size

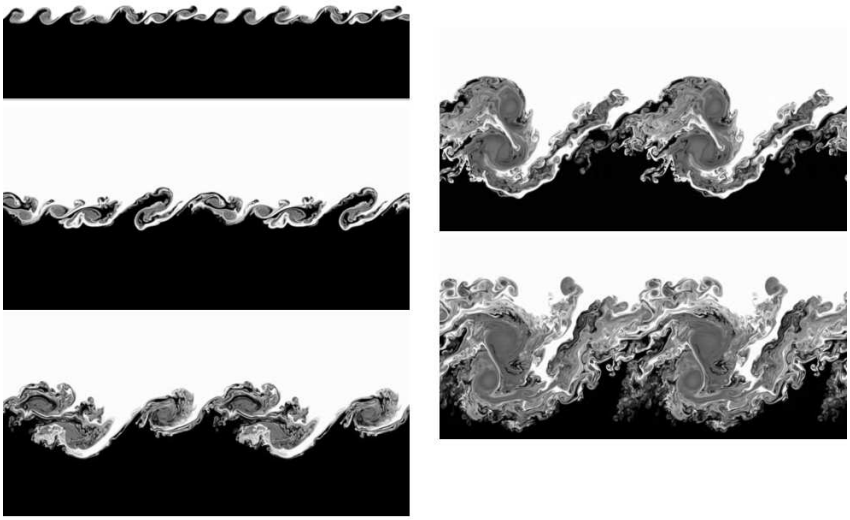

Figure 2.4: Evolution of Kelvin-Helmholtz instability [1].

of these eddies, have distinguishable upper and lower limits. The upper limits of the large eddies is determined mainly by the characteristic length of the problem under investigation, and contain the majority of kinetic energy of the flow. The lower limit is determined by viscosity and typically at these scales, the viscous and molecular effects are dominant [40]. The transfer of kinetic energy from the large eddies to the small eddies is known as the energy cascade.

For homogeneous turbulence, the rate of energy dissipation (ϵ) is estimated to be equal to the rate of energy production by the turbulence. The large scale eddies are assumed to have energy on the order of their specific kinetic energy (u_O^2) where u_O is the characteristic velocity of the same order of magnitude of the mean velocity of the flow. The large eddy length scale l_O, is comparable to the flow scale L. An important parameter for the dissipation, is the time scale of the large eddy (or the turnover time) which essentially represents the lifetime of the eddy. This turnover time is given by $\tau_O = l_O/u_O$. Together, these parameters give the energy dissipation rate,

$$\epsilon = \frac{u_O^2}{\tau_O} = \frac{u_O^3}{l_O} \tag{2.5}$$

This equation shows that the energy dissipation at large scales is independent of viscosity. For the smallest scales, or Kolmogorov scales, length, velocity, and turnover times can be defined as

$$\eta = (\frac{\nu^3}{\varepsilon})^{\frac{1}{4}} \tag{2.6}$$

$$u_\eta = (\nu\varepsilon)^{\frac{1}{4}} \tag{2.7}$$

$$\tau_\eta = (\frac{\nu}{\varepsilon})^{\frac{1}{2}} \tag{2.8}$$

For homogeneous steady turbulence, energy is not created nor destroyed, and therefore through the energy cascade, the dissipation must also equal the rate of transfer to the next scale and so on. This occurs for M scales until finally reaching the Kolmogorov scale. Within the equations previously shown for the Kolmogorov scales, an expression can be obtained for the energy dissipation at this scale to be:

$$\epsilon \sim \frac{\nu u^2}{\eta^2} \tag{2.9}$$

In this case, there is a clear dependence on viscosity at the smallest scales. Through the cascade of energy from one scale to the next, it can ultimately be said that the energy created by the turbulence at the large scales is dissipated by the smallest scales. This again is only for homogeneous steady turbulence where energy is constant. Due to the dissipative nature of flows, if we take unsteady turbulence, without any external energy source, the viscosity effects the of the small scales will eventually decay out the turbulence. The η scale, can be considered as a measure of the dimension of eddies which produce the same dissipation as the turbulence considered. [40]

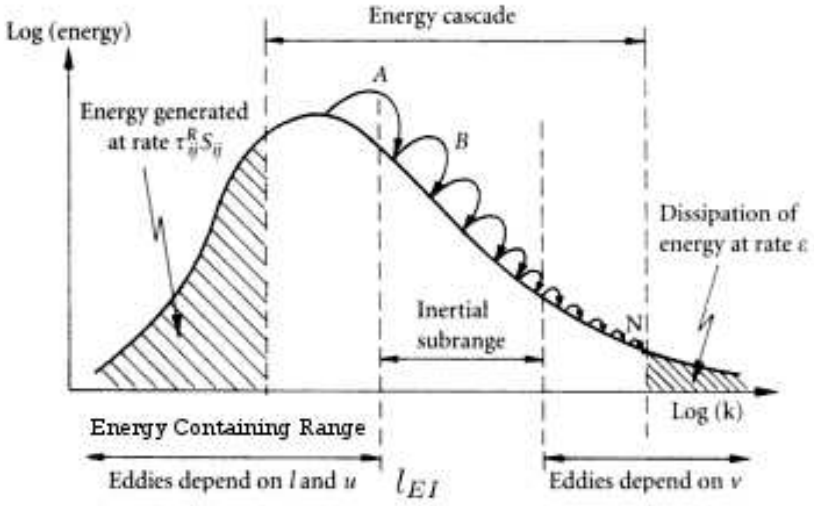

Figure 2.5: Schematic representation of energy cascade [20](Modified).

This process is graphically represented in Fig. 2.5. This figure is known as the energy spectrum, and is commonly used to analyse turbulent kinetic energy. The turbulent scales are commonly represented graphically using their wavenumbers (k). The energy spectrum is divided into two main sections, the Energy Containing Range and the Universal Equilibrium Range. In the Energy Containing Range, the energy is produced by the turbulence and contained in the large eddies. In general, large eddies are anisotropic, and are affected by boundary conditions

of the flow. Kolmogorov argued that all information about the geometry of the large eddies is lost during the cascading process, and that after a certain threshold the eddies were statistically similar in nature. The universal equilibrium range can be defined as the point (or the scale) in which anisotropy of the large eddies ends, and isotropy of the small scales begin. This length scale is given by l_{EI} and is approximated to have a value of $l_{EI} = l_O/6$.

The Universal Equilibrium Range can be divided into two subranges. The Inertial Subrange, and the Dissipation Range. The Dissipation Range is where all the energy of the turbulent flow is dissipated by the smallest scales due to viscous effects. The Inertial Subrange is the portion of the spectrum that contains most of the cascade. Kolmogorov derived an expression for the energy density of the Inertial Subrange given by,

$$E(k) = C\epsilon^{\frac{2}{3}}k^{\frac{-5}{3}} \tag{2.10}$$

where C is universal constant. According to Kolmogorov, the energy cascade follows the same trend upon entering the Inertial Subrange regardless of the geometry and properties of the flow. This has not been proven analytically, but Fig. 2.6 shows the energy density distributions of various experiments of different geometries and properties. This figure shows significant agreement to Kolmogorovs hypothesis.

Returning once again to the definition of Reynolds number, using the aforementioned large scales one would obtain the Reynolds number of the large eddies as $Re_0 = u_0 l_0/\nu$. This Reynolds number is large (comparable to the Re of the flow) so the effects of viscosity are negligibly small. The large eddies are typically unstable and break up, transferring their energy to the smaller eddies. The smaller eddies undergo a similar breakup process, and transfer their energy to yet smaller eddies. This energy cascade continues until the $Re(l) = u(l)l/\nu$ is sufficiently small that the eddy motion is stable, and molecular viscosity is effective in dissipating the kinetic energy. The Reynolds number obtained using the Kolmogorov scales is unity, which demonstrates that the cascade process takes place until the the Reynolds number is small enough for viscous dissipation to become comparable to inertial forces. This illustrates once again, that at the small scales, viscosity is dominant. The small scales can be related to the big scales by,

$$\frac{\eta}{l} \sim Re^{-\frac{3}{4}} \tag{2.11}$$

$$\frac{u_\eta}{u_0} \sim Re^{-\frac{1}{4}} \tag{2.12}$$

$$\frac{\tau_\eta}{\tau_0} \sim Re^{-\frac{1}{2}} \tag{2.13}$$

The relationships above show that the larger the Reynolds number, the smaller the Kolmogorov scales. This has tremendous repercussions when choosing a method to numerically represent a turbulent flows because, as will be discussed in the next section, different methods to model turbulence exist, each with their own underlying assumptions.

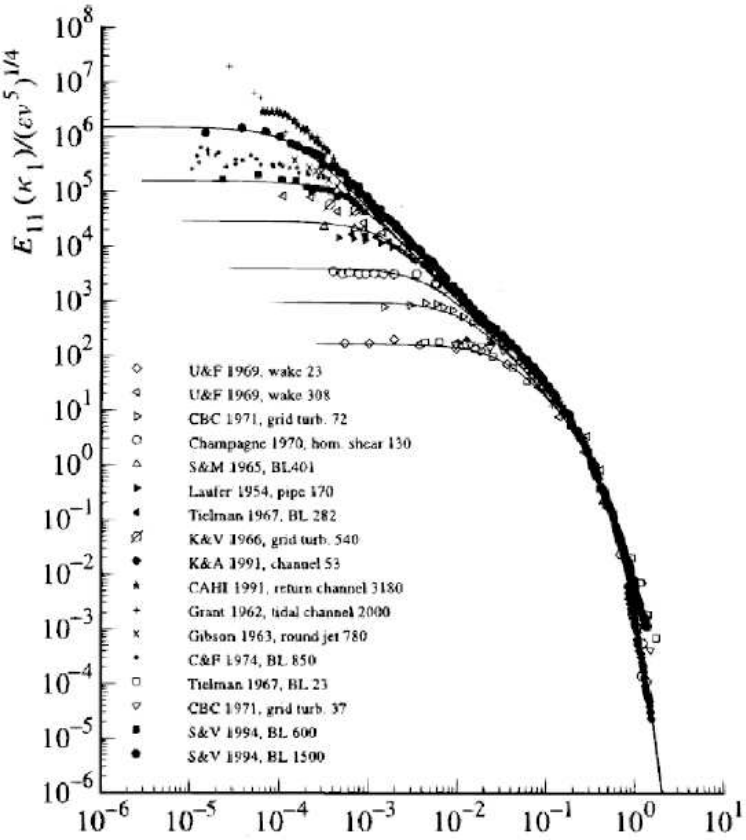

Figure 2.6: Turbulent kinetic spectrum depicting the energy dissipation trends proposed by Kolmogorov [76].

2.1.3 Turbulence Modelling

The three main models for numerically modelling the turbulence effects are *Direct Numerical Simulation* (DNS), *Reynolds Averaged Navier Stokes* (RANS), and *Large Eddy Simulation* (LES). Each of these methods have their own advantages and disadvantages, but the main advantage behind having such a wide range of modelling techniques, is the flexibility to be able to use any of them for a specific application, and a desired accuracy. In this study, a derivative of LES will be used, Implicit Large Eddy Simulation (ILES). In the following section the three main turbulence modelling methods will be described along with their advantages and disadvantages, however, more emphasis will be placed on LES and ILES.

Direct Numerical Simulation (DNS)

In DNS, the governing flow equations are numerically computed directly. This method aims to resolve all scales of turbulence, from the large visible scales all the way to the small Kolmogorov scale. Due to the resolving of even the smallest scale, in order to successfully and accurately

capture these scales, the spatial resolution of the computation must be sufficiently small to capture all the fluctuations. Based on the discussion in §. 2.1.2, specifically Eq. 2.11, we can see that the smallest scale are inversely proportional to the Reynolds number to the power of three quarters. For industrially applicable turbulent flows, Reynolds numbers can be on the order of $10^5 \sim 10^6$, resulting in extremely small Kolmogorov scales. To resolve such small length scales with DNS, the spatial resolution would need to be smaller than the smallest scale. The number of grid points on the computational grid would therefore need to be on the order of $Re^{9/4}$. This means for a Reynolds number of 10^5, the number of grid points would be on the order of 2×10^{11}.

Aside from the spatial resolution of the method, the DNS technique must also have high temporal resolution. In order to maintain accuracy and model the time scales, the temporal resolution must be smaller than the lifespan (turnover-time) of the smallest eddy. From Eq. 2.13 it can be seen that this is also quite small. Coupled together, the total computational time to simulate a reasonable Reynolds number for a short time, could be on the order of months with the current available computing power. Typically, the applications for DNS are limited to low Reynolds flow with simple geometries (periodic). Aside from the tremendous computational cost required by DNS, it is the most accurate form of simulating turbulent flow. It is often used to validate experimental results, or to provide validation data for lower resolution turbulence modelling methods.

Reynolds Averaged Navier-Stokes

RANS is the most commonly used method for simulating turbulence, specifically in industry. The premise behind RANS is the decomposition of variables into mean and fluctuation components with the final solution of the simulation being the time averaged quantity of the flow variables. The process of obtaining RANS from the governing equations (by time averaging) introduces additional unknowns terms that must be modelled. The time averaged results, along with with the addition of submodels to close the system of equations, lends to the fact that RANS is much less accurate than DNS. It should be stressed that the term accuracy in this case, is relative. The accuracy depends highly on the application and the desired results. Another main difference between RANS and DNS is the method in which they solve the flow. In DNS the flow field is resolved, while in RANS it is modelled. This difference comes with the benefit that the grid for RANS can be much coarser than that of DNS which makes it simpler and less computationally expensive. The consequence of this, is that the RANS solution is free of fluctuations and instantaneous flow phenomena. However, resolving of all the turbulent scales down the the smallest, may not be required in many engineering applications, and the mean flow quantities may be sufficient.

Large Eddy Simulation

Between these two extremes of DNS and RANS, there exists a middle ground, LES. The premise of LES is that the large scale eddies (up to predetermined filter size) are resolved while the smaller scales are modelled. Operating as a low-pass filter, the small scales are filtered out of the governing equations to eliminate the necessity to resolve them, and the flow equations only resolve the large scales of turbulence, and model the small scales. The modelling of the small scale eddies comes from equations known as the *subgrid scale* models (SGS) which act as small scale turbulence models for the flow.

The SGS models objective is to close the system of flow equations that generated additional dissipation terms when filtered, and to capture the cascade of kinetic energy through the inertial range (Fig. 2.6). There are many SGS models, but some of the more popular ones are the Smagorinksy, and the Dynamic-Smagorinksy models. The Smagorinksy model gives generally good predictions of dissipation, but tends to break down in transitional flow and near walls. The Dynamic-Smagorinksy model uses a different method to calculate subgrid dissipation, and has been seen to be valid at near wall locations. The formation of SGS models is still an on-going research area and new developments are still being developed. For example, In 2007 You and Moin [61] developed a dynamic global-coefficient SGS. The specific attributes of each SGS model will not be discussed, but as mentioned, different models are better applied in different situations, such as flow near a walls.

Since LES models the small scales, it allows the spatial resolution to be more coarse than DNS. This allows LES to simulate (less accurately) more complex, higher Reynolds number flows for a lower computational cost than that of simulating a similar flow with DNS. Compared to RANS, LES provides a much more accurate solution but at a higher computational cost. However, practically, the main issue with LES is that it was shown to be too dissipative in certain areas, making it difficult to calculate transitional flows or flows with discontinuities. One method to bypass this excess dissipation was to eliminate the SGS models all together. This method is known as the Implicit Large Eddy Simulation (ILES). ILES attempts to utilize the truncation error and the artificial viscosity generated by the numerical scheme in place of the SGS viscosity model that the Classic LES modelling utilises [38]. This method however, has problems of its own. It requires in depth knowledge of the numerical scheme used, more specifically, the truncation error generated. Thornber et al. [87, 88] derived a ILES scheme where they were successfully able to match the dissipation of the numerical scheme to that of the inertial energy cascade. More importantly, excellent agreement between simulations and experimental results was shown in the presence of discontinuities.

2.2 Combustion

Combustion can be considered a collection of chained self-accelerated elementary chemical processes that vary in time scale. It is a temperature dependant, exothermic process between a fuel and oxidant, that utilises the bond energy between molecules to produce heat and light. There are two classifications of combustion:

- **Non-premixed Combustion or diffusion flames**: Normally involving only two streams, the fuel and oxidizer are initially contained separately and brought together for combustion. The flame cannot exist anywhere else except where the two streams meet because on either side of the flame front, the mixture is either too rich or too lean for combustion to occur. At any point in time, the removal of one stream automatically terminates the combustion process. This property makes non-premixed combustion a very safe combustion mechanism. It has been studied extensively and can be seen in many everyday applications such as furnaces, diesel engines etc.
- **Premixed Combustion**: This form of combustion has not been studied as extensively as non-premixed combustion. In premixed combustion, the fuel and oxidiser are not initially separate, but instead, brought together to form a volatile mixture prior to combustion. The process of combustion occurs by the propagation of a flame separating the burnt and unburnt mixtures. In this combustion mechanism, the flame can begin anywhere within the mixture that has a temperature high enough for ignition as mixture already has fuel and oxidizer mixed together in appropriate proportions. This means that practically, this is a much more dangerous mechanism than non-premixed combustion. Many everyday applications exist for premixed combustion such as spark-ignition engines, and gas fuelled turbine engines.

However different the mechanism is for either premixed and non-premixed combustion, both these combustion mechanisms are similar when analysing their higher-level characteristics. They both utilise similar parameters and characteristics to describe the overall efficiency of combustion. Among these characteristics, one of the most important parameters in combustion modelling is the mass fraction. It indicates the total quantity of a specific chemical species within a mixture. The mass fraction is given by,

$$Y_k = \frac{m_k}{m} \tag{2.14}$$

where m_k represents the mass of a chemical species k, and m is the total mass of the mixture. Extending beyond this concept, the total amount of fuel and oxidizer in a system have a great effect on the combustion characteristics. However different premixed and non-premixed combustion are, the similarity between any chemically reacting systems is the amount of respective fuel and oxidizer for an ”ideal” combustion process. This ratio is known as the stoichiometric ratio. Considering a chemical reaction, the ratio between the oxidizer (O) and the fuel (F) is the

stoichiometric ratio, and is given by,

$$s = \left(\frac{Y_O}{Y_F}\right)_{st} \tag{2.15}$$

In reality, the mixture of fuel and oxidizer will not always exist in stoichiometric proportions, and therefore it is convenient to define a different ratio that relates the actual mixture ratio present, to the stoichiometric ratio. This relationship is known as the equivalence ratio. The equivalence ratio for the premixed regime (denoted by subscript p) is

$$\phi_p = s\frac{Y_F}{Y_O} = s\frac{\dot{m}_F}{\dot{m}_O} \tag{2.16}$$

and for non-premixed (denoted by a subscript np)

$$\phi_{np} = s\frac{Y_F^1}{Y_O^2} \tag{2.17}$$

$$\phi_{np_g} = s\frac{\dot{m}_F}{\dot{m}_O} \tag{2.18}$$

As previously mentioned, for non-premixed combustion, the oxidizer and fuel are kept separately and only brought together for mixing and combustion. It is not said that the stream of either is pure fuel or oxidizer, and thus, Y_F^1 and Y_O^2 in Eq. 2.17 represent the mass fractions of fuel and oxidizer in the respective streams. The physical significance of the equivalence ratio is to indicate the quality of the mixture. When the equivalence ratio is $\phi < 1$ the mixture is said to be lean (excess oxidizer) and when $\phi > 1$ the mixture is said to be rich (excess fuel).

2.2.1 Non-Premixed Combustion Characteristics

Laminar Diffusion Flames

In the proceeding section, aspects of diffusion flames will be discussed as they are the most pertinent to the study. Before the extension to turbulent combustion, an analysis of a simpler case such as laminar flames must be undertaken. The structure of a diffusion flame is shown in Fig. 2.7.

- Far away on each side of the flame, the gas is either too rich or too lean to burn. Reactions only occur when both the fuel and oxidizer are mixed adequately; The ideal case being when they are mixed in stoichiometric proportions. The flame normally lies along the points where this ratio is met.
- Diffusion flames do not have a reference “speed”. The flame does not propagate towards either fuel or oxidizer stream because of the lack of the other (either fuel or oxidizer) deep in either non-mixed stream. This means that the flame does not move significantly within the flow field and thus, is more susceptible to perturbations and turbulence.

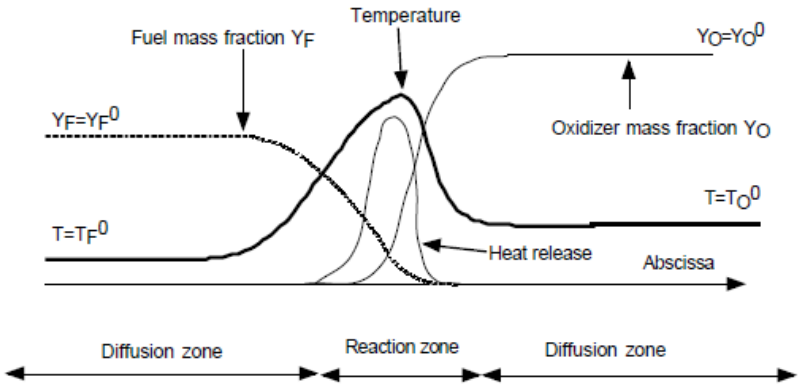

Figure 2.7: Diffusion flame structure [75].

- Unlike premixed flames, diffusion flames do not have a reference thickness; strain is required to drive fuel and oxidizer together. Without the presence of strain, a diffusion flame will stretch (thicken) and eventually dissipate.

In non-premixed combustion, there are different classes of combustion models. The most popular are conserved scalar methods. In these methods it is common to analyse flame structure with respect to z-space. This z-space (or the mixture fraction) allows the flame in question to be analysed for the respective amounts of oxidizer and fuel using a single parameter. The mixture fraction is commonly represented by,

$$z = \frac{sY_F - Y_o + Y_o^0}{sY_F^0 + Y_o^0} \tag{2.19}$$

From this definition of mixture fraction, the boundary conditions can determined as follows.

1. The value of z in the fuel stream is 1; conversely z is 0 in the oxidizer stream
2. The temperature at $z = 0$ and $z = 1$ are respectively the initial temperature of the oxidizer and fuel respectively. The temperature is maximum at the point where $z = z_{st}$ where ”st” denotes the stoichiometric point.
3. The initial mass fractions of both oxidizer and fuel is equal to their mass fraction present in their respective streams prior to mixing.

Chemistry

With respect to the chemical reactions that lead to the combustion process, there are certain classifications and characteristics that can be assigned to the elementary reactions that describes its chemical behaviour. Firstly is the *reversibility* of the reaction. Irreversible reactions mean

that the reaction can proceed only in the forwards direction, and that the reverse reaction does not take place i.e reactants are converted into products only. Conversely, reversible reactions are the opposite, signifying that the reaction can also proceed in the reverse direction as well. The second characteristic is the "speed" of the reaction. Equilibrium or "fast chemistry" assumes that the chemical times (chemical reaction times) are extremely short and that they are smaller than all other flow characteristics; the reaction happens instantaneously.

When dealing with a reacting problem, there can exist any combination of the aforementioned assumptions. The irreversible fast chemistry (equilibrium) assumption is the idealised solution, and is often implemented to give the bounds to the solution of the specific reacting problem. What is important in this assumption, is that the fuel and oxidizer cannot exist at the same time in a specific point in space. The solution to the irreversible fast chemistry assumptions is the idealised case, and is known as the Burke-Shaumann [14] flame structure. Conversely, the opposite extreme is finite rate, reversible chemistry. This corresponds to actual combustion conditions, but as a consequence, is the most complex to model.

When entering into the finite rate chemistry regime, the chemical time scales may no longer be the dominant time-scales in the flow and flow time-scales must be considered. It is therefore suitable to define a parameter that describes the dominance of one time-scale (or process) with respect to another. This parameter is known as the Damköhler number,

$$Da = \frac{\tau_f}{\tau_c} \tag{2.20}$$

where τ_f is the flow time and τ_c is the chemical time. As an example, when equilibrium chemistry is assumed, the Damköhler number tends towards infinity, however, when Da takes on finite values, the flame is taking on finite chemistry characteristics, and the flow time-scales are becoming comparable to the chemical.

Without going into too much detail at the moment in regards to the reasons behind the behaviour, Fig. 2.8 shows the structure of the Burke-Shaumann solution to that obtained from finite rate chemistry for a irreversible process.

In this figure, the mixing line denotes the extreme state where fuel and oxidizer would mix without reaction, and is important when considering ignition or quenching problems or behaviour. The other extreme case, is the upper-bound equilibrium lines which correspond to states where reaction occurs with infinitely fast chemistry. At any given location in a reacting problem, the temperature at a given mixture fraction will be somewhere in these bounds. When most of the points are located near the mixing lines, it means the flame is almost extinguished, or has not yet ignited. On the contrary, if most most of the points are located near the equilibrium lines, it indicate vigorous flames.

It is clear that there is a difference between the ideal combustion and finite rate chemistry as seen in Fig. 2.8. The total temperature is seen to decrease slightly and the "consumption" of both species extends slightly beyond the stoichiometric point. These discrepancies occur with finite rate chemistry because of the diffusion of reactants past the stoichiometric flame region which, for infinitely fast chemistry does not occur. The occurrence of this "leakage"

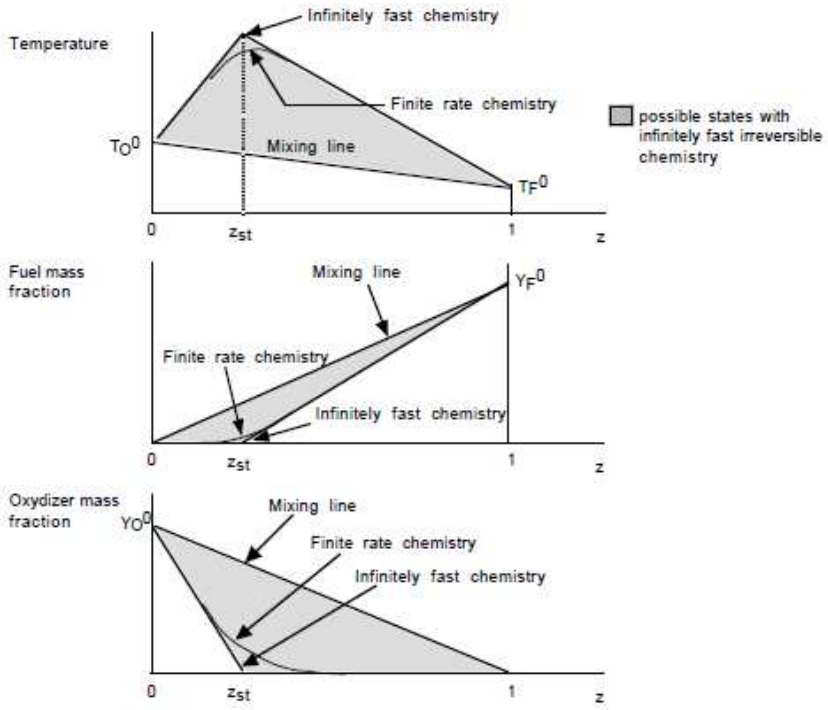

Figure 2.8: z diagram of finite rate chemistry compared to equilibrium chemistry [75].

of one species into the other is a direct consequence of the strain on the flame, or the scalar dissipation. This leakage causes the reaction zone to go from being infinitesimally small to having a certain width. A higher strain (or scalar dissipation) results in a wider reaction zone and a lower maximum temperature. The extreme case is where the strain is too high and the flame is quenched resulting in the distributions tending towards the mixing line. The effect of increased strain is further illustrated in Fig. 2.9.

When attempting to calculate the Damköhler number, because the flow times (τ_f) are generally hard to describe and quantify within the flows under investigation, a common assumption is that flow time (τ_f) is inversely proportional to the scalar dissipation at the stoichiometric point. As a consequence of this assumption, and through its definition, the Damköhler number is inversely proportional to the scalar dissipation at the stoichiometric point.

Strain and Scalar Dissipation

The last point above leads to an important way of describing the flame behaviour. Without strain a flame will not be steady. Strain acts to push reactants towards the flame and without it (or too much) the flame will inevitably dissipate and extinguish. Directly connected to this strain, is the scalar dissipation. Through z-space analysis, the scalar dissipation can be represented by Eq. 2.23.

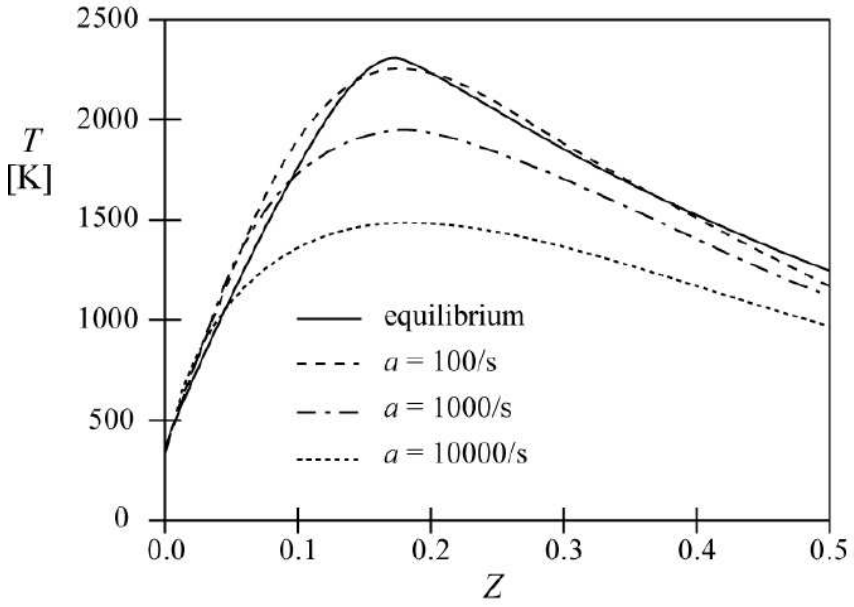

Figure 2.9: Effect of increased strain on flame structure [71].

$$\chi = 2D(\frac{\partial z}{\partial x_i}\frac{\partial z}{\partial x_i}) \tag{2.21}$$

For the process of understanding the relationships, a steady strained one-dimensional diffusion flame with infinitely fast chemistry and constant density will be assumed. With this assumption the scalar dissipation can be written in terms of the strain rate a by,

$$\chi = 2D(\frac{\partial z}{\partial x_i}\frac{\partial z}{\partial x_i}) \approx \frac{a}{\pi}\exp(-\frac{a}{D}x_1^2) \tag{2.22}$$

What must be taken from the the above equation is the manner in which the scalar dissipation rate is related to the strain rate. The value a/π signifies the maximum possible scalar dissipation. The strain rate a, is constant and dependant on the flow characteristics, more specifically the velocity gradients. The scalar dissipation on the other hand, depends on the the velocity gradients as well as the spatial location. It measures the mixture fraction gradients as a consequence of the strain.

$$\chi = \frac{a}{\pi}\exp[-2(\mathrm{erf}^{-1}(\frac{\phi-1}{\phi+1}))^2] \tag{2.23}$$

Chemical Schemes

There exist many degrees of modelling combustion mechanisms. Complete chemical mechanisms may consist of hundreds of elementary chemical reactions, and modelling them all may

be too expensive. It must be considered that within the CFD regime, at every cell, it is required to solve the governing flow equations for every species, along with every elementary reaction in the mechanism. With hundreds of mechanisms and with many species, this could prove to be too computationally expensive for grids required to resolve detailed flow phenomena. To avoid this high computational cost, reduced mechanism have been proposed ranging from 33 reactions [45], down to 4 [15] and even as far as 2 [69].

Reaction[b]	A	n	E
(1) $H_2 + O_2 \rightarrow OH + OH$	1.70×10^{13}	0	48 000
(2) $H + O_2 \rightarrow OH + O$	2.60×10^{14}	0	16 800
(3) $O + H_2 \rightarrow OH + H$	1.80×10^{10}	1.00	8 900
(4) $OH + H_2 \rightarrow H_2O + H$	2.20×10^{13}	0	5 150
(5) $OH + OH \rightarrow H_2O + O$	6.30×10^{12}	0	1 090
(6) $H + OH + M \rightarrow H_2O + M$	2.20×10^{22}	−2.00	0
(7) $H + H + M \rightarrow H_2 + M$	6.40×10^{17}	−1.00	0
(8) $H + O + M \rightarrow OH + M$	6.00×10^{16}	− .6	0
(9) $H + O_2 + M \rightarrow HO_2 + M$	2.10×10^{15}	0	−1 000
(10) $HO_2 + H \rightarrow H_2 + O_2$	1.30×10^{13}	0	0
(11) $HO_2 + H \rightarrow OH + OH$	1.40×10^{14}	0	1 080
(12) $HO_2 + H \rightarrow H_2O + O$	1.00×10^{13}	0	1 080
(13) $HO_2 + O \rightarrow O_2 + OH$	1.50×10^{13}	0	950
(14) $HO_2 + OH \rightarrow H_2O + O_2$	8.00×10^{12}	0	0
(15) $HO_2 + HO_2 \rightarrow H_2O_2 + O_2$	2.00×10^{12}	0	0
(16) $H + H_2O_2 \rightarrow H_2 + HO_2$	1.40×10^{12}	0	3 600
(17) $O + H_2O_2 \rightarrow OH + HO_2$	1.40×10^{13}	0	6 400
(18) $OH + H_2O_2 \rightarrow H_2O + HO_2$	6.10×10^{12}	0	1 430
(19) $M + H_2O_2 \rightarrow OH + OH + M$	1.20×10^{17}	0	45 500
(20) $O + O + M \rightarrow O_2 + M$	6.00×10^{17}	0	−1 800
(21) $N + N + M \rightarrow N_2 + M$	2.80×10^{17}	− .75	0
(22) $N + O_2 \rightarrow NO + O$	6.40×10^{9}	1.00	6 300
(23) $N + NO \rightarrow N_2 + O$	1.60×10^{13}	0	0
(24) $N + OH \rightarrow NO + H$	6.30×10^{11}	.50	0
(25) $H + NO + M \rightarrow HNO + M$	5.40×10^{15}	0	−600
(26) $H + HNO \rightarrow NO + H_2$	4.80×10^{12}	0	0
(27) $O + HNO \rightarrow NO + OH$	5.00×10^{11}	.50	0
(28) $OH + HNO \rightarrow NO + H_2O$	3.60×10^{13}	0	0
(29) $HO_2 + HNO \rightarrow NO + H_2O_2$	2.00×10^{12}	0	0
(30) $HO_2 + NO \rightarrow NO_2 + OH$	3.40×10^{12}	0	−260
(31) $H + NO_2 \rightarrow NO + OH$	3.50×10^{14}	0	1 500
(32) $O + NO_2 \rightarrow NO + O_2$	1.00×10^{13}	0	600
(33) $M + NO_2 \rightarrow NO + O + M$	1.16×10^{16}	0	66 000

Figure 2.10: Example of chemical reaction scheme consisting of 33 reactions for H_2, with N_2 chemistry [45].

The elementary reactions can be broken down into 3 categories [37]: Chain initiating step, chain carrying or propagating steps, and chain terminating step. This three step definition of a reaction mechanism implies that the process of combustion is initiated by a single step, specifically the one that produces radicals. At low temperatures, this step (or reaction) is usually determined by the elementary reaction that has the lower activation energy, and tends to be highly endothermic and very slow. Conversely, the chain reaction mechanisms have a low activation energy, and are important because they determine the overall reaction propagation rate. Eventually, after a certain amount of intermediate chain reactions, the process is terminated by the recombination of radicals, or when a radical combines with a molecule to give products of lower activity that cannot propagate the chain.

The dominance of certain elementary reactions over other depends on a few factors: the activation energy, and overall temperature of the system. Both these factors affects the reaction

rate which is modelled by the Arrhenius Law.

$$k = AT^n \exp\left(\frac{-E_a}{RT}\right) \tag{2.24}$$

where R is the universal gas constant, T is the temperature, n is the temperature exponent, and A is the pre-exponential factor. The temperature exponent and pre-exponential factor are both determined by experiments and are known to be highly dependant on temperature.

In order to determine the global effect of specific reactions, often a sensitivity analysis is conducted on chemical schemes. Sensitivity analysis is fairly straight forward and involves scaling the reaction coefficients and observing the changes in combustion characteristics. Therefore, the basic idea of a reduced mechanism is the elimination of reactions that produce negligible influence on the overall combustion process. This is a valid assumption as long as the overall combustion mechanism proposed is still representative of the original process. Computationally, reduced mechanisms are used as approximations and to enhance computing efficiency, and may used when not describing the full mechanism is not required. The number of equations used to model the reaction depends on the application, and to what extent the chemical features want to be modelled [15].

Turbulent Diffusion Flames

The laminar flamelet (LFA) is a common method to model combustion using z-space and has the fundamental assumption that combustion is the ensemble of laminar flames occurring at the smallest scales. Based on this description, another assumption in its formulation is that the $Da >> 1$. However, is was shown that as the flow times-scales decrease (as occurs in turbulent flows), Da begins to deviate from is very large value and approach unity. To study the effect of turbulence on non-premixed combustion, Cuenot and Poinsot [19] conducted a DNS study of flame-vortex interaction utilising the popular flamelet model. This was study was conducted to study the validity limits of the laminar flamelet assumption (LFA) at different turbulence levels. The aim was to propose a diagram (Fig. 2.11) for possible turbulent non-premixed combustion regimes, similar to those present for premixed.

Four regimes and two transition Damköhler numbers, D_a^{LFA} and D_a^{ext} were identified by the study [75].

- Case A in Figure Fig. 2.11 corresponds to very large Damköhler numbers. In this regime, LFA applies, and the inner structure of the flame is unaffected by the vortices.
- Case B shows strong curvature of the flame front, and molecular and heat diffusion along the tangential direction to the flame front must be considered.
- for Case C, the chemical time becomes non-negligible compared to the vortex characteristic time. The chemistry is not fast enough to be accurately modelled by the LFA and unsteady effects are become noticeable. In this regime, the evolution of the flame is delayed compared to the evolution of the flow.

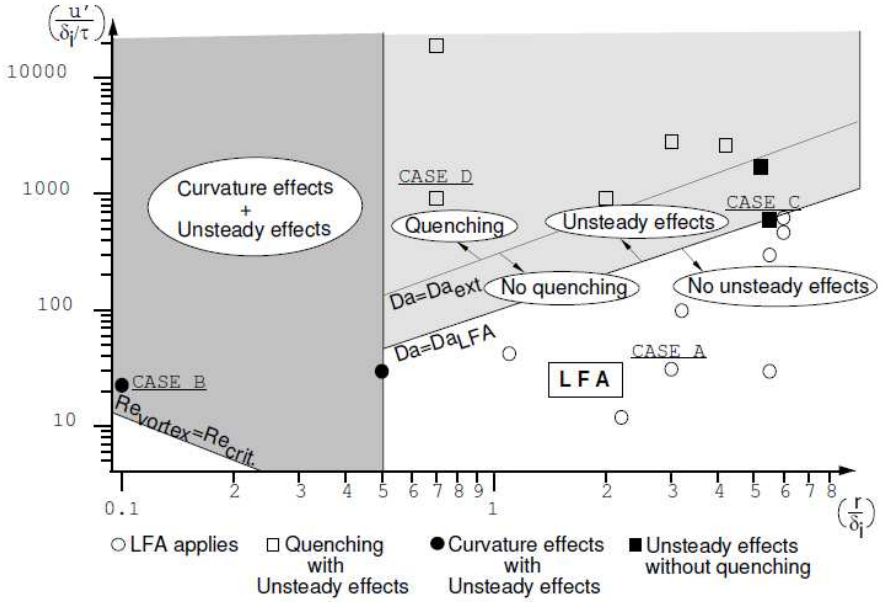

Figure 2.11: Laminar diffusion flame vortex interaction spectral log-log diagram [19] plotted versus velocity and length scale ratios of the vortex and flame.

- In case D, the Damköhler number is very small, and the strain induced on the flame by the vortex is too strong. In this regime extinction occurs, but was evidenced to occur at a lower Damköhler number than expected from flamelet libraries.

Vervisch and Veynante [92] provide a similar diagram, with explicit reference to the turbulent Reynolds number and the Damköhler number (Fig. 2.12).

The one difficulty of turbulent diffusion flames is the inability to confidently define its scales, even if there are definitions for them. Non-premixed flames have no intrinsic length scales, and strongly depend on highly fluctuating local flow conditions such as strain rate. This is the primary difference (and difficulty) between premixed and non-premixed turbulent combustion, and is also a reason why the diagrams presented above should be used with care, and more as a guide; they neglect to model precise local phenomena that can be different at various locations within the flow.

Nevertheless, two length scales can be introduced for the flame region. The diffusion layer thickness l_d is the thickness of the zone where the mixture fraction changes indicating reactants mixing.

$$l_d \approx \sqrt{\frac{D_{st}}{\widetilde{\chi}_{st}}} \tag{2.25}$$

where $\widetilde{\chi}_{st}$ denotes the conditional scalar dissipation rate for $z = z_{st}$ and theD_{st} represents the molecular diffusivity on the stoichiometric surface. The second length scale is the reaction zone thickness l_r. This quantity corresponds to the region where the reaction rate is non-zero.

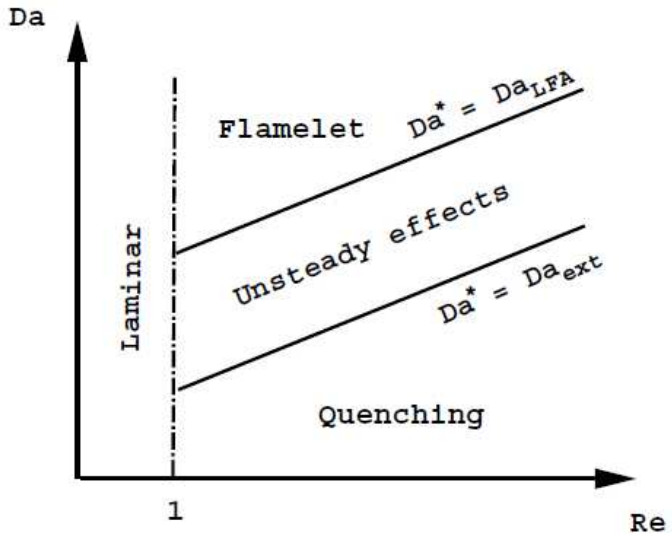

Figure 2.12: Schematic of non-premixed turbulent combustion regimes as a function of Da and the turbulent Reynolds number [92].

Similar to the laminar diffusion flame case, the flow time scales can be approximated as the inverse of the scalar dissipation as seen in Eq. 2.26. The scalar dissipation is replaced by its conditional counterpart leading to

$$\tau_f \approx \frac{1}{\widetilde{\chi}_{st}} = \frac{l_d^2}{D_{st}} \tag{2.26}$$

thus the Damköhler number becomes

$$D_a^{fl} = \frac{\tau_f}{\tau_c} \approx (\widetilde{\chi}_{st}\tau_c)^{-1} \tag{2.27}$$

Turbulent Combustion Modelling

The main objective of combustion modelling is to close the system of equations for the mean reaction rates. Veynante and Vervisch [92], summarise three main physical approaches to model turbulent combustion.

- **Geometrical analysis** - The flame front is defined as the geometrical surface evolving in the turbulent flow field. It can be related to the total surface covered by the flame during combustion (flame brush), but is more often linked to an instantaneous iso-surface mixture fraction and is usually combined with flamelet assumptions.
- **Turbulent mixing** - If the assumption is made that the chemical time scales are shorter than turbulent time scales, then the mean reaction rate is controlled by the mean turbulent

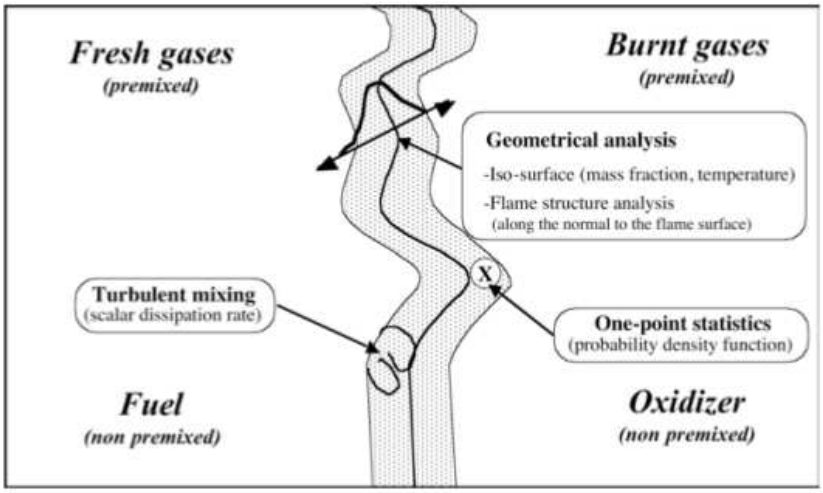

Figure 2.13: Modelling approaches for turbulent combustion [92].

mixing rate which can be approximated by the scalar dissipation rate. The most popular models are the Eddy-Break-Up and Eddy Dissipation Concept.

- **One point statistics** - The most general of the modelling approaches, is based on the joint Probability Density Function (PDF). No flame structure assumption is required and it closes the mean reaction rate by combining instantaneous reaction rates given by the Arrhenius law, with the joint PDF of the thermodynamic variables.

2.2.2 State of the art in Non-Premixed combustion Modelling

In the previous section, combustion characteristics were described. In the proceeding section, a more detailed description of popular models will be given. As the current work deals with LES, the models that will be described will be done so with the underlying implementation to LES. However, for non-premixed combustion, the models used are simply extensions of their RANS counterparts. The three more popular combustion models are the probability density function (PDF) transport models, the Flamelet models, Linear Eddy model, and the relatively new Conditional Moment Closure (CMC).

PDF Transport Models

The main idea behind the PDF approach is that the mean reaction rates are determined as a function of the instantaneous reaction rates, and the PDF. The PDF, that describes every point in the flow field, is a unique description of fluctuating turbulent field, and contains all the necessary information. The instantaneous reaction rates, on the other hand, can be a function of a number of thermochemical variables. The general formulation of this approach is given below.

$$\overline{\dot{\omega}}_k = \int_{\phi_1} \dots \int_{\phi_k} \dot{\omega}_k \left(\phi_1 \dots \phi_k\right) p\left(\phi_1 \dots \phi_k\right) d\phi_1 \dots d\phi_k \tag{2.28}$$

where ϕ_k represents a thermochemical parameter, $\dot{\omega}_k$ is the instantaneous source term of species k calculated via the chemical mechanism, $p\left(\phi_1 \dots \phi_k\right)$ represents the joint probability density function conditioned on k thermochemical parameters, and $\overline{\dot{\omega}}_k$ represents the source term in a closed form. The primary difficulty in this approach is determining the joint-PDF, as the dimensionality of the PDF, scales with the number of independent thermochemical parameters. There are currently two approaches to this problem. The first is by assuming a PDF shape, and the second is where a modelled conservation equation of the joint-pdf is solved.

Presumed PDF

A PDF can take on any shape, and contains information about the mean and higher order moments of a variable. In combustion applications, PDF functions have displayed common features which lends to an assumption that a PDF could possibly be described using a limited number of variables. Williams [94] proposed that the shape of the PDF is fixed, and parametrised by the first and second moments of the variable in question. This is a popular method, and has been used in a variety of combustion studies [59, 91]. For single composition PDF's the most popular shape is defined by the β-PDF.

$$f(x;\alpha,\beta) = \frac{x^{\alpha-1}(1-x)^{\beta-1}}{\mathrm{B}(\alpha,\beta)} = \frac{\Gamma(\alpha+\beta)}{\Gamma(\alpha)\Gamma(\beta)} x^{\alpha-1}(1-x)^{\beta-1} \tag{2.29}$$

Where $\mathrm{B}(\alpha,\beta)$ is the beta function defined by

$$\mathrm{B}(\alpha,\beta) = \int_0^1 x^{\alpha-1}(1-x)^{\beta-1}\, dx \tag{2.30}$$

and $\Gamma(z)$ is the gamma function.

$$\Gamma(z) = \int_0^\infty t^{z-1} e^{-t}\, dt \tag{2.31}$$

The presumed PDF approach provides good results when there is only one parameter in question. Its usage carries the underlying assumption that the species production rates are dependant only on one quantity (typically the mixture fraction). In reality, the source term is dependant on more than one parameter, and therefore it is common to approximate the thermochemical variable joint-PDF as being statistically independent. Taking an example of mixture fraction, and temperature, the joint-PDF can be rewritten as,

$$p(z,T) = p(z)p(T) \tag{2.32}$$

where in this case, the PDFs of each thermochemical variable can be constructed independently. This is a better assumption than using a single parameter, however this method still falls short of the true behaviour and accurate modelling requires constructing a multi-dimensional joint-PDF.

PDF Method

A less practical method (but more accurate) when dealing with multiple parameters, involves solving an exact balance equation (a transport equation) for the joint-PDF. The main attraction to the balance PDF equation, is that the chemical source term is closed within it and depends only on the chemical variables, therefore it does not need to be modelled and can handle any complex chemical schemes. Also, this method provides all the higher moments of the flow, whereas most other approaches provide only mean values.

The main drawback of this modelling method is that it is extremely expensive. It has been made slightly more efficient by using Monte-Carlo simulations, however its applicability still remains within the research community. Additionally, there also remains unclosed terms which are difficult to model, specifically the molecular diffusion which requires additional length scale information. Therefore in using this method, the issues related to the closure of the system is shifted from treatment of the chemical source terms, to modelling unclosed molecular mixing terms [80].

Linear Eddy Model (LEM)

This model was first developed by Kerstein [49, 50] for non-reactive flows but extended to reactive scalars in 1992 [51, 52]. Linear eddy modelling is a method of simulating molecular mixing on a one-dimensional domain embedded in a turbulent flow. The LEM approach aims to treat two different mechanisms that describe the evolution of a scalar: turbulent stirring (or convection), and the molecular diffusion and chemical processes.

$$\frac{\partial}{\partial t}(\rho Y_i) + F_i = \frac{\partial}{\partial x}\left(\rho D_i \frac{\partial Y_i}{\partial x}\right) + \dot{\omega}_i \tag{2.33}$$

where F is symbolic convection term, Y is a scalar, and x is an arbitrary spatial coordinate. The fist phase involves solving the equation shown above (minus the convection term). Secondly, the convection term is modelled. This process consists of a stochastic sequence of independent *rearrangement* events that happen instantaneously on the linear domain at intervals dependant on the flow. Both of these processes take place at the sub-grid scale, and therefore this method tends to be fairly computationally expensive.

The rearrangement events are supposed to represent the effect that a single eddy would have on the scalar profile. The size of the rearrangement domain is chosen based on the eddy size distribution within the flow, and lies between the Kolmogorov scale, and the filter size. This mimicking of the effects of eddies is known as the “triplet map” [50]. The triplet map models the distortion placed on a scalar field segment of a predetermined size by an eddy of similar size. The map maintains continuity and causes a spatial redistribution of the scalar field. It also causes an increase in scalar gradients and a compression as shown in Fig. 2.14.

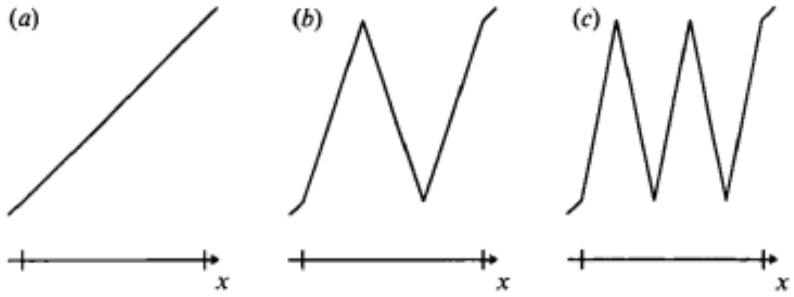

Figure 2.14: Triplet map [50].

Laminar Flamelet

Peters [70, 71] was the first to introduce the idea of the flamelet. One of the most popular models, the underlying assumption of the flamelet model is that the chemical time scales are short compared to the turbulent time scales (high Damköhler number) and that reactions occur in a thin wrinkled layer (known as flamelets). The reactions take place around the stoichiometric mixture iso-line on a scale smaller than the small scales of the turbulence. This assumption has two consequences: firstly, the structure of the reaction zone is assumed to remain laminar, and secondly, the diffusive transport occurs roughly in the direction normal to the surface of the stoichiometric mixture iso-line. The steady flamelet model is often used in LES because of its simplicity but loses accuracy when slow chemical or physical processes have to be considered.

There are two variations for the flamelet model, both that solve for the unsteady flamelets: The lagrangian flamelet model (LFM) [73] and the Eularian flamelet model [72]. Below, the equation for the Lagrangian form is shown

$$\rho\frac{\partial Y_i}{\partial \tau} - \rho\frac{\chi}{2}\frac{\partial^2 Y_i}{\partial Z^2} - \dot{m}_i = 0 \tag{2.34}$$

where ρ is the density, Z is the mixture fraction, Y_i denotes the mass fraction of the chemical species, and τ is time. It should be noted that time in this case is the time defined in a coordinate system attached to the stoichiometric surface (Lagrangian).

The main disadvantage of the LFM is that only a conditionally averaged scalar dissipation rate is used. However, it is known that the scalar dissipation is a highly fluctuating quantity as shown in Fig. 2.15. In this cross-section shown, it can be seen that there is an uneven distribution of scalar dissipation across the stoichiometric iso-line. Local fluctuations can have a strong influence on the flame, and can lead to local extinction or ignition [74]. Thus, by taking its conditional average value, localized characteristics are ignored.

In order to capture the local fluctuations, the Lagrangian model was reconstructed into the Eularian flamelet model [72] shown below. The Eularian flamelet equations shown here is very similar to the first-order CMC model.

$$\rho\frac{\partial Y_i}{\partial t} + \rho\mathbf{v}\cdot\nabla Y_i - \rho\frac{\chi}{2}\frac{\partial^2 Y_i}{\partial Z^2} - \dot{m}_i = 0 \tag{2.35}$$

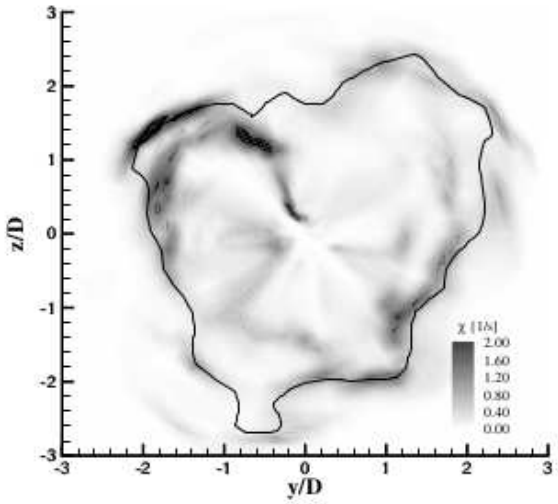

Figure 2.15: Scalar dissipation rate distribution in a cross section of the Sandia D Flame. The stoichiometric mixture fraction iso-contour is indicated by the solid black line [72].

2.2.3 CMC

The CMC model for non-premixed combustion is considered to be one of the more advanced models for turbulent combustion, and was developed separately by Klimenko [57] and Bilger [11] for RANS using two different approaches; Bilger used the decomposition method, while Klimenko used the joint-PDF method. Both approaches yielded the same results which gives credibility to the models formulation. Bilger observed that most of the fluctuations of the reactive scalars are associated with fluctuations of the mixture fraction. Klimenko's outlook on the other hand, was that turbulent diffusion in mixture fraction space can be modelled better than in physical space.

The premise of CMC is to take advantage of the strong correlations between the mixture fraction and reactive scalars (chemical species, temperature, etc), and rather than considering the conventional approach to modelling by averaging, such as the Lagrangian Flamelet model, the CMC approach conditions the reactive scalars on the mixture fraction (or progress variable if considering premixed combustion).

If the fluctuations of the conditional mean of reactive scalars at a given mixture fraction value are small enough, they can be neglected, resulting in first order closure for the chemical source term. The first order CMC equation shares similarities with the Lagrangian flamelet equation except for the addition of spatial diffusion and convection terms which constitute the main modelling difference. The presence of these terms suggests that the physical processes present at the smaller scales of combustion are captured and accounted for within the CMC framework.

Over the past few years countless studies have been conducted within the RANS framework, on simple geometries using CMC for non-premixed combustion, such as of lifted jets [22, 53],

bluff body burners [55, 56], and attached jets [28, 79]. The difference between the simulated results and the experimental results were concluded to be due to the chemical scheme used (normally simple chemical scheme with few species). It was deduced that the chemical schemes were not detailed enough to accurately model the combustion process, and errors occurred due to the underlying assumption of the first order CMC; it neglects the fluctuations of the reactive scalars.

As long as the fluctuations of the scalar around its conditional mean remain small, the model remains fairly accurate, but as the fluctuations increase they can no longer be neglected. The model will still hold, but suffers greatly in terms of accuracy. Areas that tend to have variable magnitude fluctuations in reactive scalars are those of near extinction and ignition. Once the fluctuations of the conditional mean become large, the first order CMC is no longer applicable, and higher order representations must be made

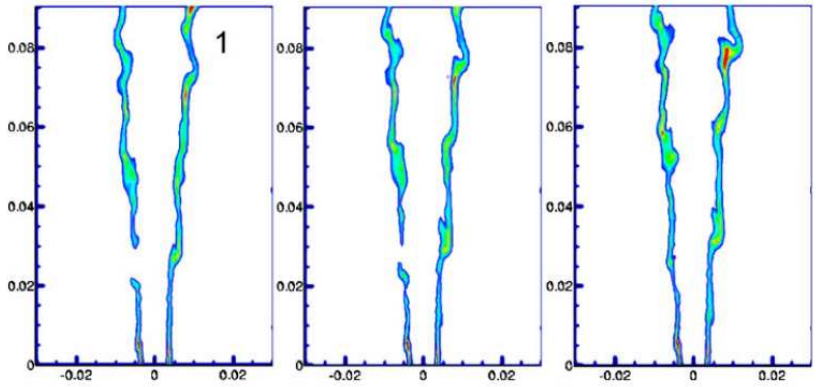

Figure 2.16: Reignition sequence of the flame front depicted by OH mass fraction [8].

There are two possibilities to extend the first order CMC model as outlined by Kronenburg [60]. Firstly, is to consider the second moment closure. It is developed by expanding the chemical source term via Taylor expansion which inherently accounts for the fluctuations in reactive scalars. The other approach suggested by Bilger [10] was to introduce an additional conditioning scalar (double conditioning). However, double conditioning has its own challenges.

- The choice of second conditioning variable is difficult but suggestions include, sensible enthalpy, scalar dissipation, temperature and progress variable.
- The unclosed terms (scalar dissipation, cross correlations between scalar gradients etc) are difficult to model and also cannot be measured via experimentation and thus cannot be validated experimentally.

The effect of doubly conditioned CMC can be seen in Figure Fig. 2.17 where Kronenburg [60] used this model to predict combustion for a simplified 2 step hydrocarbon flame with unity Lewis number. The aim of his study was to determine the accurate closure of the conditional

source term while using DNS data to close the other unclosed terms. He was able to successfully predict species mass fractions at different times, and capture local extinction and the onset of reignition. His results shows the potential of the doubly conditioned CMC, but due to fact that the unclosed terms still cannot be modelled accurately, the practicality of this methods is outweighed by its complexity and uncertainty. The extension to 3D and more detailed chemical schemes still presents a challenge.

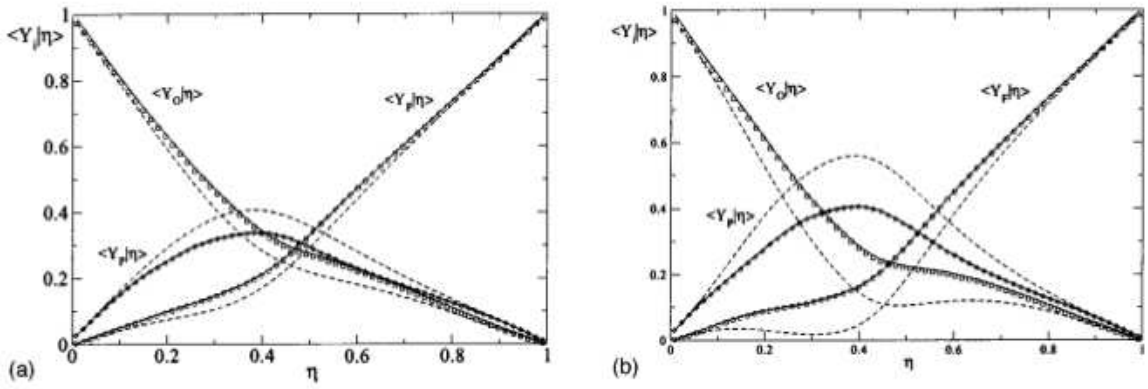

Figure 2.17: Conditionally averaged mass fractions at (a) t= 1.44 and (b)= 1.8. DNS data against doubly conditioned CMC (solid line) and singly conditioned CMC(dashed line) [60].

In 2005, the CMC equations were extended to LES by Martinez [66] with the result that the form of the equations in the LES framework, was similar to that of the CMC in the RANS framework. Since then, simulations of LES-CMC have been preformed on common flames that have previously been performed with RANS-CMC, such as bluff-body [64] and lifted jet [65] as examples. In 2012, Ayache and Mastorakos [8] performed a study on the Delft-III non-premixed flame where they utilised first order 3D LES-CMC with a detailed chemical mechanism. They were able to successfully reproduce the experimental data along with capturing local extinctions along the flame front.

Until recently, CMC has only been used to model combustion for moderately low Reynolds numbers with simple geometries, consequently limiting its applications to only simple cases. What has never been verified to the knowledge of the author, was the ability of CMC to successfully model supersonic compressible flow, and forms the basis for the current study.

as the gradients are smoother in CMC cspace, it can be solved on a coarser grid.

CHAPTER 3

Governing Equations and Numerical Methods

3.1 Governing Equations

Combustion codes that utilize a purely incompressible formulation eg. [63], in their basic formulation, are limited in their ability to resolve certain flow characteristics due to the inherent assumptions of incompressibility or constant density. When applied to combustion modelling, they may still provide relevant information on the general flow phenomena created by the influence of combustion.

Low-Mach formulations eg. [12,21] provide an increased modelling potential to incompressible solvers. In these formulations, density may be allowed to vary but remains independent of pressure, and any compressible features such as shocks, are not resolved. As the name suggests, these formulations are limited to subsonic applications. When interactions between acoustics and combustion need to be analysed, or applications of higher speed regimes want to be modelled, this formulation falls short of its fully compressible counterpart, and the compressible Navier-Stokes equations must be solved.

Compressible formulations eg. [63] represent the most comprehensive formulations. They allow for almost all flow features to be fully resolved. In this family of methods, density is a function of both temperature and pressure. Some of the of the main advantages of compressible methods is the ability to model supersonic combustion, detonation waves, combustion noise, and most importantly, study combustion instabilities. Secondly, a compressible method will employ an explicit time discritisation (mainly Runge-Kutta), and can avoid costly implicit iterative loops that would be needed for incompressible flow. The principle disadvantage with compressible codes is, the acoustic CFL is drastically smaller than for incompressible codes. This means that for a similar flow scenario, using a compressible solver to model a subsonic/incompressible flow would be extremely inefficient. In combustion modelling, one of the criteria for the stable limiting time-step is the chemistry. Depending on the chemistry being modelled, in some cases these two criteria can be comparable. Normally, chemistry is the limiting factor, and therefore the inclusion of compressibility effects does not theoretically increase the computation cost dramatically.

Although there exist a handful of fully compressible methods able to model complex chem-

istry [9, 17, 23, 42, 62], only those proposed by Berglund et al. [9] and Molkov et al. [62] are capable of capturing shocks. The Compressible High Order Combustion (CHOC), is a single block, Cartesian grid code, and was designed in repose to the need for a high order compressible shock capturing method, coupled with robust combustion modelling.

3.1.1 Governing Equations

The proceeding section presents the governing equations used for modelling compressible reacting LES as presented by Poinsot and Veynante [75] and Verman et al. [93]. In the following presentation, $\tilde{(.)}$ represents Favre filtered quantities, and $\overline{(.)}$ represents spatially filtered values. These set of equations consist of the continuity equation,

$$\frac{\partial \overline{\rho}}{\partial t} + \frac{\partial \overline{\rho}\tilde{u}_i}{\partial x_i} = 0 \tag{3.1}$$

and the filtered momentum equation,

$$\frac{\partial \overline{\rho}\tilde{u}_i}{\partial t} + \frac{\partial \overline{\rho}\tilde{u}_i\tilde{u}_j}{\partial x_j} + \frac{\partial \overline{p}}{\partial x_i} - \frac{\partial \hat{\sigma}_{ij}}{\partial x_j} = \underbrace{-\frac{\partial \tau_{ji}}{\partial x_j}}_{A_1} + \underbrace{\frac{\partial}{\partial x_j}\left(\overline{\sigma}_{ij} - \hat{\sigma}_{ij}\right)}_{A_2} \tag{3.2}$$

Where p is the pressure, ρ is the density, u_i are the velocity components, $\tau_{ij} = \overline{\rho}\left(\widetilde{u_i u_j} - \tilde{u}_i\tilde{u}_j\right)$ is the Reynolds stress tensor, and σ_{ij} is the viscous stress tensor, with $\hat{\sigma}_{ij} = \sigma_{ij}\left(\partial\tilde{u}_i/\partial x_j, \tilde{T}\right)$.

As the combustion model utilised in this formulation is of the conserved scalar method family, only one conserved scalar is utilised to represent the fluid mixture. Its conservation equation is represented by,

$$\frac{\partial \overline{\rho}\tilde{\zeta}}{\partial t} + \frac{\partial \overline{\rho}\tilde{u}_i\tilde{\zeta}}{\partial x_i} - \frac{\partial}{\partial x_i}\left(\overline{\rho D_\zeta}\frac{\partial \tilde{\zeta}}{\partial x_i}\right) = \underbrace{-\frac{\partial}{\partial x_i}\overline{\rho}\left(\widetilde{u_i\zeta} - \tilde{u}_i\tilde{\zeta}\right)}_{S_1} \tag{3.3}$$

where ζ denotes the mixture fraction, and D_ζ represents it molecular diffusivity. The mixture fraction ζ, is represented by the scaled O_2 mass fraction given by,

$$\zeta = \frac{Y^o_{O_2} - Y_{O_2}(\mathbf{x}, t)}{Y^o_{O_2} - Y^f_{O_2}} \tag{3.4}$$

where superscript o and f denote the mass fraction of oxygen in the oxidizer and fuel stream respectively. Similar to the explanation in §. 2.2.1, in the oxidizer stream the mixture fraction takes on a value of 0, and in the fuel stream a value of 1.

The formation of the energy equation follows the evolution of sensible energy and kinetic energy. This is also known as "total non-chemical energy" as defined by Poinsot and Veynante [75]. The resulting equations is,

$$\frac{\partial \widehat{\rho E}}{\partial t} + \frac{\partial \tilde{u}_i \left(\widehat{\rho E} + \overline{p}\right)}{\partial x_i} + \frac{\partial \hat{q}_j}{\partial x_j} - \frac{\partial}{\partial x_j}\left(\hat{\sigma}_{ij}\tilde{u}_i\right) = \underbrace{\frac{\partial}{\partial x_i}\overline{\left(\rho \sum_{k=1}^{N} h_{s,k} Y_k J_k\right)}}_{R_1} + \underbrace{\overline{\dot{w}_T}}_{R_2} - B_1 - B_2 - B_3 + B_4 + B_5 + B_6 - B_7 \quad (3.5)$$

where $\widehat{\rho E} = \overline{\rho}\tilde{e_s} + 1/2\overline{\rho}\tilde{u}_i\tilde{u}_i$ ($\tilde{e_s}$ represents the sensible energy, $\tilde{e}_s = \sum_{k=1}^{N}\tilde{e}_{s,k} = \int_{T_o}^{T} C_{v,k}dT - R_u T_o/W_k$, R_u is the perfect gas constant, W_k is the species molecular weight, and $C_{v,k}$ is the species heat capacity at constant volume), $\overline{\dot{w}_T} = \overline{-\sum_{k=1}^{N}\Delta h^o_{f,k}\rho\dot{w}_k}$ is the heat release due to chemical reaction ($\Delta h^o_{f,k}$ is the enthalpy of formation of species k at 298K), and finally, $q_i = -\lambda\left(\partial T/\partial x_i\right)$ (λ is the thermal conductivity) with $\hat{q}_i = q_i\left(\partial T/\partial x_i\right)$. However in this study, a modified formulation of energy was used, namely "the total chemical energy" and the new energy equation is

$$\frac{\partial \widehat{\rho E}}{\partial t} + \frac{\partial \tilde{u}_i \left(\widehat{\rho E} + \overline{p}\right)}{\partial x_i} + \frac{\partial \hat{q}_j}{\partial x_j} - \frac{\partial}{\partial x_j}\left(\hat{\sigma}_{ij}\tilde{u}_i\right) = \underbrace{\frac{\partial}{\partial x_i}\overline{\left(\rho \sum_{k=1}^{N} h_{s,k} Y_k J_k\right)}}_{R_1} - B_1 - B_2 - B_3 + B_4 + B_5 + B_6 - B_7 \quad (3.6)$$

where in this case $\widehat{\rho E} = \overline{\rho}\tilde{e_s} + 1/2\overline{\rho}\tilde{u}_i\tilde{u}_i + \sum_{k=1}^{N}\Delta h^o_{f,k}Y_k$. The primary difference with these two formulations is the absence of the explicit source term R_2. In the latter formulation, the chemistry is used to calculate the mass fractions and then used to update energy. In both formulations however, all the terms on the left hand side are computable using the LES flow field, while those on the right-hand side need to be modelled. These are defined as:

$$B_1 = \frac{\partial}{\partial x_i}\left(\overline{\rho}\widetilde{e_s u_i} - \overline{\rho e_s}\tilde{u}_i\right) \quad (3.7)$$

$$B_2 = \overline{p\frac{\partial u_i}{\partial x_i}} - \overline{p}\frac{\partial \tilde{u}_i}{\partial x_i} \quad (3.8)$$

$$B_3 = \frac{\partial}{\partial x_i}\left(\tau_{ij}\tilde{u}_{ij}\right) \quad (3.9)$$

$$B_4 = \tau_{ij}\frac{\partial \tilde{u}_i}{\partial x_i} \quad (3.10)$$

$$B_5 + B_6 = \frac{\partial}{\partial x_j}\left(\overline{\sigma_{ij}u_i} - \hat{\sigma}_{ij}\tilde{u}_i\right) \quad (3.11)$$

$$B_7 = \frac{\partial}{\partial x_i}\left(\overline{q}_i - \hat{q}_i\right) \quad (3.12)$$

Equation of State

In order to close the above system of equations, an additional relationship must be provided. Commonly this relationship employs a dependence of primitive thermodynamic variables to calculate another. In this study, the gases are assumed to be thermally perfect, meaning the heat capacities are dependant only on temperature. As such, the thermodynamic data (specifically the heat capacity at constant pressure), is extrapolated through JANAF polynomials. However, it should be noted that under this assumption the ideal gas law is still a valid assumption, and is in fact, utilised in the present work in the following form.

$$p(\rho, T) = \rho RT \tag{3.13}$$

Based on the assumption of thermally perfect gas, the relationship between the species heat capacity at constant volume, and species heat capacity at constant pressure, is that of a perfect gas. In this study, variable ratio of heat capacities is used taking the form,

$$C_{v,k} = C_{p,k} - R_k \tag{3.14}$$

$$\gamma_k = \frac{C_{p,k}}{C_{v,k}} \tag{3.15}$$

Modelling Assumptions in CHOC

Following Verman et al. [93] it is common to neglect terms A_2, B_5, B_6, and B_7. The numerical methods implemented in this code [88, 89] are used to model terms A_1, B_3 and B_4. This numerical method is not kinetic energy conserving, but is designed to give leading order dissipation of the kinetic energy proportional to the velocity increment at the cell interface cubed $\left(\Delta u^3\right)$ as expected from Kolmogorov's analysis. The improved interpolation approach helps overcome the typical poor behaviour of the compressible Godunov-type methods at high wave numbers [31, 85]. It acts as an implicit sub-grid model while naturally stabilising the numerical solution and retaining monotonicity. Making the assumption that the implicit dissipation of the numerical methods is sufficient to model the dissipation of turbulent kinetic energy, the terms referring to the Reynolds stresses are also neglected (A_1, B_3 and B_4). This leaves the terms associated with species turbulent diffusion, reaction rates, and turbulent pressure/internal energy fluxes to model (S_1, R_1, R_2, B_1, and B_2).

Smooke and Giovangigli [84] demonstrated that the terms including enthalpy diffusion could be neglected by comparison to the other terms in the energy equation. Based on this, term R_1 is neglected here. The term S_1 is modelled using a gradient model in combination with the turbulent Schmidt number and represents species turbulent transport.

$$S_1 = \frac{\partial}{\partial x_i}\left(\overline{\rho}\overline{D}_t \frac{\partial \tilde{\zeta}}{\partial x_i}\right) \tag{3.16}$$

Terms $B_1 + B_2$ can be represented together by thermal diffusion via the Prandtl analogy.

$$B_1 + B_2 = -\frac{\partial}{\partial x_i}\frac{\overline{\rho}\,\overline{\nu_t}C_p}{Pr_{sgs}}\frac{\partial \tilde{T}}{\partial x_i} \tag{3.17}$$

where the eddy viscosity (ν_t) is estimated using the Smagorinsky model [83].

$$\overline{\nu_t} = (C_s\Delta)^2\left(2\overline{S}_{ij}\,\overline{S}_{ij}\right)^{1/2} \tag{3.18}$$

and,

$$\overline{S}_{ij} = \frac{1}{2}\left(\frac{\partial \tilde{u}_i}{\partial x_j} + \frac{\partial \tilde{u}_j}{\partial x_i}\right) \tag{3.19}$$

3.1.2 Combustion Modelling

The source term R_2 is determined by $\overline{\dot{w}_T} = \overline{-\sum_{k=1}^{N}\Delta h^o_{f,k}\rho\dot{w}_k}$. Closure for this term is typically achieved by a combustion model, which in the case of this study, is the Conditional Moment Closure model. In this model, an equation is solved for the transport of the conditional mean mass fractions of every species taken into consideration.

$$\frac{\partial Q}{\partial t} + \underbrace{\widetilde{u_i^*|\zeta}}_{C_1}\frac{\partial Q}{\partial x_i} = \underbrace{\widetilde{N^*|\zeta}}_{C_2}\frac{\partial^2 Q}{\partial \zeta^2} + \underbrace{\widetilde{\dot{\omega}_k^*|\zeta}}_{C_3} + \underbrace{e_Q}_{C_4} \tag{3.20}$$

where $Q = \widetilde{Y_k^*|\zeta}$ represents the mass fractions conditioned on the mass fraction, and the starred (*) quantities denote parameters on the CMC grid. The equation above contains unclosed terms that require modelling, specifically the conditional velocity term (C_1), the correlation of the conditional fluctuation of $u_i^*|\zeta$ and $Y_k^*|\zeta$ term (C_4), the conditional scalar dissipation (C_2), and the species conditional production/consumption source term (C_3).The term C_4 is given by

$$e_Q = \frac{1}{\overline{\rho^*|\zeta}\widetilde{P}^*(\zeta)}\nabla\cdot\left[\overline{\rho|\zeta}\widetilde{P}^*(\zeta)\left(\widetilde{(u_i Y_k)|\zeta} - \widetilde{u_i|\zeta}\,Q\right)\right] \tag{3.21}$$

where, by applying a gradient model, C_4 becomes,

$$e_Q = \frac{1}{\overline{\rho^*|\zeta}\widetilde{P^*}(\zeta)}\frac{\partial}{\partial x_i}\left[\overline{\rho^*|\zeta}\widetilde{P^*}(\zeta)\overline{D_t}\frac{\partial Q}{\partial x_i}\right] \tag{3.22}$$

where $\widetilde{P}^*(\zeta)$ is the FDF on the CMC grid, and $\overline{D_t}$ is a turbulent diffusivity.

The gradients in conditional space have been shown to be smoother than the gradients in the spatial domain, and thus, CMC is typically solved on a grid coarser than the spatial CFD grid. In CHOC there is an algebraic relationship between the number of CFD cells and CMC cells, and is prescribed *a priori*. An example of the grid relationship can be seen in Fig. 3.1 where the CMC grid (coloured cells) is seen to be comprised of a certain number of CFD cells (black

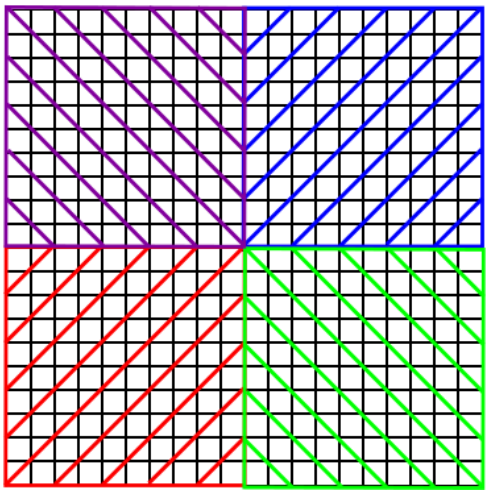

Figure 3.1: Example of CMC vs CFD grid: colours-CMC cells; black grid-CFD cells

cells). Within each CMC cell (similar to the mechanism of solving the Naiver-Stokes equations) the CMC equations are solved for every species under investigation.

Every CMC and CFD cell is extended by an additional dimension known as conditional space, and the "cells" within this 1D domain are known as "bins". On the CFD grid, within every cell, conditional space is required in order to model sub-grid mixing behaviour and to gather unconditional reactive scalar distributions. The conditional information within the CFD cells is required by the conditional space in each CMC cell, in order to evolve the CMC equations. The information is passed between the grids by averaging the information from all the CFD cells contained within the CMC cell; the CMC cell essentially determines the conditional averaging domain. This procedure involves averaging conditional quantities bin by bin, and passing the averaged bin values, to the corresponding bin in the CMC conditional space. The primary parameter that affects the communication and distribution between the CMC and CFD grids is the Filtered Density Function (FDF).

Filtered Density Function

As mentioned in §. 2.2.2, the Beta-PDF is a common distribution used in combustion modelling. However, this code employs the Top-hat distribution because it was shown by Floyd *et al.* [29] that it was better for the use in time dependant turbulent flows. In order to construct the FDF, the scalar variance needs to be modelled. In this case it is estimated using a gradient model [13] instead of the typical transport equation.

$$\tilde{c''^2} = \frac{C_{c'}}{4}\left[(\tilde{c}_n - \tilde{c}_s)^2 + (\tilde{c}_e - \tilde{c}_w)^2 + (\tilde{c}_u - \tilde{c}_d)^2\right] \tag{3.23}$$

$C_{c'}$ is 1/12 and the subscripts n, s, e, w, u, and d, refer to the neighbouring cell locations 'North', 'South' 'East', 'West', 'Up', and 'Down'. More details can be found in [29].

To obtain the FDF on the CMC grid as is needed by term C_4, a density weighted average is taken of all the FDF's in the CFD cells within a respective CMC cell,

$$\widetilde{P}^*(\zeta) = \frac{\int_{Vcmc} \overline{\rho}\, \widetilde{P}(\zeta)\, dV'}{\int_{Vcmc} \overline{\rho}\, dV'} \tag{3.24}$$

where $\widetilde{P}(\zeta)$ is the FDF in each CFD cell.

As detailed previously, solving the flow-field variables requires passing information from the CFD grid to the CMC grid, and conversely back to the CFD grid. When a specific quantity is needed on the CMC grid, a density weighted average of all CFD cells within the CMC cell is taken. This takes the form

$$\widetilde{g^*|\zeta} = \frac{\int_{Vcmc} \overline{\rho}\, g|\zeta\, \widetilde{P}(\zeta) dV'}{\int_{Vcmc} \overline{\rho}\, \widetilde{P}(\zeta) dV'} \tag{3.25}$$

where $\widetilde{g^*|\zeta}$ is then a conditionally averaged quantity g on the CMC grid.

Scalar Dissipation

For the conditional scalar dissipation (C_2), there are two popular models that can be used to represent the scalar dissipation in non-premixed combustion: the Amplitude Mapping Closure(AMC) [67], and the Girimaji model [36]. In these models, the unconditional scalar dissipation is explicitly conditioned through some function $G(\eta)$. The conditioning takes the form.

$$N|\zeta = N\, G(\eta) \tag{3.26}$$

However in CHOC, a different modelling technique is utilised. In this formulation, no explicit condition of the scalar dissipation used, and the conditional scalar dissipation is assumed to be equal to its unconditional counterpart.

$$N|\zeta = N \tag{3.27}$$

The scalar dissipation in every CFD cell is calculated using equation Eq. 3.28 and volume averaged to the CMC grid through means explained in the preceding paragraph (Eq. 3.25). Since the turbulent diffusivity ($\overline{D_t}$) has to be modelled to close dissipation terms in on the CFD grid, it is also used to compute the scalar dissipation in the CFD cells. Thus the model for scalar dissipation becomes,

$$\widetilde{N} = \overline{D_t} \frac{\tilde{\zeta}''^2}{C_{c'} \Delta^2} \tag{3.28}$$

where $\tilde{\zeta}''^2$ is the mixture fraction variance, Δ is the filter width calculated by $\sqrt[3]{\Delta x \Delta y \Delta z}$, and $C_{c'}$ is a constant chosen to be $1/12$. The turbulent diffusivity is modelled by,

$$\overline{D_t} = \frac{\overline{\nu_t}}{Sc_t} = \frac{(C_s \Delta)^2}{Sc_t} \sqrt{2 S_{ij} S_{ij}} \tag{3.29}$$

where the eddy viscosity $\overline{\nu_t}$, is determined through the Smagorinsky model, C_s is the Smagorinsky constant chosen to be 0.1, Sc_t is the turbulent Schmidt number, and S_{ij} is the rate of strain. Finally, the conditionally averaged scalar dissipation on the CMC grid is obtained through Eq. 3.25 yielding Eq. 3.30.

$$\widetilde{N^*|\zeta} = \frac{\int_{Vcmc} \overline{\rho}\, N|\zeta\, \widetilde{P}(\zeta) dV'}{\int_{Vcmc} \overline{\rho}\, \widetilde{P}(\zeta) dV'} \tag{3.30}$$

Conditional Velocity

The conditional velocity (C_1),is fairly straightforward in its assumption and modelling. Following the work of [66], it is assumed to be independent of the conditional variable. Therefore at each CFD cell interface, it is assumed that $\widetilde{u_i|\zeta} = \widetilde{u_i}$. This assumption has not been explicitly validated, but has shown to be a good assumption as it has been used in may of the LES studies previously mentioned, which themselves, show very good results. The conditional velocities are required at the CMC cell interfaces, and are computed based on the solution of the local Riemann problem at each CMC cell interface. Thus, $\widetilde{u_i|\zeta} = \widetilde{u_i^{RS}}$ where superscript RS, indicates the solution to the Riemann problem. The conditional velocities are obtained to the CMC boundaries by integrating using equation Eq. 3.25.

CMC Source Term and Conditional Thermodynamics Quantities

Finally the source term (C_3), is closed using the first order CMC assumption,

$$\overline{\dot{\omega}^*|\zeta} = \frac{\overline{\dot{W}\left(\widetilde{Q}^*|\zeta, \widetilde{T}^*|\zeta, \overline{p}^*|\zeta\right)}}{\overline{\rho|\zeta}} \tag{3.31}$$

where $\overline{\dot{W}}$ is the conditionally filtered chemical mass production rate simply determined by solving the chemical mechanism implemented for given conditional pressure, temperature, and species concentration. Pressure equilibrium is assumed within a computational cell, i.e $\overline{p}|\zeta = \overline{p}$, thus, the conditional pressures are calculated as follows,

$$\overline{p^*|\zeta} = \frac{\int_{Vcmc} \overline{p}|\zeta\, \widetilde{P}(\zeta) dV'}{\int_{Vcmc} \widetilde{P}(\zeta) dV'} \tag{3.32}$$

The source term calculation, C_3, is highly dependant on temperature. Typically when utilising CMC as a closure method, there are k+1 equations to solve; k for the number of species present, and one for some form of energy. This temperature evolution is necessary as the conditional temperatures are a necessary parameter to calculate the conditional source term, and evolve the conditional mass fractions.

If considering incompressible flow, the evolution of energy on the CMC grid would be sufficient to describe the flow on the CFD grid due to the lack of sharp gradients and discontinuities.

However, in shock capturing compressible codes, the acoustics are of utmost importance and require adequate resolution. As the CMC equations are typically solved on a coarser grid than that of the CFD, they may lack the adequate resolution to resolve compressible features. Therefore in this work, as temperature is calculated through the energy equation (Eq. 3.6) on the resolved CFD grid, they are used to calculate the standardized enthalpy within each CFD cell. Eq. 3.25 is then used to bring the standardized enthalpy to the CMC grid at every time-step.

$$\widetilde{h^*|\zeta} = \frac{\int_{Vcmc} \overline{\rho}\,\widetilde{h}\,\widetilde{P}(\zeta)dV'}{\int_{Vcmc} \overline{\rho}\,\widetilde{P}(\zeta)dV'} \tag{3.33}$$

This allows the influence of temperature inhomogeneities due to any compressible flow features on the conditional reaction rates. The conditional enthalpy distribution is then converted into conditional temperatures distribution through iterative techniques, using the conditional species mass fractions.

Once the CMC equation has evolved in time, information from the CMC cells are then required once again in the CFD domain. Depending on the definition of energy used, Eq. 3.34 will either bring the conditional mass fractions, or conditional source terms to spatial CFD domain to update to energy equation. This process takes the form,

$$\widetilde{g} = \int_0^1 \widetilde{g^*|\zeta}\,\widetilde{P}(\zeta)\mathrm{d}\zeta \tag{3.34}$$

where $\widetilde{g^*|\zeta}$ represents the conditionally averaged quantity, and $\widetilde{P}(\zeta)$ is the FDF of the CFD cell in question.

Transport Properties

Species viscosity is calculated by using the Sutherland's law,

$$\mu_k = \mu_{k,ref}\left(\frac{T}{T_0}\right)^{3/2}\frac{T_0+S}{T+S} \tag{3.35}$$

where T_0 is the reference temperature, $\mu_{k,ref}$ is the reference viscosity at T_0, and S is the Sutherland's constant for the species considered. From there, the thermal conductivity can be estimated by using the kinetic theory,

$$\lambda_k = \frac{15}{4}\frac{R_u}{W_k}\mu_k\left(\frac{4}{15}\frac{C_{p,k}W_k}{R_u}+\frac{1}{3}\right) \tag{3.36}$$

The mixture properties are computed using the Wilke's law which is valid for both the viscosity and the thermal conductivity.

$$\Lambda_{mix} = \sum_{k=1}^{n}\left(\frac{X_k\Lambda_k}{\sum_{j=1}^{3}X_j\phi_{kj}}\right) \tag{3.37}$$

where Λ stands for either the viscosity or the thermal conductivity, and ϕ_{kj} is the weighting matrix defined as,

$$\phi_{kj} = \frac{1}{\sqrt{8}} \frac{1}{\sqrt{1 + \frac{W_k}{W_j}}} \left(1 + \sqrt{\frac{\Lambda_i}{\Lambda_j}} \left(\frac{W_j}{W_k} \right)^{1/4} \right)^2 \tag{3.38}$$

In the current formulation, the ratio between momentum and molecular diffusion are assumed to be constant. This ratio is known as the Schmidt number, and by presuming it for a given species, the species diffusivity can be obtained.

$$D_k = \frac{\nu}{Sc_k} \tag{3.39}$$

where ν is the kinematic viscosity. A different assumption that can be made, is on the Lewis number, or the ratio between species and thermal diffusion. Species Lewis numbers are commonly assumed to be constant, and with a specification of the mixture Prandtl number, the Schmidt number can be obtained and used to calculate the species diffusivity as in Eq. 3.39.

$$Sc_k = \frac{Pr}{Le_k} \tag{3.40}$$

with

$$Pr = \frac{c_p \mu}{\lambda} \tag{3.41}$$

where λ is the mixture thermal conductivity, μ is the dynamic viscosity, and c_p is the mixture specific heat at constant pressure. The formulation of Eq. 3.20 inherently assumes that the species Lewis numbers are constant, and in the case of this study, unity.

$$Le = \frac{Sc}{Pr} = \frac{\alpha}{D} = 1 \tag{3.42}$$

with $Sc = \nu/D$, and $Pr = \nu/\alpha$. Making this assumption or presuming these values is often done for simplicity, but carries additional assumption on species thermodynamic behaviour. By presuming them, thermodynamic behaviour is assumed to act in a certain way under all conditions, which is known to not be true; misrepresenting the value of any of these quantities can lead to erroneous results.

3.2 Numerical Methods

3.2.1 Godunov's Method

When the objective is to generate a shock-capturing method, an attractive approach is to utilise a conservative scheme that is Total Variation Diminishing (TVD) [39]. The reason a TVD

scheme is desired is that it allows sharp gradients to be resolved without the generation of spurious oscillations. In this work, a conservative Finite Volume based TVD discritisation is used with the aid of the Godunov method. The first order classical Godunov method can be written in vector form as follows,

$$\mathbf{U}_i^{n+1} = \mathbf{U}_i^n + \frac{\Delta t}{\Delta x}\left(\mathbf{F}_{i-\frac{1}{2}} - \mathbf{F}_{i+\frac{1}{2}}\right) \tag{3.43}$$

Where **F** are the inter-cell fluxes, and **U** is the vector of conserved variables at time steps n and $n+1$. In its basic form it is first order accurate, but one of the attributes that makes this method attractive, is it ability to be used as a basic algorithm with easy extendibility to higher order methods. The simplified solution process of the Godunov method is as follows:

1. Piece-wise discretisation is applied to the cell using finite volume method that represent volumetric averages.
2. A reconstruction step interpolates the data introducing higher order accuracy, and a non-linear stability criterion is employed to avoid oscillations in the reconstruction step (§. 3.2.1).
3. Values at the left and right cell interface act as left and right discontinuities as modelled in the Riemann problem. Using these values, the Riemann problem can now be solved with an appropriate solver (§. 3.2.1).

Within the framework of CHOC, the methods of lines is used which allows for separate temporal and spatial discritisation. In CHOC, a spatial accuracy of order 5 is used along with a temporal accuracy of order 2. The hyperbolic part of the governing equations are calculated using the above Godunov method, while the viscous terms are calculated based on second order central differencing, and Runge-Kutta methods are used for the explicit time integration.

Reconstruction

The spatial accuracy of a scheme is essentially determined by the order of stencil or reconstruction order. With increasing spatial accuracy, comes a reduction in numerical dissipation and in the presence of shocks or sharp gradients, the decreased numerical dissipation can cause high resolution schemes to generate spurious oscillations. Methods have been proposed to overcome these oscillations [90], but the most common method is by the use of slope limiters. High resolution schemes together with slope limiters render a scheme TVD. TVD schemes are inherently monotonically preserving [39] meaning their very nature and formulations inhibit generation of oscillation (local extrema).

High resolutions schemes are attractive for compressible codes because they allow sharper resolution of shocks on a coarser grid, and they require fewer cell within the discontinuity to achieve proper resolution. Within CHOC there are three limiters implemented namely the Van Leer and Minmod limiters, both of which are second order accurate, and the *MUSCL* 5^{th} of Kim

and Kim [54]. The latter has been used in all the computations in this study and therefore will be presented.

$$\mathbf{U}^{L}_{i+1/2} = \mathbf{U}_i + \frac{1}{2}\phi\left(r_L\right)\left(\mathbf{U}_i - \mathbf{U}_{i-1}\right) \tag{3.44}$$

$$\mathbf{U}^{R}_{i+1/2} = \mathbf{U}_{i+1} - \frac{1}{2}\phi\left(r_R\right)\left(\mathbf{U}_{i+2} - \mathbf{U}_{i+1}\right) \tag{3.45}$$

$$\tag{3.46}$$

the ratio of subsequent gradients is given by

$$r^{L}_{i} = \frac{\mathbf{U}_{i+1} - \mathbf{U}_i}{\mathbf{U}_i - \mathbf{U}_{i-1}} \tag{3.47}$$

$$r^{R}_{i} = \frac{\mathbf{U}_i - \mathbf{U}_{i-1}}{\mathbf{U}_{i+1} - \mathbf{U}_i} \tag{3.48}$$

where the limiters $\phi\left(r\right)$ are determined by,

$$\phi_L = \frac{-2/r^{L}_{i-1} + 11 + 24r^{L}_{i} - 3r^{L}_{i}r^{L}_{i+1}}{30} \tag{3.49}$$

$$\phi_R = \frac{-2/r^{R}_{i+2} + 11 + 24r^{R}_{i+1} - 3r^{R}_{i+1}r^{R}_{i}}{30} \tag{3.50}$$

monotonicity of the solution is preserved by using the relationships below to limit the limiters.

$$\phi_L = max\left(0, min, \left(2, 2r^{L}_{i}, \phi_L\right)\right) \tag{3.51}$$

$$\phi_R = max\left(0, min, \left(2, 2r^{R}_{i}, \phi_R\right)\right) \tag{3.52}$$

Riemann Solver

In the present study the Harten-Lax-van Leer-Contact (HLLC) Riemann solver is utilised [90]. This solver assumes a three wave structure to the Riemann problem which allows for two intermediate states to be enclosed by the two characteristic waves. It accounts for rarefaction waves, shockwaves and also a contact surface which is crucial in multi-component modelling.

Low Mach Number Correction

In Godunov type methods, there is a certain level of artificial dissipation associated with its implementation and usage. Thornber *et al.* [89] presented an analysis that the incorrect pressure scaling at low Mach numbers in Godunov type methods is caused by the large velocity jumps at the cell interfaces. A low Mach treatment was developed to treat this excess numerical dissipation by a function *z*, which gives reconstructed velocities.

$$\mathbf{u}_L^c = \frac{\mathbf{u}_L + \mathbf{u}_R}{2} + z\frac{\mathbf{u}_L - \mathbf{u}_R}{2} \tag{3.53}$$

$$\mathbf{u}_R^c = \frac{\mathbf{u}_L + \mathbf{u}_R}{2} + z\frac{\mathbf{u}_R - \mathbf{u}_L}{2} \tag{3.54}$$

where z is defined by the local Mach number by,

$$z = min(M_{Local}, 1) \tag{3.55}$$

where M_{local} is given by,

$$M_{local} = max(M_L, M_R) \tag{3.56}$$

It was also shown that based on this reconstruction function, the kinetic energy dissipation was proportional to $u^3/\Delta x$ which is similar to that proposed by Kolmogorov for the decaying turbulence. As indicated previously, this allows an implicit modelling of therms A_1, B_3 and B_4 in Eqs. 3.2, 3.5 and 3.6, leads to the conclusion that this code belongs to the class of Implicit Large Eddy simulation.

Time integration

As the time step is very small compared to that of incompressible solvers, it is not necessary to implement very high order time integration. With fifth order reconstruction there is very little difference in solution between second and higher order time integration, and as a consequence, an explicit time integration in CHOC is achieved using a two stage second order TVD Runge-Kutta method [82].

$$\mathbf{U}^{(1)} = \mathbf{U}^n + \frac{\Delta t}{\Delta x}\mathbf{F}\left(\mathbf{U}^n\right) \tag{3.57}$$

$$\mathbf{U}^{n+1} = \frac{1}{2}\left[\mathbf{U}^n + \mathbf{U}^{(1)} + \frac{\Delta t}{\Delta x}\mathbf{F}\left(\mathbf{U}^{(1)}\right)\right] \tag{3.58}$$

where the limiting time step size is determined from the following

1. Acoustic CFL condition - $CFL = \left(\Delta t\left(|\tilde{u}| + a\right)\right)/\Delta < 1$
2. Conditional Velocity - $\Delta t\left(\widetilde{u_i^*|\zeta}\right)/\Delta < 1$
3. Péclet number due to the conditional scalar dissipation - $2\Delta t\widetilde{N^*|\eta}/\Delta\zeta^2$
4. Chemistry - to avoid excess consumption of species ($Y_k > 0$)

where Δ is the minimum cell spacing, and $\Delta\zeta$ is the minimum spacing in conditional space. In this work, an additional time integration scheme has been implemented. A second order four

step Runge-Kutta was also implemented into the code. This allowed the maximum CFL to have a value of 3.

$$\mathbf{U}^{(1)} = \mathbf{U}^{n} + \frac{1}{3}\frac{\Delta t}{\Delta x}\mathbf{F}\left(\mathbf{U}^{n}\right) \tag{3.59}$$

$$\mathbf{U}^{(2)} = \mathbf{U}^{(1)} + \frac{1}{3}\frac{\Delta t}{\Delta x}\mathbf{F}\left(\mathbf{U}^{(1)}\right) \tag{3.60}$$

$$\mathbf{U}^{(3)} = \mathbf{U}^{(2)} + \frac{1}{3}\frac{\Delta t}{\Delta x}\mathbf{F}\left(\mathbf{U}^{(2)}\right) \tag{3.61}$$

$$\mathbf{U}^{n+1} = \frac{1}{4}\mathbf{U}^{n} + \frac{3}{4}\mathbf{U}^{(3)} + \frac{1}{4}\frac{\Delta t}{\Delta x}\mathbf{F}\left(\mathbf{U}^{(3)}\right) \tag{3.62}$$

CHAPTER 4

CMC for Supersonic Combustion

The objective of this work was to use demonstrate a first approach in utilising the CMC to model supersonic combustion. The availability of supersonic combustion experimental data is very limited, and therefore the choice of test cases are not vast. Along with the lack of available data, the test case must also be chosen based on the current limitations of CHOC (1 block/Cartesian).

Typically, supersonic combustion validation cases lack quantitative information of chemical species, and are limited to wall pressure distributions. This form of validation is difficult as the simulation then becomes an acoustic simulation requiring a substantially resolved grid with higher order time integration. Wall-bound flows also require adequate mesh refinement near the walls in order to capture the boundary layer and correct heat flux, and thus pressure. For high Reynolds flows, the boundary layer becomes smaller and smaller, requiring more and more refinement near the wall if no wall functions are present within a code. Therefore, cases where pressure distributions are the form of validation for combustion processes, are generally more computationally demanding and complex.

Reactive supersonic shear layer studies on the other hand, although more scarce and complex experimentally, provide a relatively better indication of a combustion models ability to capture transient phenomena and combustion physics. As there are usually no walls, the only experimental measurements are the averaged quantitative reactive scalar data, which are normally given at different locations in the flow. This allows a spatial evaluation of modelling potential and limitations, and removes the uncertainty caused by wall bounded flows and boundary layers.

In order to assess the ability of CMC to capture supersonic combustion, a shear layer study was preferred for the aforementioned reasons, however, the next obstacle was determining a viable validation case within the limitations of CHOC. One of the best reacting supersonic shear layer studies is that by Chen *et al.* [16]. Along with species and temperature information at different locations, this case also provides additional statistical information in the form of RMS values of species concentrations and temperature. However, due to the experimental setup and geometry, the case is too complex geometrically, and requires advanced boundary conditions currently non-existent in CHOC.

–	NX	NY	NZ	Cells Count(10^6)
Coarse	64	64	256	1.048
Medium	100	100	384	3.84
Fine	128	128	512	8.388

Table 4.1: Computational domain used in Eggers Jet Simulations

The test case chosen and to which the present study was mimicked, was the publication by Karaca *et al.* [46]. This study analysed a high-speed reacting and non-reacting hydrogen-air jet using similar order numerics to those implemented in CHOC. Most importantly, the computational domain was well within the capabilities of CHOC. For this, these test cases were deemed suitable. As a consequence of the similarity between the two studies, the computational setup was influenced by those published by Karaca *et al.*.

4.1 Supersonic Mixing - Frozen Chemistry

The first section of the study investigates a frozen chemistry case. The motivation for conducting a frozen chemistry case was to assess the ability for the solver to model the flow correctly and capture adequate mixing i.e. the breakdown length of the potential core, and development of the shear layer. These are important phenomena, and are fundamental characteristics that are crucial to capture correctly in modelling reactive and non-reactive jets. Poor capturing of these phenomena in frozen chemistry, has the implication for potentially poor results within reacting flows. The test case analysed for this flow regime is the experiment by Eggers [26]. This test case involves injection of a circular jet of H_2 into a supersonic co-flow of air in a constant test section, allowing mixing at near atmospheric pressure.

4.1.1 Computational Grids and Domain

CFD Grid

The computational domain for this test case is a $70mm \times 70mm \times 700mm$ domain as shown in Fig. 4.1. Three simulations were conduced on meshes ranging from 1 million (1M) to 8.3M cells. Details of the grid setup are given in Table 4.1. Ideally isotropic grid spacing should be used, especially when using higher order spatial discritization, however, if the grid is sufficiently smooth, clustering can be acceptable. In this case, grid clustering is used, and is achieved in the transverse and cross-stream directions by utilizing a hyperbolic sine relationship given below.

$$x = 0.5\left[\frac{1.0 + \sinh(\delta\,(X - 0.5)}{\sinh\,(\delta)}\right] \tag{4.1}$$

where $X = Y$ and $X \in [0, 1]$. In the axial direction, clustering is achieved utilizing an exponential function,

$$z = \frac{\exp(\beta Z - 1.0)}{\exp(\beta - 1.0)} \tag{4.2}$$

where $Z \in [0, 1]$. The stretch factors δ and β, were chosen to achieve approximately the same ratio between smallest and largest cell size utilized by Karaca *et al.*. In the axial direction this ratio is 6, yielding a value for β of 1.8. In the transverse directions, the ratio used was 5, yielding a stretch factor δ, of 4.5. These constants were used throughout all the simulations. As the constants were determined based on the coarse simulation, the ratios between the largest and smallest cells changed slightly for the medium and fine simulation. The differences were negligible, with the order of magnitude still maintained at 6 and 5 for the axial and transverse directions respectively. It should be emphasised that although the ratio between the smallest and largest cell are similar to those in the literature, the distribution of cells within the computational domain are quite different due to the different functions used to calculate the stretching.

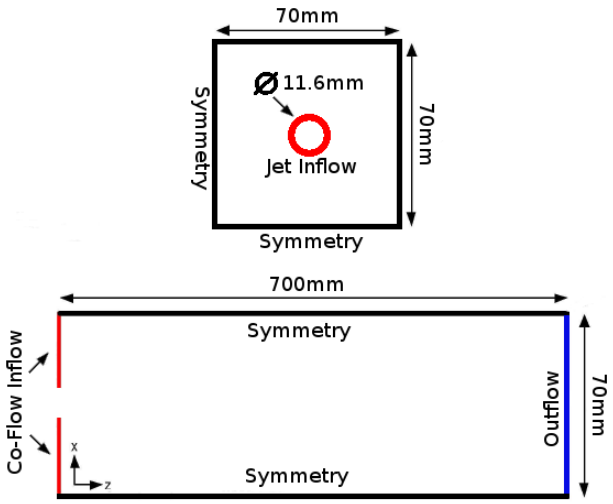

Figure 4.1: Computational Domain for Eggers Jet

CMC Grid and Conditional Space

Traditionally, multi-species mixing is achieved by solving conservation equations on the CFD grid, with the number of conservation equations equal to the number of species under analysis. As this study employs the CMC model for closure of the energy source term, it was decided to utilise the CMC model at its frozen limit. That is, to keep the CMC model active and effectively use it as a sub-grid mixing model. The equations would be solved as in a reacting case with the source term equal to zero. As in the reacting case, the FDF would be responsible for determining the species concentrations in a given cell. This methodology was deemed to be acceptable, and within the capability of the model as outlined in §4.3 of [58].

	NXC	NYC	NZC	CMC Cell Count
Coarse	1	1	32	32
Medium	1	1	48	48
Fine	1	1	64	64

Table 4.2: Eggers jet CMC grid

	Air Co-flow	H_2 Jet
H_2	0.0	1.0
O_2	0.232	0.0
N2	0.768	0.0

Table 4.3: Boundary species mass fractions for Eggers simulations

For the case setup previously described, it was seen that for CMC operating at its frozen limit, having a fine CMC grid versus a coarse CMC grid made no difference term C_2 in Eq. 3.20 was the leading order term both cases. As a consequence of this, the proceeding simulations were run with a coarser CMC grid to slightly reduce the computational cost. In addition to this, as the conditional gradients in the cross-stream direction are very small in comparison to the mean axial conditional gradients, there was no need for a multi-dimensional CMC grid. This yielded a 1 dimensional CMC grid with each CMC cell having the dimensions $NX \times NY \times 8$ CDF/CMC. The total distribution of CMC cells for all the simulations is given in Table 4.2

Much of the analysis of the CMC and conditional space grids was omitted in this section. They are not as influential in the frozen chemistry simulations, as they are in the reacting cases. With the lack of chemistry and consequently sharp gradients, the effects of these two grids is difficult to analyse as no relevant of conditional reactive scalars occurs. A more detailed analysis is presented in the portion of the study concerning reacting flows, more specifically §. 4.2.1

4.1.2 Initial Conditions and Boundary Conditions

The boundary conditions for the Eggers simulations are presented in Tables 4.3 and 4.4. The mass fractions used in this simulation are only that of the major species in air, namely O_2 and N_2. The presence of H_2 in this case does not cause a chemical reaction as the temperatures of the two streams are well below the autoignition temperature of the mixture. Simulations at these low temperatures are beneficial because they allow fuel mixtures to be studied without the influence of combustion, which normally make pure mixing studies of fuels difficult. Additionally the utilisation of a specific fuel as opposed to thermodynamically different inert species (such as N_2 or He), allows more accurate, species specific, mixture phenomena and behaviour, to be observed and studied.

In all of the simulations, Lewis numbers were all kept constant at unity (Le=1), as the current

	Air Co-flow	H_2 Jet
U $[m/s]$	1074	394
T_{stat} $[K]$	260	222
P_{stat} $[kPa]$	100	100
ρ $[kg/m^3]$	1.563	0.093
M	1.32	0.886

Table 4.4: Boundary conditions for Eggers simulations

formulation of CMC is based on unity Lewis assumption. The Prandtl number was assumed constant at 0.709, and the turbulent Schmidt number was unity ($Sc_t = 1.0$).

Boundary Conditions

The boundary conditions utilised in this simulation are shown in Fig. 4.1. In the transverse directions are Euler wall (symmetry), while the outflow is supersonic outflow. The inflow is slightly modified to accommodate velocity profiles and a turbulence generator.

Velocity Profile

Fig. 4.2 shows the inlet velocity profile that was extracted from numerical simulations by Karaca *et al.*. It corresponds to the velocity profile at the fictitious cross-stream plane at H_2 jet exit. It is important to capture the correct velocity profiles and gradients at the interface of the fluids as these quantities are paramount in the development of the shear layer and mixing of the fluids. All the simulations conducted for this test case use this profile as a template, interpolating based on the grid resolution and distribution. Points were clustered in regions of higher gradients to adequately capture the profile features even at low resolutions.

Turbulence Generator

In order to help trigger the transition to turbulence, a simple white noise turbulence generator was implemented at the boundary. It takes the form,

$$u' = (\epsilon w_{Jet} r_1) \tag{4.3}$$

$$v' = (\epsilon w_{Jet} r_2) \tag{4.4}$$

where in this case, fluctuations are only applied in the transverse directions, and are confined only to the jet. The random values r_1, r_2 are recalculated every time-step, and only determine the direction of the fluctuation; they can take on values of -1 or 1. The magnitude of the fluctuation (ϵ) was constant at 1% of the maximum jet velocity, giving a fluctuation of approximately $10.7 m/s$. This method of turbulence has been shown to be a poor representation of turbulence

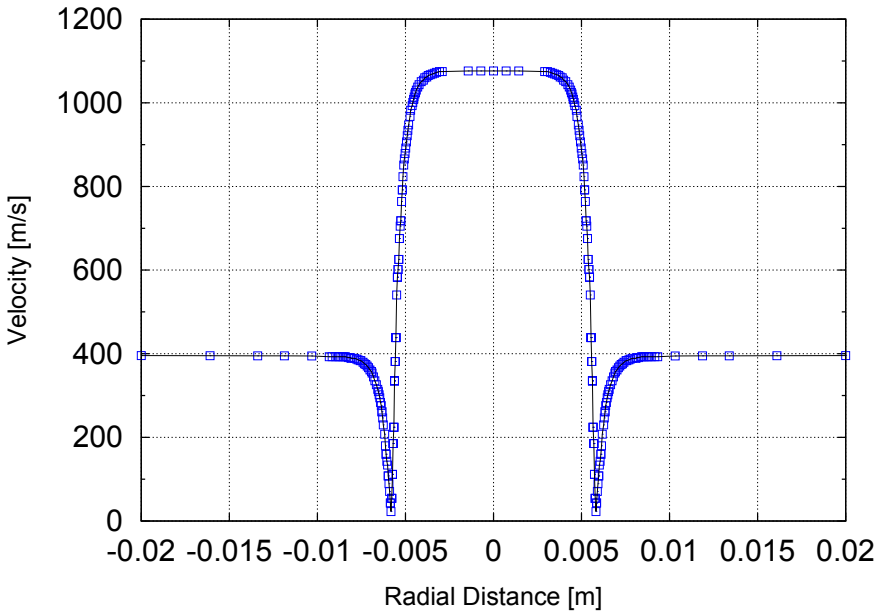

Figure 4.2: Inlet velocity profile used for Eggers jet simulations

[77], however given the time frame and priority of this study, a simple turbulence generator was needed to aid in the transition to turbulence and the white noise generator was deemed feasible.

4.1.3 Averaging of Results

Interactive time averaging began after allowing the flow to stabilise for 3 flow through times. A flow through time was considered the time required for the co-flow to enter and exit the domain which was determined to be approximately 1.6ms. Temporally averaged results were obtained by averaging a total of 480 evenly spaced samples over 3 flow through times (160 samples/flow-through), giving each simulation a total of 6 flow through times. Fig. 4.3 shows the effect of sample rate where different sampling frequencies were taken ranging from 50/flow-through, to 250/flow-through. It was seen that for 160 samples and above, the difference was negligible on the resulting average.

Fig. 4.4 shows a temporal forward-averaged density at 4 different probe locations throughout the domain for the fine simulation. The fine simulation was used in this demonstration because, theoretically, this simulation would exhibit more fluctuations, and thus take longer to converge given a similar sampling frequency. The sampling frequency for all these locations is 160 sample/flow-through as determined above, however, these figures show the effect of initialisation time of the interactive averaging process on the averaged results. The earliest initialisation time is after one flow-through, and the latest is at the 5^{th} flow-through. It can be seen that it takes approximately 2 flow-through times for the averages to stabilise at this sampling

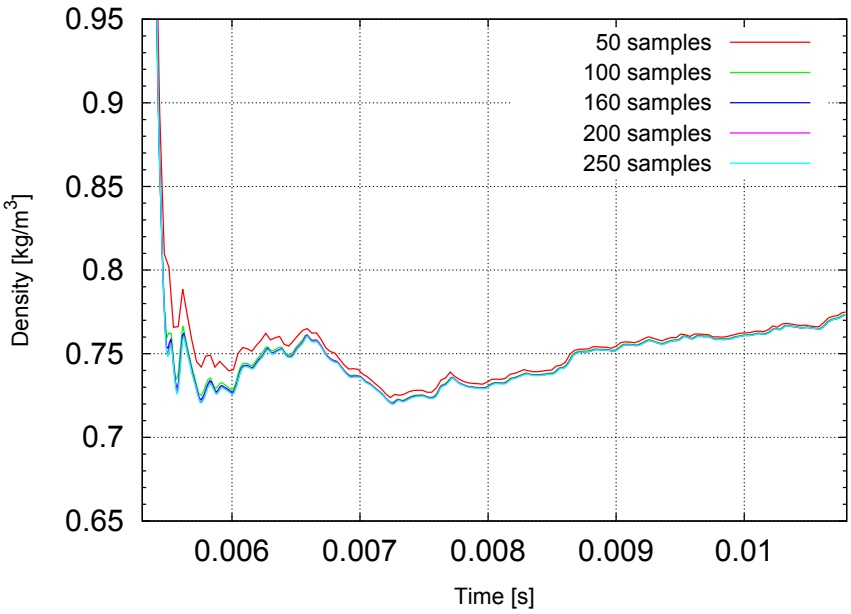

Figure 4.3: Sampling frequency comparison

frequency. As a consequence, beginning the averaging after 4 or 5 flow-though times would result in non-converged results. Elaborating on that point, it can also be said that it is indeed possible to begin the averaging process after 1 flow-through time. This is evident as beginning at 1, 2, or 3 flow-through times all converged to the same values. It can therefore be concluded that, instead of waiting 3 flow-through times to begin averaging for an additional 3 flow-through times, averaging could have commenced earlier reducing the total simulation time.

4.1.4 Simulation Results

Presented in Figs. 4.5 to 4.10, are the major results of the simulations plotted against the experimental results from Eggers [26] and Karaca *et al.* [46]. The locations of the experimental data of centreline profiles shown in Fig. 4.5, correspond to all the locations that have radial distributions as well. In this study only four axial locations are investigated radially: $x/D = 5.51$ (x=63.3mm), $x/D = 9.58$ (x=110.17mm), $x/D = 15.44$ (x=177.56mm), and $x/D = 25.2$ (x=289.9mm). These locations are important because this region exhibits the largest gradients, and they describe the transient processes/phases of the jet before it becomes self-similar.

A preliminary conclusion from the centreline data shows that qualitatively, the simulation seems to fit the experimental data moderately well. However, a difference is visible between the H_2 profiles and the velocity profiles. The H_2 mass fraction profiles fit well up to about an $x/D \approx 25.2$. Thereafter, the H_2 mass fraction level off while the experiment shows continued gradual decay. The velocity appears to begin to decrease roughly at the correct location, but decays more sharply and for a longer distance compared to the experimental results.

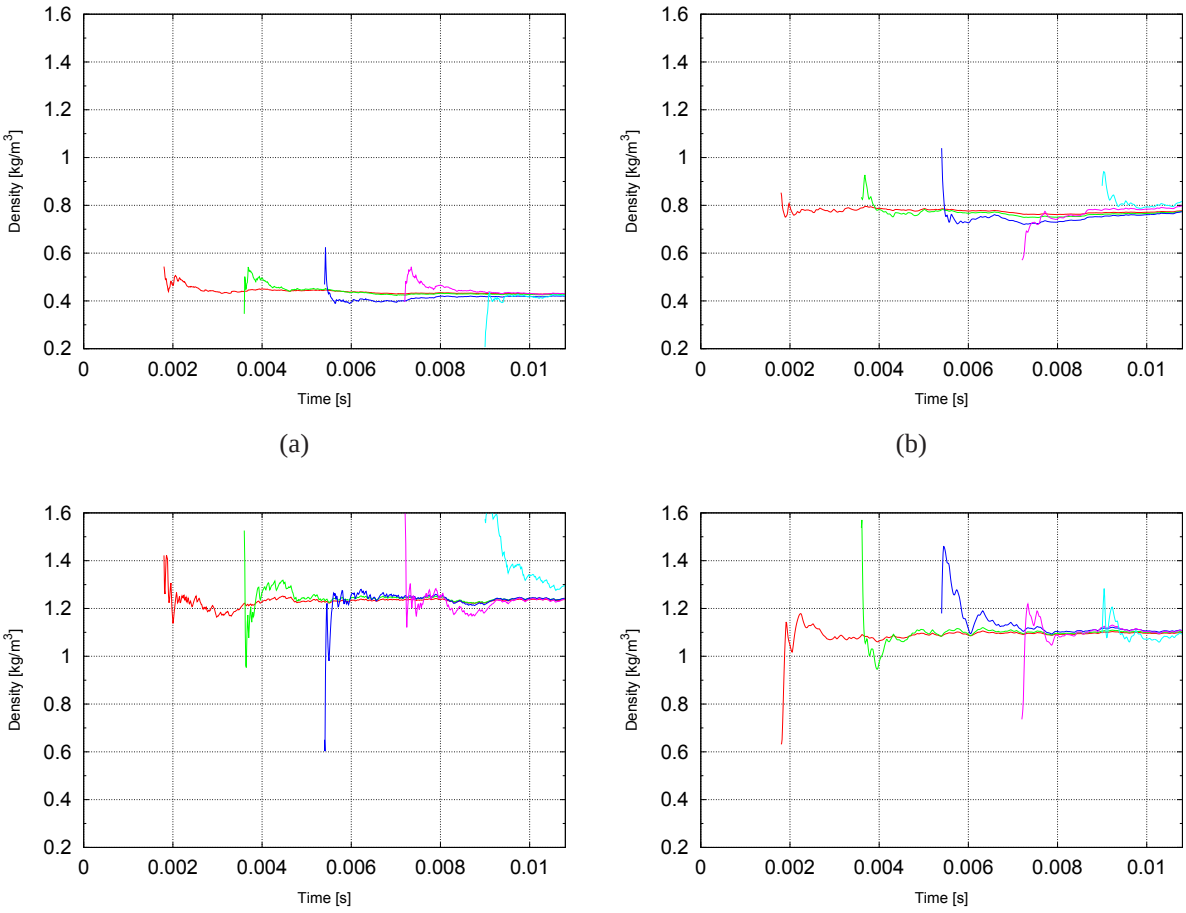

Figure 4.4: Effect of averaging initialisation time on converged density averages for 4 probe locations throughout the domain

H2

The two centreline figures are accompanied by the numerical results of Karaca *et al.*. The rate of mixing of H_2 seems to be similar for both simulations up till about $x/D = 17$, where the present results show a decreased rate. It is not entirely certain what causes this, however one of speculations for this is the assumption of incorrect modelling of species diffusivity.

The assumption of constant Lewis number in mixing simulations is not a bad assumption as the temperatures do not vary significantly as they would for reacting cases. However, when considering species with such a difference in molecular transport such as H_2 and air, accurate thermodynamic transport representation is necessary. Due to the unity Lewis assumption in this work, the Schmidt numbers are also kept constant at 0.709. For O_2 and N_2 this may not be a very inaccurate assumption, but it is well known that assuming unity Lewis and "typical" Schmidt values for H_2 can result in skewed, inaccurate results. According to Giacomazzi [35]

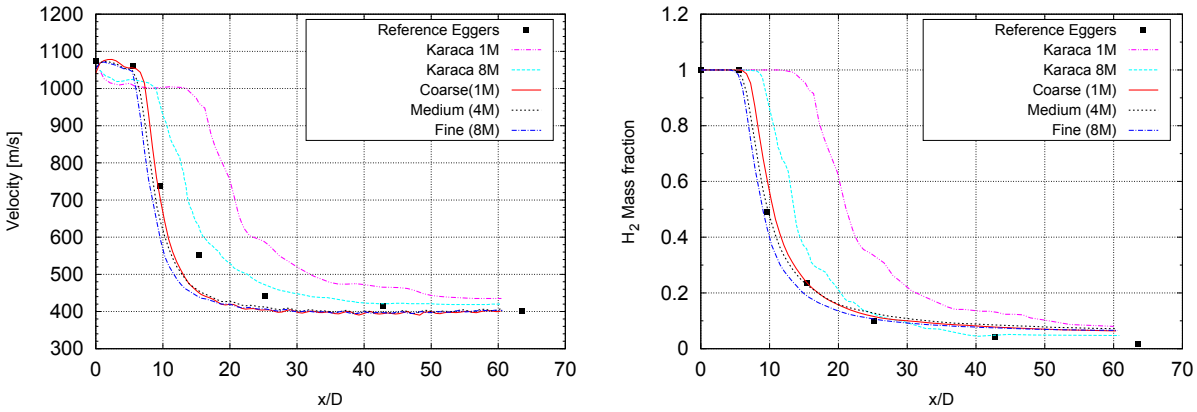

Figure 4.5: Centreline distribution of velocity and H_2 mass fraction

the typical Schmidt numbers for these molecules are about 0.8 for both O_2 and N_2 and about 0.35 for H_2 (Le= 1.26, 1.27 and 0.35 for O_2, N_2, and H_2 respectively).

Karaca *et al.* use variable molecular transport, and in addition to the Navier-Stokes (N-S), perform an additional simulation using a Euler formulation. The immediately obvious results from these simulations, is that the N-S simulation shows a faster breakdown of the concentration potential core, and a slightly steeper decay of the H_2 mass fraction compared to the Euler. The profiles begin to deviate at about $x/D = 15.44$ with the N-S simulation ultimately reaching a slightly lower final mass fraction at the domain exit. This would indicate that although the principle mixing mechanism in these high Reynolds flows is inviscid turbulent mixing, diffusion has a noticeable influence on the overall mixing of the fluids. Whether this noticeable influence is specific to the species in question (H_2), or diffusion in general is unclear, but nevertheless, accurate modelling of diffusion is necessary.

In the case of the present simulation, the downstream region of higher mass fraction of H_2 may be caused for multiple reasons. Firstly is the stretch rate of the grid compared to that of Karaca *et al.*. As mentioned earlier, although the ratio between the smallest and largest cells are similar, due to the stretching functions being different, the inlet section of the domain is more resolved, and the opposite it true for the downstream section. This decreased resolution downstream acts to smear and dissipate much of the turbulent motions that are in fact, the dominant mixing mechanism. The well resolved inlet section could also explain the improved capturing of the potential cores by the presented 1M results to those of the 8M of Karaca *et al.*. Secondly, the assumption of constant Schmidt (Lewis) numbers does not isolate H_2 as a strong diffusive species compared to the others, and does not conform to the established need for accurate molecular transport. The current numerics implemented lack this capability as constant species diffusivities is assumed in the formulations of the CMC equations.

Velocity

Compared to the H_2 profiles, the velocity profiles hint that the simulation may be too dissipative. In conjunction with the experiment, Eggers did a numerical study on various eddy viscosity models. The primary conclusion was that there was a difference in centreline profiles and jet decay rates based on the eddy viscosity model chosen; The larger the eddy viscosity component, the faster the jet decay rate. Additionally, Uzun*et al.* [43]. performed a classical LES study of a Mach 0.9 jet of air-air and studied the effect of the Smagorinsky constant on the simulated jet behaviour. The study involved multiple simulations, where only the Smagorinksy constant was varied. What was seen was that the larger constant resulted in a faster jet decay, and a lower jet momentum spread. A 5.56% difference in the constants led to approximately a 15.20% increase in decay rate and 18.87% reduction in jet spread. The results of studies illustrate the sensitivity of the jet decay rate to viscosity.

This type of study could prove to be difficult for ILES simulations of jets, as the sub-grid dissipation is a function of the numerical scheme and is not quantifiable. It was thought that the excess decay of the jet was perhaps a consequence of the current numerical schemes, and that it was overly dissipative. Based on the results of Uzun*et al.* [43], a variation of sub-grid dissipation does not have to be substantial to have a large influence on jet behaviour. However, the excess dissipation seems to be localised after about x/D=9.58, where the present jet continues to decay, while the experimental data gradually stabilises. Prior to this location, the simulation jet decay rates are comparable to experiment. The initial jet decay rate calculated ($x/D \approx 8$) as indicated in [43], gives the experimental Eggers jet a decay rate of 9.25, and the present simulations a rate of about 9.88. In addition to this, due to the presence of the low Mach number correction, Thornber *et al.* [85] illustrated that the modified MUSCL 5^{th} scheme used in CHOC, was less dissipative than the standard MUSCL 5^{th}, and the WENO 5^{th}. Therefore it can be concluded that the numerical scheme is not overly dissipative and is not the reason for the localised excess decay.

It was therefore thought that the random white noise turbulence inlet was the cause of the excess decay. As a result of this doubt, a simulation for the medium case was run without the aid of the turbulence generator. Fig. 4.6 shows that without turbulence the initial trends of velocity are still captured well although there is a shift in breakdown location. This gives reassurance that the turbulence generator is not the principle reason for the apparent excess decay of the jet.

What must also be mentioned is the effect of laminar viscosity. In the early stages of the jet, as the momentum dissipation is still primarily laminar as the flow has not yet fully developed, the effective viscosity is dominated by the laminar contribution. In the simulations, the Sutherland law is used to calculate the mixture viscosity, however, the coefficients used for all species is that of air. This greatly overestimates the viscosity as at 298K, the viscosity of air is 2.5 times greater than H_2. This overestimated viscosity contribute and provide insight to the excess decay of velocity.

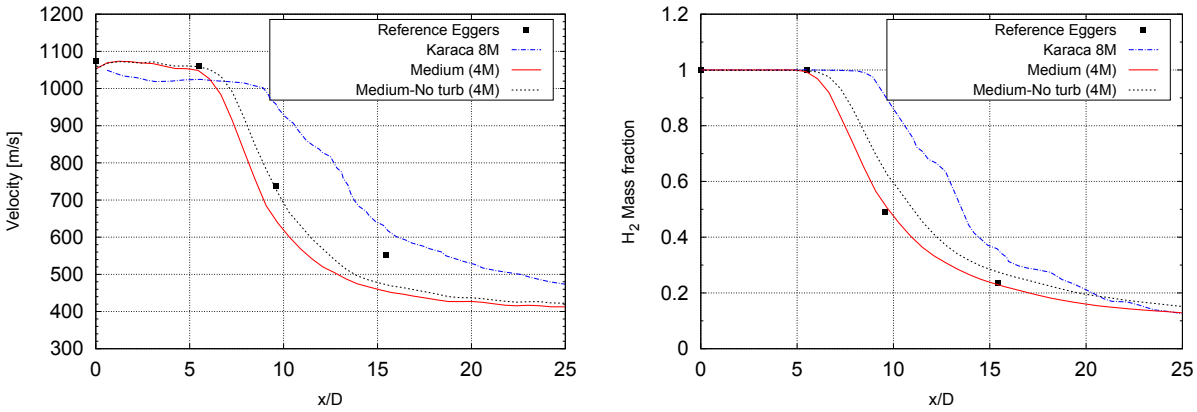

Figure 4.6: Centreline profiles of velocity and H_2 mass fraction with no turbulent inlet

Effect of Grid Distribution

It is true that with the exponential clustering implemented in the axial direction, the inlet section of the present simulation would have an effective resolution much higher than the averaged domain resolution. Exponential clustering (inherent to its name) places and unbalanced number of cells at either extreme of the coordinate direction it alters. In the present case, the upstream portion of the domain may be over-resolved with respect to the downstream portion. Further increasing the resolution while keeping the stretch coefficient constant, may not always be required as further refinement in the upstream portions of the domain may not be necessary to the same extent as the factor of cell increase. In fact, perhaps with increasing grid resolution, the stretch coefficient should be relaxed to give a better overall resolution increase. Nevertheless, this clustering distribution was implemented because it was thought that even at coarse resolution, capturing the initial development of shear layer instabilities was crucial in modelling the jet.

This asymmetric distribution of the grid, could potentially lead to visible asymmetries when approaching very fine simulations. This effect is apparent through the profiles of the current simulation varying much more upstream between the coarse, medium, and fine, as opposed to the downstream sections where only minor differences are seen. This is in contrast to the numerical results of Karaca *et al.* where, because a more relaxed clustering distribution was used, the effect of increasing resolution was more noticeable throughout the entire simulation. Increasing the resolution showed a global convergence towards the experimental values, as opposed to isolated regions of the domain shown in the present simulation.

As a consequence of this, an additional simulation was conducted simulating a half domain with 8M cells (effective 16M) with a stretch factor β of 1.1. The hope was that any under-resolved regions were to blame for the excess decay of the jet. The results showed slightly better agreement downstream with the upstream portions having an almost negligible change. Most importantly, the region of excess decay was not significantly altered giving credence to

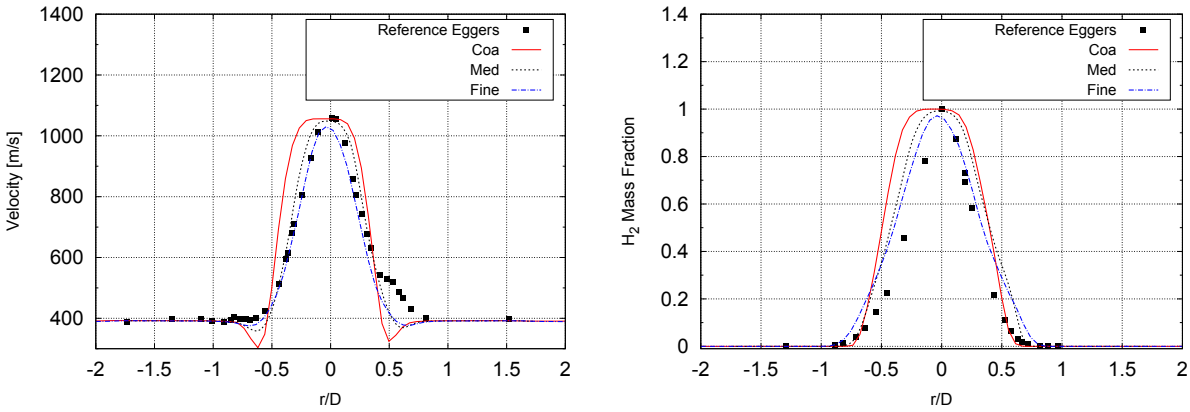

Figure 4.7: Radial distributions at x/D=5.51 of velocity and H_2 mass fraction

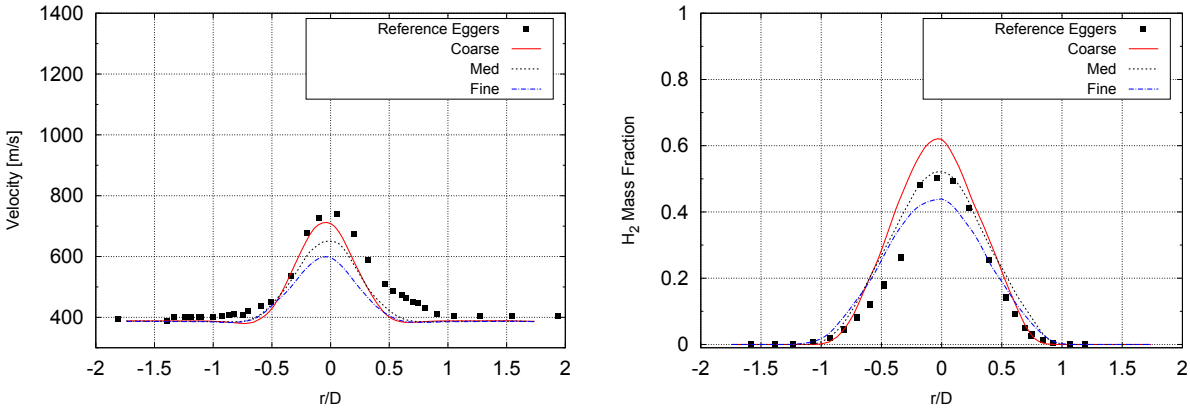

Figure 4.8: Radial distributions at x/D=9.58 of velocity and H_2 mass fraction

the idea that this region is a consequence of a different or underlying more fundamental issue. It also verifies that the grid in it's current form, is satisfactory in capturing the flow features and is adequately converged.

Radial Distributions

Typically for jet simulations, if the centreline data is accurate, radial distributions will not be far off. Nevertheless, it is worth investigating the radial distributions, more specifically the early regions of the jet, e.g. the potential core region. This region is important in jet physics because it dictates the region where the shear layer merges, and where the transition region begins. This transition region location is dictated by the shear layer growth rate, and has a direct effect on the jet spread and the jet decay rates.

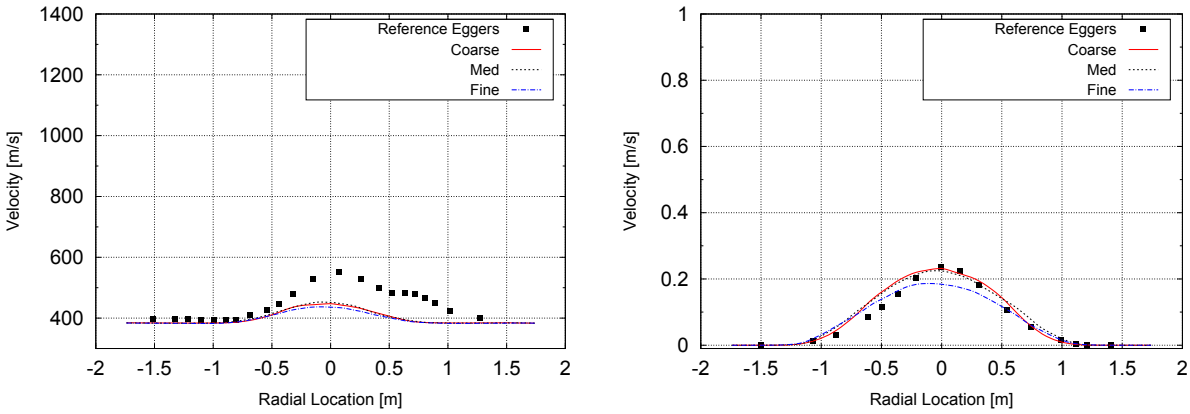

Figure 4.9: Radial distributions at x/D=15.44 of velocity and H_2 mass fraction

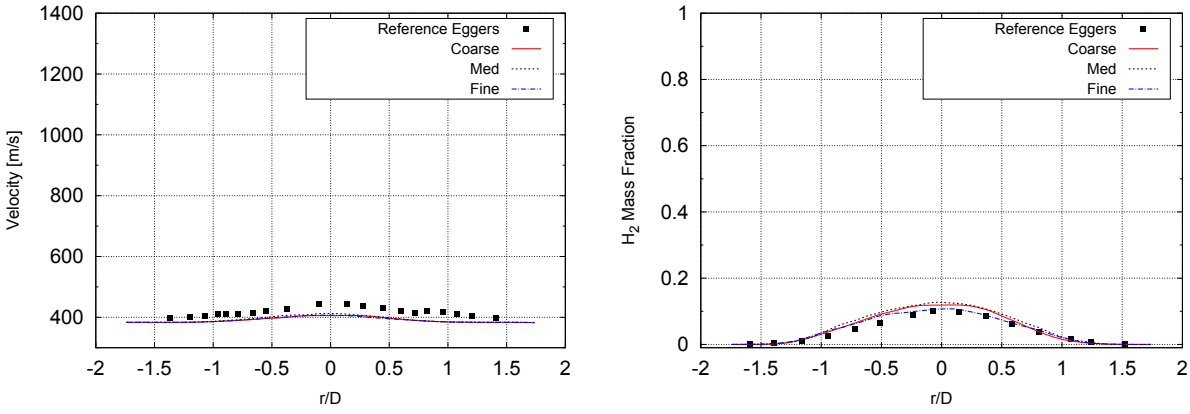

Figure 4.10: Radial distributions at x/D=25.2 of velocity and H_2 mass fraction

Fig. 4.7 shows the results of the simulations for the region at the approximated potential core length, with the difference between the three resolutions immediately visible. With increasing grid resolution, the traces of the initial velocity gradient/discontinuity at the fluid interface disappears. In addition to this, the profile widths indicate that the shear layers at this location are of different sizes. They indicate different capturing of shear layer instabilities upstream of this region. At this location, from experiment, the shear layer non-dimensional thickness based on the mass fraction of H_2, was determined to be 0.706. From the simulations, the shear layer thickness approximations are 0.527, 0.64335, and 0.79623, for the coarse, medium, and fine respectively. As expected the finer simulation tends to grow sooner as at this location the shear layer is the thickest of all three simulations. However, the over estimation of the shear layer thickness for the fine simulation, indicates that perhaps the inadequate turbulence generator added additional non-physical perturbations that caused the instabilities to grow sooner than they should have. This can also be verified with the potential core being shorter than what was observed in experiment (Fig. 4.5).

Figs. 4.8 to 4.10 show the remaining radial profiles at different axial locations downstream of the potential core. As expected the correlation between centreline fit and radial profiles is illustrated. The H_2 profiles seem to correlate fairly well with experiment, but as expected from the accuracy of the centreline profile of velocity, the radial profiles of velocity seem to deviate substantially. Due to the nature of modelling jets and the sharp decay of parameters they experience after the potential core, a small shift in jet breakdown length can have a profound impact on the radial profile distributions. This consequently leads to relative inaccuracies of the simulation. Therefore one of the key characteristics to capture accurately when modelling any jet, is the initial development of the shear-layer, and thus, the potential core length.

4.2 Supersonic Combustion - Reacting Case

The proceeding section aims to demonstrate the first application of the conditional moment closure model to a supersonic reacting H_2-air jet. The test case chosen for this demonstration was the LAERTE jet from ONERA [32, 46]. Similar to the motivation chosen for the frozen chemistry case, this case was deemed acceptable as it was a shear-flow test case that removed the complexities of wall modelling. Additionally, the geometry of the test section was simple enough to be used within the capabilities of CHOC.

A comprehensive grid convergence study for the reacting case would involve a coarse, medium, and fine simulation on the CFD grid, with coarse, medium, and fine, 1D, 2D, and 3D CMC grids. Assuming three resolutions in conditional space, that would be equivalent to a minimum of 81 simulations. This is indeed not practical, however, some assumptions and simplifications can be made to help reduce this number. §. 4.2.1 presents a study that enabled the determination of the conditional space grid *a priori*. Additionally, in a previous paper by Thornber *et al.* [86], it was shown that the difference between 1D CMC, and 2D or 3D was not substantial. Therefore, based on those results, and the notion that the jet is axis-symmetric and the conditional gradients in the cross-stream direction are small compared to the axial direction, only a 1D CMC grid was used in the axial direction. Lastly, presented in §. 4.2.7, is the study that led to the usage of a single CMC resolution, further reducing the number of simulations required in the grid convergence study. Based on these assumptions and studies, the total number of simulations was greatly reduced from 81. The proceeding section presents, a total of 3 simulations utilising an axial, 1D, medium resolution CMC grid, with a fixed, equispaced conditional space distribution.

4.2.1 Computational Grids and Domain

The computational domain for this test case is a $45mm \times 45mm \times 350mm$ that corresponds to the constant cross section portion of the ONERA LAERTE combustion chamber. As with the frozen chemistry case, three simulations were conduced ranging from 1M to 8.3M cells. Details of the grid resolution are given in Table 4.5.

	NX	NY	NZ	Cells Count(10^6)
Coarse	64	64	256	1.048
Medium	100	100	384	3.84
Fine	128	128	512	8.388

Table 4.5: LAERTE Jet computation sizes

Clustering is achieved in the transverse and cross-stream directions by utilising the hyperbolic sine relationship given for the frozen chemistry case in §. 4.1.1. The stretch factors δ and β, were once again chosen to achieve approximately the same ratio between smallest and largest

cell size utilised in the previous section. In the axial direction this ratio is 6 yielding a value for β of 1.8, while in the transverse directions, the ratio used was 5 yielding a value for δ, of 4.5.

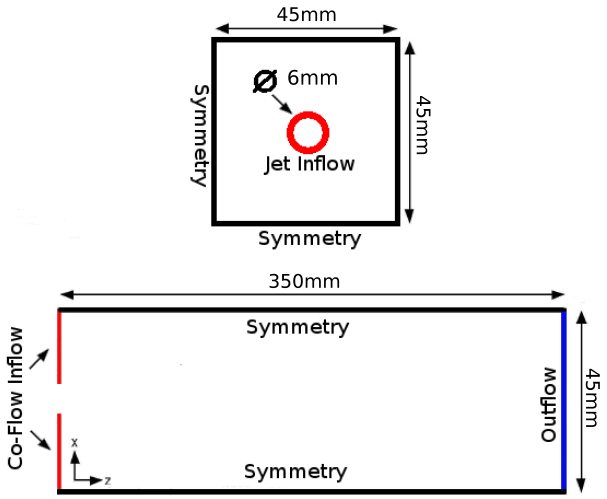

Figure 4.11: Computational Domain for LAERTE Jet

CMC Grid

Unlike the previous test case where CMC was operating at its frozen limit, for the reacting cases, the CMC grid was altered and refined. Having too coarse of a CMC grid for a reacting case can have a profound impact on the simulations as will be demonstrated in section §. 4.2.7. Therefore, the proceeding simulations were conducted with what was deemed, a medium CMC grid. For all the simulations unless otherwise indicated, each CMC cell has the dimensions $NX \times NY \times 4$ CFD/CMC. The total number of CMC cells in the computational domain can be seen in Table 4.6.

	NXC	NYC	NZC	CMC Cell Count
Coarse	1	1	64	64
Medium	1	1	96	96
Fine	1	1	128	128

Table 4.6: CMC Grid size for the CFD grid convergence study for the LAERTE Jet

Conditional Space

A convenient property of conditional space, is that it represents the combustion process given certain external inputs. These inputs come in the form of specific parameters of which the

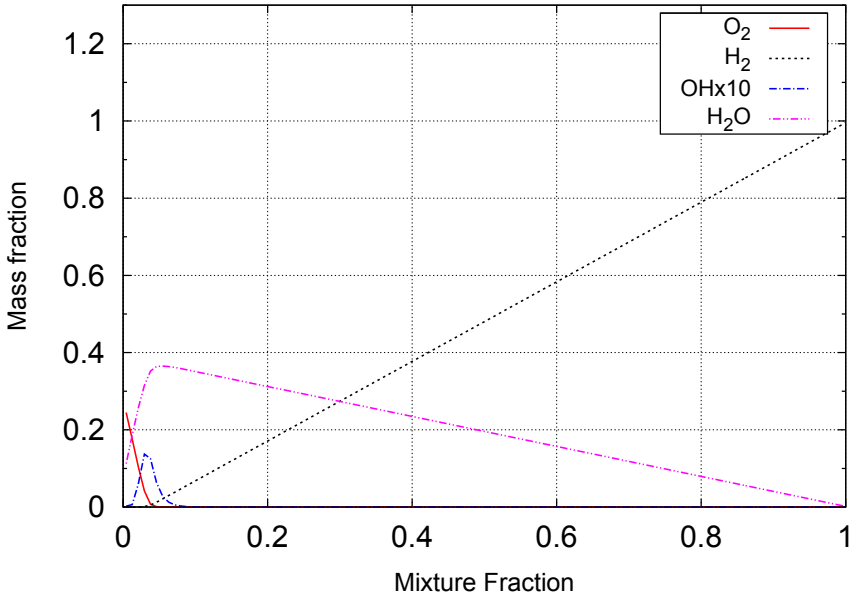

Figure 4.12: Distribution of major species at a Scalar dissipation of 1; boundary conditions are set to those of the LAERTE Jet.

solution in conditional space is explicitly dependant on. What makes this a convenient attribute is that it allows the solution in conditional space to be obtained with only a few inputs. As a result, the effect of grid resolution in conditional space can be analysed independently and *a priori* to the full simulations which allows the simulation convergence study to be reduced by a dimension.

Solving conditional space and obtaining averaged mixture quantities only requires information from the CFD grid; information that for the sake of analyses, can be artificially provided to the CMC equations. The primary parameters required are the scalar dissipation, mixture fraction, and mixture fraction variance. As the scalar dissipation increases, the gradients in conditional space become smoother, the opposite is true for a decreasing scalar dissipation. Therefore, the extreme case (or the case with the sharpest gradients) occurs when the scalar dissipation approaches 0. To analyse the grid sensitivity in conditional space, a solution in conditional space was obtained for a scalar dissipation rate of 1(1/s) using 6 different, equispaced grid resolutions: 50, 100, 120, 180, 200, and 500; 500 being considered as the control. To illustrate the solution-space, Fig. 4.12 shows the steady-state solution of the conditional mass fractions in conditional space using 500 conditional bins. The boundary conditions used to obtain this solution are those listed in Tables 4.7 and 4.8.

Calculating the unconditional mass fractions from this distribution of conditional mass fractions is done using Eq. 3.34. The FDF shapes that are used, corresponded to the shapes generated in the region of mixture fraction space near stoichiometry ($\zeta_{st} \approx 0.0298$), as this region exhibits the sharpest gradient. The FDF can either be an analytical or discrete function (Beta

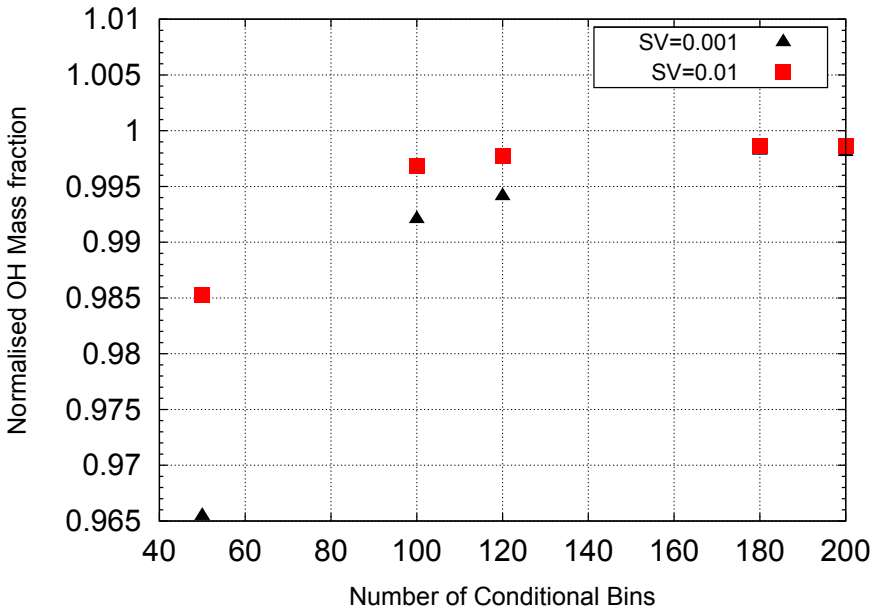

Figure 4.13: Normalised unconditional mass OH fraction

and Top-hat respectively) of the mixture fraction and it's variance. This means for any given number of realisations of these two parameters, similar combinations of the two always produce the same FDF shapes.

As a measure of convergence, the unconditional OH mass fraction was used. Using the previously indicated number of conditional bins, two possible FDF shapes were constructed and integrated yielding an unconditional OH mass fraction. This value was then normalised based on the value obtained from a simulation using the control at 500 bins. The 500 bin limit represents an extreme upper limit for the resolution in mixture fractions space, as the total number of calculations per time-step and memory requirement scale proportionally with it's size.

Fig. 4.13 shows that relative errors of less than 1% begin after about 100-120 bins which leads to the conclusion, that obtaining a relatively high accuracy, does not require an high number of bins. To see the effect of conditional space resolution where the gradients are not as sharp as the region about stoichiometry, a similar study was performed near a mixture fraction of 0.97. In this case, the same variances as in the previous study were used, however, H_2 was used as at this mixture fraction, OH is not present and H_2 experiences the sharpest gradients. This study yielded a maximum unconditional H_2 mass fraction difference between 50 and 500 conditional bins of 0.00297%. This result is not surprising as in this region the conditional mass fractions profiles are quite linear.

The results presented here represent idealised results with "clean" values of mixture fraction and variance. In reality, these two parameters will not take on such ideal values. The mean

mixture fraction given to conditional space determined where the FDF is constructed around, and may not coincide with the distribution of conditional bins. This in turn may introduce small errors in the location of the FDF mean. The variance on the other hand, affects the broadness of the FDF and bounds. The Beta-PDF is less prone to this error, as it's distribution is analytical, and a solution can theoretically be obtained for any distribution of conditional bins. The Top-hat on the other hand, is built from discrete functions, and uses specific locations in conditional space for its bounds. Therefore these locations are also susceptible to their values not coinciding with grid locations on the conditional space grid. Although the implementation of the FDFs aims to conserve the mean, and avoid these very small errors, they are inevitable. However, it should be noted that the errors are not very large and are quantifiable. As an example, for 120 conditional bins, the extreme case of both Top-hat FDF endpoints being located in-between conditional bins locations, leads to a maximum error of about 0.83%.

The aforementioned discussion, plus the obvious differences in gradients at locations near stoichiometry compared to the rest of conditional space, raise an obvious question about grid clustering. Fig. 4.14 shows the grid points for 120 bins for the grid convergence study mentioned above, along with the OH distribution. It can be seen that only about 13 conditional bins fall within the OH distribution. Therefore only about 10% of the points used in conditional space are used to capture OH. Ideally, grid clustering can be implemented in conditional space around the stoichiometric mixture fraction to greatly reduce the number of grid points present, decrease conditional space computation time, and increase the effective resolution. However, decreasing the spacing between conditional bins also increases the influence of the Péclet number criteria for limiting time step. In this criteria, the minimum conditional grid spacing is used. In the case of a multi-step, time-splitting, time integration as implemented in this code, having a smaller Péclet number would increase the overall computation time. A balance between grid clustering and number of conditional bins is required, and whether the increased computational time due to the increased iterations from a smaller time-step, is outweighed by the accuracy and decreased computational time from the clustered conditional space grid, is the subject of another study. From the presented *a priori* study, 120 equispaced bins were chosen to represent mixture fractions space for all the simulations.

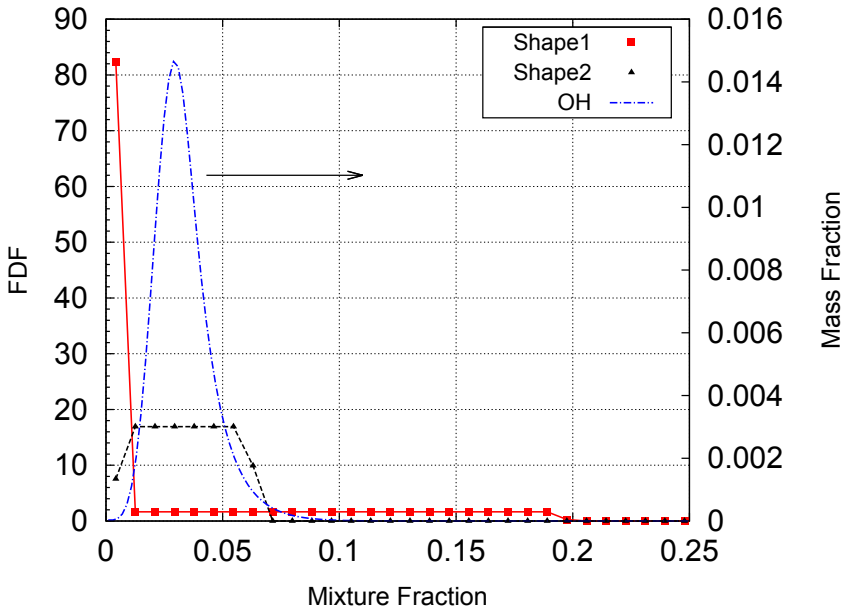

Figure 4.14: Distribution of conditional bins in conditional space

4.2.2 Initial Conditions and Boundary Conditions

Contrary to the frozen chemistry case, the initial/boundary species mass fractions for the air co-flow were not of strictly of the major species in air, and included traces of H_2O and O, H, and OH radicals. Specific quantities can be seen in Table 4.7. Additionally, the temperature of the jet and air co-flow in this case, were much higher. This ensured that the mixed H_2-air streams were well above the autoignition temperature. Specific details of the inlet conditions are shown in Table 4.8 Lewis numbers were kept constant at unity (Le=1) for all species as

	Air Co-flow	H_2 Jet
H_2	0.0	1.0
O_2	0.2447	0.0
H_2O	0.1124	0.0
OH	2.285×10^{-4}	0.0
O	1.8×10^{-5}	0.0
N_2	0.64265	0.0

Table 4.7: Initial and boundary mass fractions for the LAERTE Jet

required by the formulation of CMC utilised in this study. For the proceeding simulations, the Prandtl number was assumed constant and fixed at 0.709. The turbulent Schmidt number was constant at unity ($Sc_t = 1.0$).

	Air Co-flow	H_2 Jet
U[m/s]	1366	1970
$T_{stat}[K]$	1170	160
$P_{stat}[kPa]$	92	84
$\rho[kg/m^3]$	0.259	0.127

Table 4.8: Initial and boundary flow conditions for the LERTE Jet

Velocity Profile

The inlet velocity profile shown in Fig. 4.15 was extracted from numerical simulations by Karaca *et al.*, and represents the velocity profile at the fictitious cross-stream plane at the jet exit. Points on the profile, were clustered around the regions of highest gradients to ensure adequate profile resolution, even at lower grid resolutions.

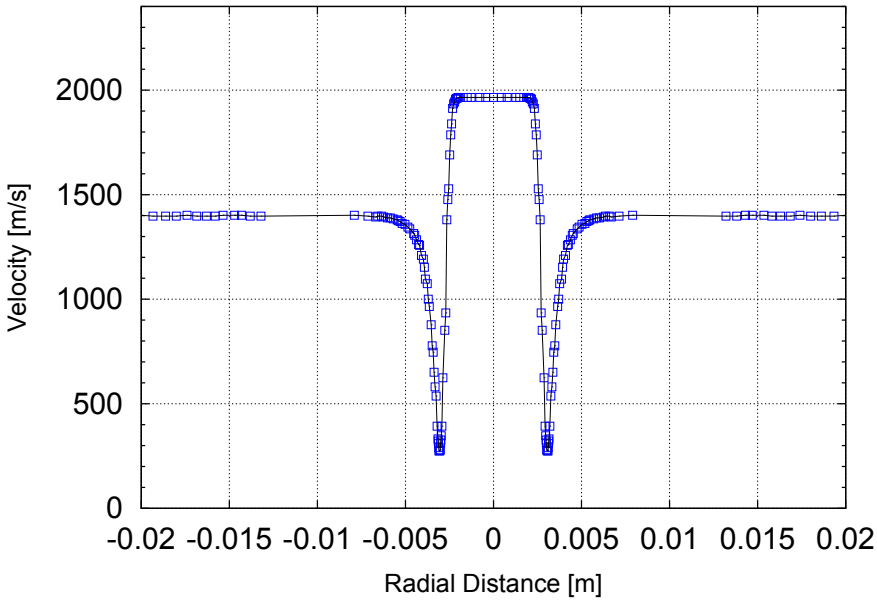

Figure 4.15: Inlet velocity profile used for LAERTE Jet Simulations

Turbulence Generator

In order to help trigger the transition to turbulence a simple white noise turbulence generator was used, taking the form similar to the turbulence generator used in the frozen chemistry simulations. The fluctuations were only applied in the transverse directions and are confined to

the jet. The magnitude of the fluctuation (ϵ) was constant at 1% of the maximum jet velocity, giving transverse fluctuations of approximately $19.7m/s$.

4.2.3 Averaging of Results

Interactive time averaging began after allowing the flow to stabilise for 3 flow through times. Temporally averaged results were obtained by averaging a total of 480 evenly spaced samples over 3 flow through times (160 samples/flow-through) giving each simulation a total of 6 flow through times. A flow through time was considered the time required for the co-flow to enter and exit the domain which was determined to be approximately 0.27ms.

4.2.4 Simulation Results

Centreline distributions of H_2 mass fraction and velocity are shown in Fig. 4.16, showing adequate convergence between the medium and fine simulations. What is almost immediately evident is that the velocity decay is not as sharp as with the frozen chemistry case. Instead, there is a much smoother decay towards the self-similar region. The fine simulations is similar to the medium expect that near the domain outflow, there is a slightly better mixing captured. What is also shown, is that between the medium and fine simulations, the potential core is captured almost identically. This is in comparison to the previous case, where there was a noticeable difference in potential core breakdown location with grid refinement. It appears as if the white noise turbulence no longer has an substantial effect on the simulations, or the effect is the same for both grid resolutions. As the time-step is decreased with increasing grid resolution, the overall frequency (and wavenumber) of the synthetic turbulence is increased. As large wavenumbers are dissipated more quickly than lower wavenumbers, at the given resolutions of both the medium and fine simulations, it is possible that the perturbations by the turbulence generator are immediately dissipated.

In reacting flows, the more important representative quantity in simulations is the temperature. Fig. 4.17 shows radial distributions of temperature at two axial locations, along with experimental data and those obtained by Karaca *et al.*. Unfortunately, the experimental temperature data shown was the only data available for this test case, and it was stated in the paper [46] that the experimental results are very poor — The velocity was underestimated and the mean temperatures were overestimated because of the flapping nature of the jet. No relative errors were published and therefore it is unclear how inaccurate the data truly is.

The experimental data resembles the early stages of the averaging procedure of the simulations, and it is possible (but uncertain) that the high temperature point at 1600K is an outlier. Instantaneous temperature profiles from the simulations experienced similar peak temperatures (sometimes even reaching 2000K), but due to the flapping nature of the jet, the averaged temperature dropped substantially to those shown. However, even if the temperatures are overestimated, the trend of the experimental data is still expected to maintain some accurate qualitative

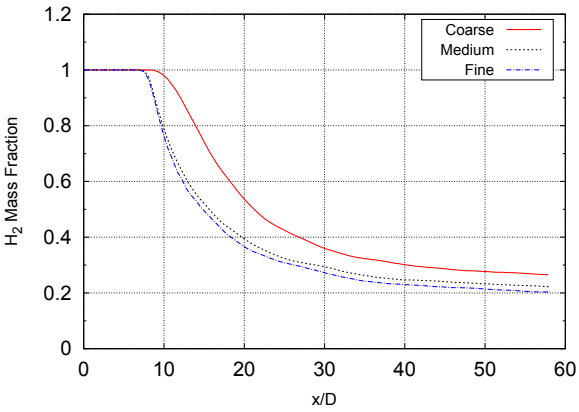

(a) Centreline distribution of H_2

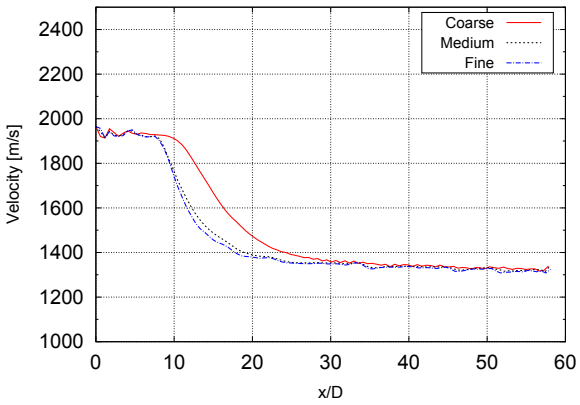

(b) Centreline distribution of velocity

Figure 4.16: Centreline distributions of H_2 mass fraction and velocity

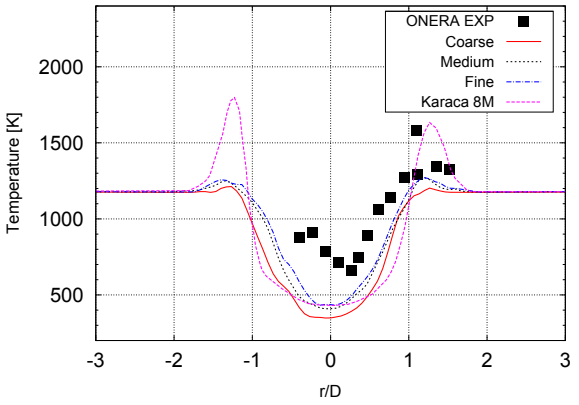

(a) Radial Distribution of temperature at x/D=35

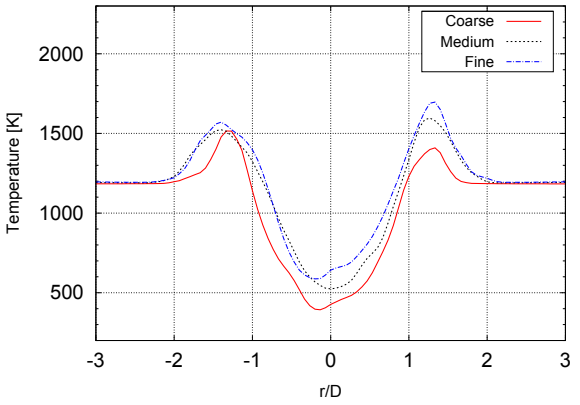

(b) Radial Distribution of temperature at x/D=57.5

Figure 4.17: Radial ditributions of temperature at selected axial locations

description of the structure of the jet. Based on this criteria, the presented simulations follow the trends very well except for a perhaps a slightly lower temperature in the shear-layer at $r/D \approx 1.3$.

A independent analysis of the temperature profiles gives clear indication that combustion is occurring at the exit of the computational domain ($x/D = 57.5$), as there is an approximate increase in temperature of 500K from the air co-flow temperature. Even at $x/D = 35$, the temperatures are lower than the exit plane, but still higher than the mixture temperatures, indicating the presence of chemical reactions. If indeed the experimental temperatures are over estimated, then it is safe to conclude that the results of the present study match well to the experiment. The lower temperatures experienced at $x/D = 35$ also indicate that the combustion process has only just begun in this region.

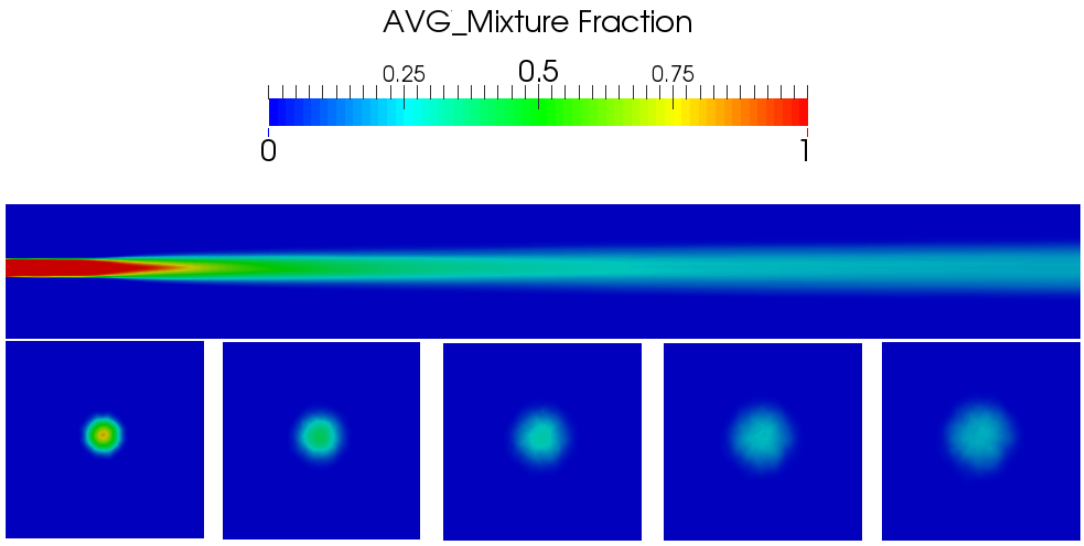

Figure 4.18: Time averaged mid-plane contour of mixture fraction along with selected cross stream contours

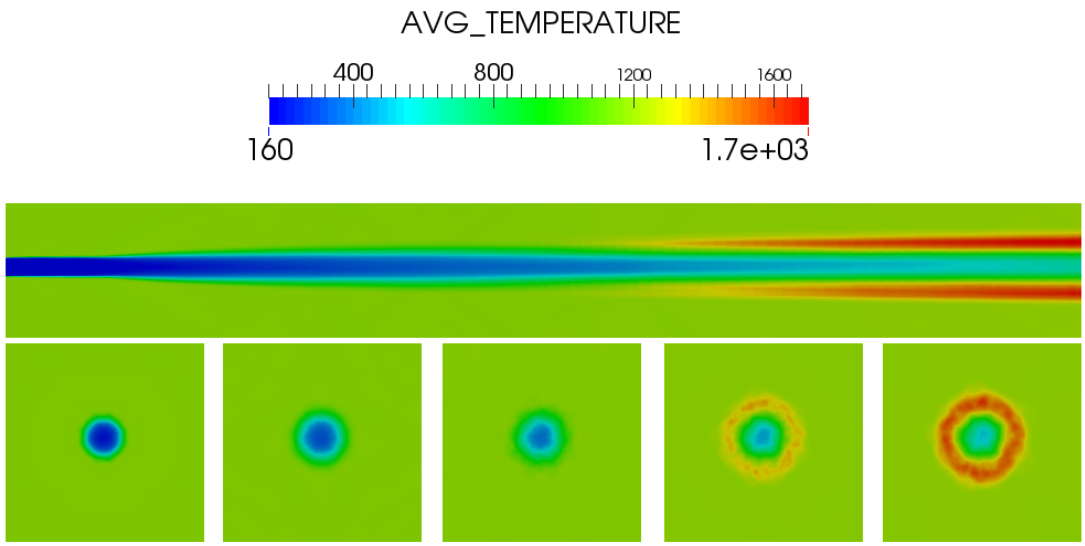

Figure 4.19: Time averaged mid-plane contour of temperature along with selected cross stream contours

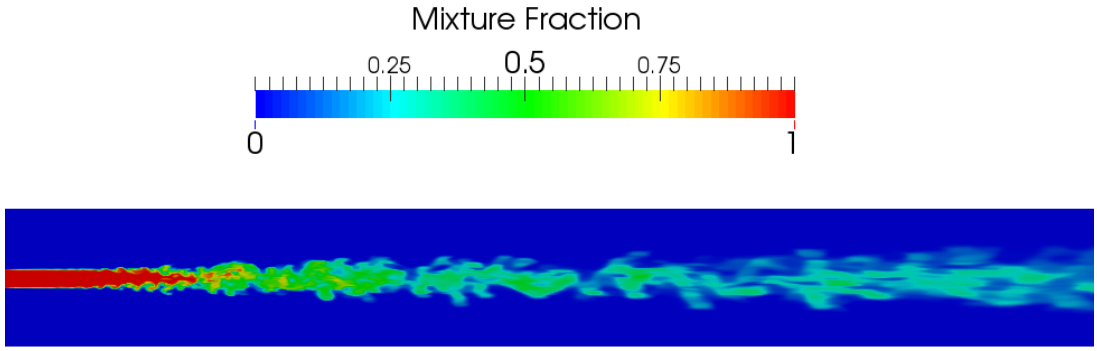

Figure 4.20: Instantaneous mid-plane contour of mixture fraction

It should be emphasises that the low temperatures at $x/D = 35$ do not indicate that this is the lift off height of the flame, nor do they indicate that it happens near this region. At the advective velocities experienced in this experiment, small differences in ignition time, can cause large differences in lift of height. As an example, a ± 0.01ms difference in ignition time can theoretically translate the ignition point approximately ± 2.87D (17.22mm). Further investigation into the non-equilibrium effects and lift-off height will be investigated in §. 4.2.6.

The results from Karaca *et al.* in Fig. 4.17 appear to be of the same order of magnitude as the experimental results. As no other definitive/quantitative data is compared to in Karaca *et al.* to assess chemical non-equilibrium effects or reactive scalar distributions (due to poor experimental results), it is difficult to conclude on the true validity of their results. Based on the contour plots published, it appears that the lift-off height was located significantly farther upstream compared to the results of the present simulations, and thus can explain the higher temperatures at similar axial locations.

Karacas *et al.* closure to the chemical source term is left to diffusion (as DNS normally is) and is a dangerous closure at the published grid resolutions. As the flow is under-resolved compared to a DNS resolution, the sub-grid fluctuations are being left to numerical diffusion which may or may not be modelling them accurately; This potentially giving rise to erroneous production rates. As numerical dissipation is highly dependant on grid resolution in ILES, a varying numerical dissipation will give rise to fictitious sub-grid diffusion of species, which may create large variations in the local temperature. Although the mean flow *may* be captured adequately, the effect of turbulence on sub-grid mixing is poorly represented. Therefore, to conclude that the results of Karacas *et al.* are accurate, would be just as incorrect as saying they are inaccurate, and should be accepted with caution. The conclusions extrapolated from this publication are used merely to strengthen findings of the present study, and are valid only because the comparisons (between Euler and N-S), are based on results from consistent numerics.

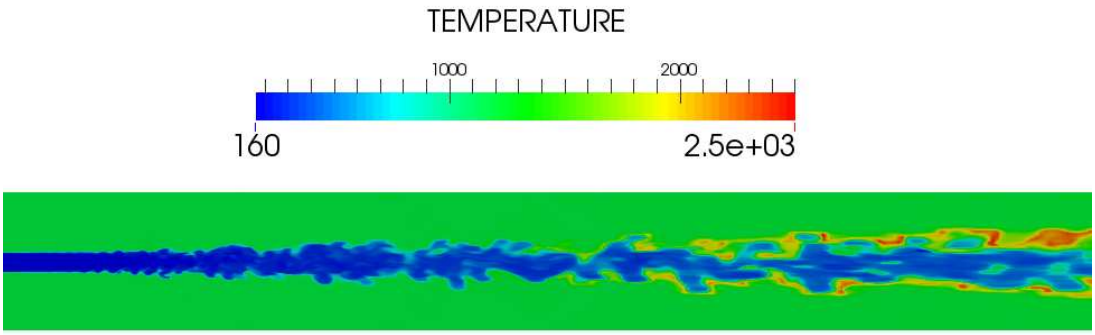

Figure 4.21: Instantaneous mid-plane contour of temperature

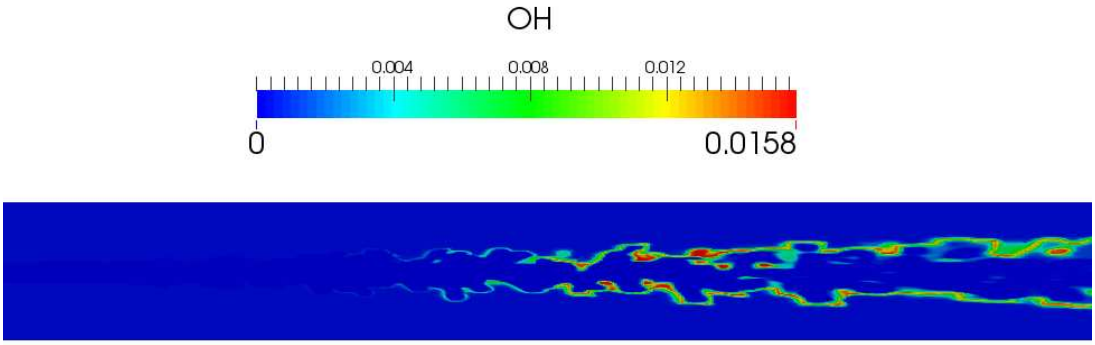

Figure 4.22: Instantaneous mid-plane contour of OH

4.2.5 Effect of Differential Diffusion

In the previous analyses, the importance of the effect of differential diffusion when modelling H_2 was emphasised. In fact, there have been many DNS studies showing the effect of non-unity Lewis numbers on H_2 flames. Doom and Mahesh [24] showed that non-unity Lewis number effects increase the overall temperature and heat release, and can decrease the ignition delay time by up to 64%. Dinesh *et al.* [78] performed a DNS study of an impinging jet (Re=2000), and also concluded an increase in overall combustion temperature. It was also shown, that non-unity Lewis altered the structure of the reacting jet, shifting the combustion mixture towards leaner conditions. The DNS studies of turbulent diffusion flames tend to be limited to low Reynolds flows as the Kolmogorov length scale, scales with Reynolds as shown in Eq. 2.13. Thus, the results of such DNS studies are mainly describing flows who's mixing processes are influenced by both turbulence and diffusion in comparable proportions. In high Reynolds flows, the principle mechanics still remain the same except that mixing tends to be bias/dominated by turbulence while the component of diffusion begins to diminish. Thus, the DNS findings cannot be applied definitively to the present case as the Reynolds number is approximately 100 times larger than the case of Doom and Mahesh. However, they do still provide a good indication of expected behaviour when assuming non-unity species Lewis numbers.

Similar to the Eggers case above, Karaca *et al.* performs a reacting case with a Euler formulation as well as a N-S formulation. In this case, the effect of non-unity Lewis is more strongly visualised though the temperature distributions. The difference in radial temperature distribution at a given axial location between the Euler and N-S simulations, showed the N-S simulation with a temperature 70K higher than the Euler simulation. In addition to this, although not conclusive, instantaneous centre-plane contours of temperature distributions showed the N-S having a slightly earlier ignition point. This difference is far from the immense difference shown in Doom and Mahesh [24] of about 450K, but the difference can perhaps be correlated to the Reynolds number. In flows where turbulent-diffusion time-scale are comparable (low Reynolds number), the temperature differences may be as large as determined by [24], but in cases where turbulent transport is dominant (large Reynolds number), it may be smaller. Referring back to Fig. 4.17, it could therefore be concluded that the lower radial temperatures near $r/D \approx 1.3$ are slightly underestimated due the inaccurate modelling of species molecular transport.

4.2.6 Chemical Non-Equilibrium Effects

The results to this point look promising, but due to the lack of reliable experimental data it is still uncertain whether the implementation models correctly and captures the appropriate non-equilibrium effects. Quantitative comparison to the numerical results of Karaca *et al.* can not be done confidently because of the questionable conslusions provided by the numerical methods used.

In order to analyse the chemical non-equilibrium effects, an additional simulation was conducted. This test case came from ONERA [32] as well, and was identical to the test case

previously analysed, except for the pressure boundary conditions. In this case the pressure for both the jet and the co-flow were 80kPa. The primary focus of this experiment was to assess lift-off height, and does not provide velocity, mass fraction, or temperature data. Along with a quantitative value for flame lift-off height, wall pressure distributions were also published. Ideally a simulation would be conducted assessing the wall pressure distribution, but for the reasons described at the beginning of this section, the wall pressure distribution is not the primary interest and validation tool. The focus of these simulations was to assess combustion phenomena, and therefore the grid was clustered around the central jet regions, limiting the resolution of the wall. As pressure is highly dependant on the grid resolution, the resultant wall pressure distributions were not expected to be very accurate. However, even though the flow in these wall-regions was under resolved, quantitatively the results can be expected to deviate, while qualitatively, similar trends should still be visible as in the experiments.

George *et al.* [32] conduct two experiments; a reacting case and and non-reacting case, where the non-reacting case injects N_2 as opposed to H_2. They use the wall pressure distributions to approximate the lift-off height, and state that autoignition is determined where the two pressure profiles deviate. From the published wall pressure distributions, this occurs at about 0.20m downstream. It is unclear exactly how the authors extrapolated the approximate lift-off height, however they also preform Planar laser-induced fluorescence (PLIF) along with pressure measurements. Therefore, it is probable they use a combination of both the pressure and averaged OH distributions to determine lift-off height. From the experiments, it was stated that lift-off height was about 0.170m downstream from the jet exit. Using the definition of autoignition of Gerliner [34] as being the point of largest OH gradient, the lift-off height for the simulation was approximately 0.165-0.183m. A similar methodology of comparing a reacting case to a non-reacting case could not be applied, as the exact boundary conditions for the non-reacting case where not published and could only be speculated.

The resultant wall pressure of the simulation is shown in Fig. 4.23. Indeed the pressure distribution shown does not resemble the experimental values quantitatively as expected, and the right scale had to be adjusted to better compare the trends of the distributions downstream. However, qualitatively, they match fairly well. Peaks occur roughly in the same regions as the peaks in the experiment, and there is a pressure increase downstream where the experimental pressure appears to begin to increase.

4.2.7 Effect of CMC Grid

One of the more difficult compromises in utilising a conserved scalar methods, is the governing of multiple grids in a given physical domain. When using direct Arrhenius rate closure to the chemical source term (as in DNS), the chemistry is calculated directly on the CFD grid for every CFD cell, and determining the CFD grid is the only requirement. However, at the opposite extreme, when utilising CMC, there is the CFD grid, CMC grid, and conditional space to consider. An accurate solution requires a delicate balance between all these grids as they are coupled. Inaccuracies in one affect all the others.

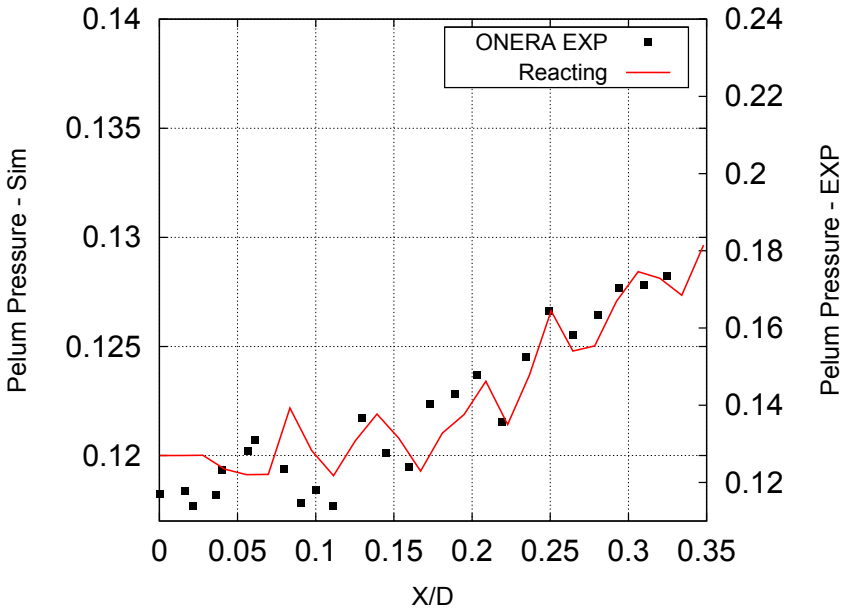

Figure 4.23: Pressure Distribution of LAERTE Experiment

The choice of utilising 4 CFD/CMC in the axial direction was not chosen randomly. Initially, 8 CFD/CMC was chosen for the simulations, however, the results obtained were non-physical and a refinement of the CMC grid by a factor of 2 led to seemingly good results. The CMC grid was not refined beyond this point, as the results for the "medium" resolution were deemed adequate. As a demonstration to the sensitivity of CMC and it's method, the results for the axial 8 CFD/CMC on the medium CFD grid are presented. Fig. 4.24 shows instantaneous mid-plane contours of density, and OH mass fractions. It can be seen that about 1/6th of the way downstream, a discontinuity is formed through the onset of combustion. The density from one cell to the next experiences sudden sharp gradient due to combustion, leading to shock formation which travels downstream. It is obvious that the results obtained are incorrect, as the ignition process should be smoother and, show a gradual transition as seen in Figs. 4.20 to 4.22.

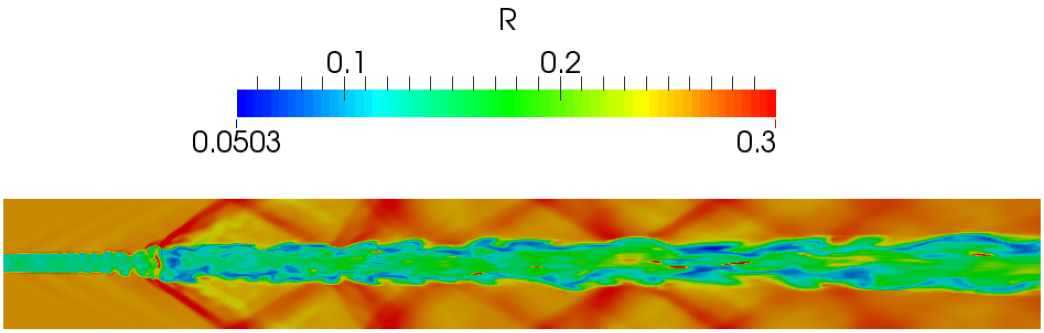

(a) denisty

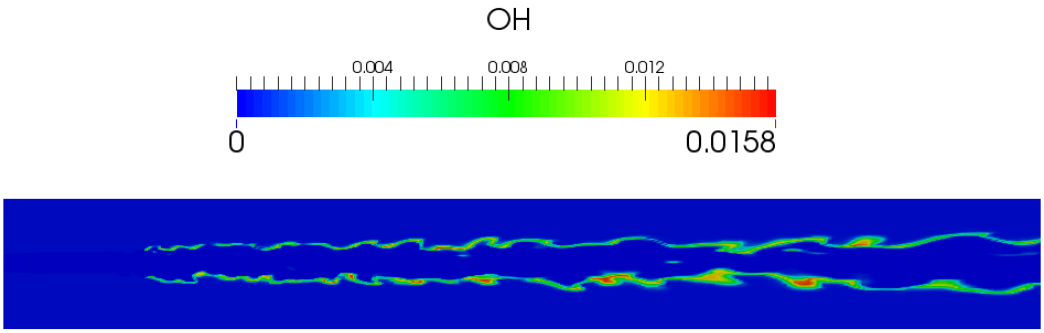

(b) OH

Figure 4.24: Instantaneous centre-plane contour of LAERTE Jet with 8 CFD/CMC

It was evident that this was a transient phenomena as it did not appear immediately, but rather, farther into the simulation. The hypothesised cause of this is due to the CMC grid being too coarse. What is supposedly occurring, is that the CMC cell downstream of the discontinuity is a misrepresentation of true state of the fluid. As a CMC cell covers and models (through conditional averages) a certain physical portion of the domain, any fluid entering that portion of the domain is influenced (and influences) that CMC cell. However, if the CMC cell is too coarse, it governs a larger portion of the physical domain. In reality, the CFD cells in the CMC cell, may not be undergoing similar chemical processes due to chemical non-equilibrium effects, and the advective time-scales present.The result being a conditional average of that entire physical section that includes information from chemically opposite extremes. If the gradients are too sharp in this region of the cell, the average solution from the CMC cell may over predict a solution at one end, and under predict at the other. The CFD cells in the CMC cell at one end may be a region of ”mixing”, and the other end may be “igniting”. If this

is indeed the case, the CMC cell will have information from both extremes being fed into its solution. If the average is bias towards the ignition process, the CMC solution will inevitably tend towards autoignition over time. However as detailed previously, not all CFD cells should be experiencing this autoignition, and if indeed this CMC cell "ignites", the entire conditional solution space of that CMC cell will be that of a burning solution. This translates back to the CFD grid, giving what should be a point in space of mixing, the information that it is in fact burning. If the solution of the CMC cell upwind of the discontinuity tends towards the mixing solution due to the larger influence of the mixing cells, the autoignition process will be seen to occur over a CMC cell interface. This leading to a discontinuity and an unrealistic solution as presented above in Fig. 4.24.

Decreasing the number of CFD/CMC to 4, results in a relatively smoother solution as shown in Figs. 4.20 to 4.22. A more representative indication of the CMC methodology can be seen in Fig. 4.25, where it shows the average cross-stream OH mass fractions for every CFD cell in the axial direction.

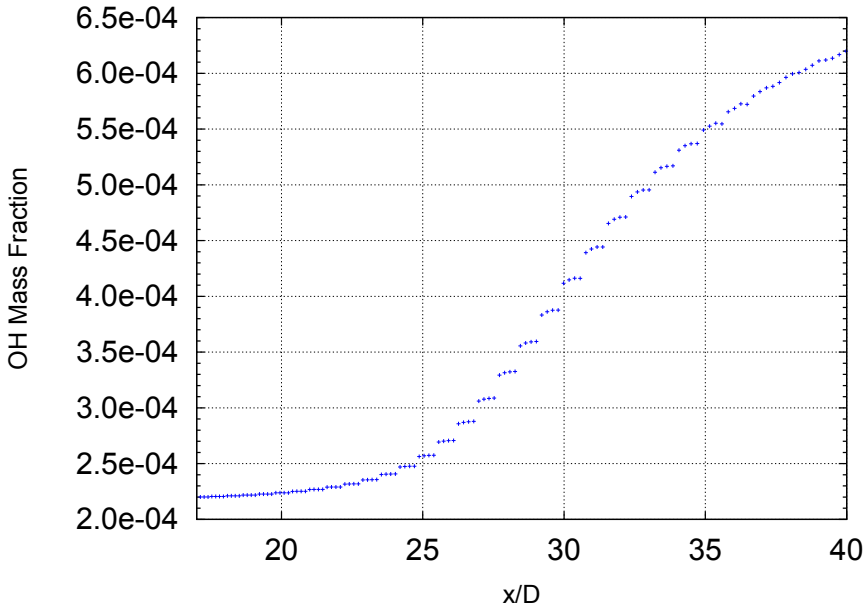

Figure 4.25: Average cross-stream OH mass fraction

Fig. 4.25 shows three distinct regions: before $x/D \approx 20$ and near the exit of the domain, the distribution is smooth, while in-between these two regions, the distribution appears to have small discontinuities. This behaviour can be explained with the aid of the conditional mass fraction profiles. At the locations where the distribution in Fig. 4.25 is smooth, the difference between conditional profiles corresponding to adjacent CMC cells is small. Conversely, the steps are created because the relative difference between conditional profiles for adjacent CMC cell is larger; the larger the difference, the larger the step. The smooth profile with low OH

concentration near the inlet, indicate that this is a region of mixing, while the discontinuous region indicates the region of the jet where transient chemical effects are occurring. In conditional space, this region is where the conditional profiles appear to be evolving the fastest. The smooth profile near the exit on the other hand, would indicate that chemical transient effects have begun to cease, and that beyond this location, combustion would begin to be established. It is expected that if the domain was larger, the OH distribution would eventually level off indicating a steady-state flame.

The CMC cells can be clearly seen in this image by the 4 points per "cluster" representing the 4 CFD/CMC. One would expect that if decreasing to 2 CFD/CMC, the piecewise distributions of the OH mass fractions in the high gradient regions would be halved, creating a smoother profile. The extreme case would correspond to 1 CFD/CMC, which should give the smoothest solution, however, at this resolution, the advantage of CMC (and conditional averaging) diminishes, and the solution process approaches a similar method to the presumed PDF methods. Additionally, at these resolutions, CMC becomes very expensive, and the main advantage of modelling sections of the domain through conditional averages becomes questionable.

Naturally, increasing the CFD resolution will have the effect of increasing the resolution of the CMC grid as well. This will make the physical size of the CMC cells smaller, and therefore, the "steps" seen in Fig. 4.25, may also become smoother. However, it can also be argued that this increased CMC resolution is only necessary in regions where the conditional profiles are evolving the quickest. The upstream portion of the domain has the largest cluster of CFD cells, and the downstream, the lowest, yet the profiles in these regions are smooth. This would indicate that the CMC grid in these regions is adequately resolved for the gradients experienced. Hence, the increasing of the resolution of the CMC grid to avoid these steps and obtain a globally smooth solution, may come at cost of decreased efficiency, and wasted computation in the upstream and downstream regions. Currently the implementation of CMC only allows a predetermined ratio of CFD to CMC cells in the three principle directions. Therefore, what is needed, is the ability to decouple the algebraic dependence of CMC to CFD, and allow a variable CMC grid. This would enable adequate clustering of the CMC grid in regions of expected high gradients, while reducing the resolution in regions of smoother gradients (i.e steady-state combustion regions).

Nevertheless, keeping a modest resolution of 4 CFD/CMC still results in miniature discontinuities, but does not affect the flow as in the case of 8 CFD/CMC. It is uncertain if these discontinuities exist in flows of lower advective velocities, or if it is a new phenomena present only in the case of supersonic flows. To the knowledge of the author, detailed distributions such as this have never been published for subsonic flows, however, it is expected that solutions in subsonic flows are much smoother. If 1 CFD/CMC is required for a smooth solution, this could certainly be a limitation of CMC and its application to supersonic reacting flows, or indication that better modelling is required.

The hypothesised term that would require better modelling would be the conditional velocity. The spatial advection of a conditional quantity (term C_1 in §. 3.1.2) passes information of conditional scalars from a conditional bin in one CMC cell, to the same bin in another CMC

cell. The fact that there exists a discontinuity in scalars at the CMC cell interface indicates that perhaps information is not being passed correctly, or that for supersonic flow, this term must be treated in a different manner.

Kinetic Energy Dissipation

The energy spectra of the coarse and fine simulations are shown in Fig. 4.26. The energy spectra was determined based on the time history of a point after the flow was established (approximately after 3 flow-through times). As this was a temporal signal, the Taylor Hypothesis of frozen turbulence was applied in order to convert this to a spatial signal to obtain the spectra in terms of wavenumber. Ingenito and Bruno [44] performed a dimensional analysis on kinetic energy density, with a dependence on density, dissipation, and wavenumber. They found that for flows dependant on density (compressible flows), the dissipation no longer follows a -5/3 slope but a steeper -8/3 instead. The reader is encouraged to refer to [44] for further details. Fig. 4.26 shows that both spectra have a small region where they follow the -5/3 dissipation, but a larger region where they follow -8/3.

To show the effect of the stretched grid and varying local resolution, Fig. 4.27 shows the spectra at three different axial locations on the centreline for the medium simulation. The downstream point that corresponds to the locally coarser grid location, captures more -5/3 and less -8/3, than the upstream location where the spectra shows a larger -8/3 region. It is uncertain whether the -8/3 slope is an appropriate indication of the dissipation rate in these simulations, but the results show fair agreement to this hypothesis. It is known that the -5/3 is an idealised dissipation rate for incompressible homogeneous turbulent flows, and the recurring theme in literature is that compressible flows do not follow -5/3 slope. In addition to the -8/3 decay of Ingenito and Bruno [44], Passaro *et al.* [68] propose a -11/3 decay for weakly turbulent hypersonic flows. Regardless of the dissipation rates experienced in the present simulations or those hypothesised in literature, the results in the presented figures show that the simulations are successfully capturing dissipation and some apart of the inertial range.

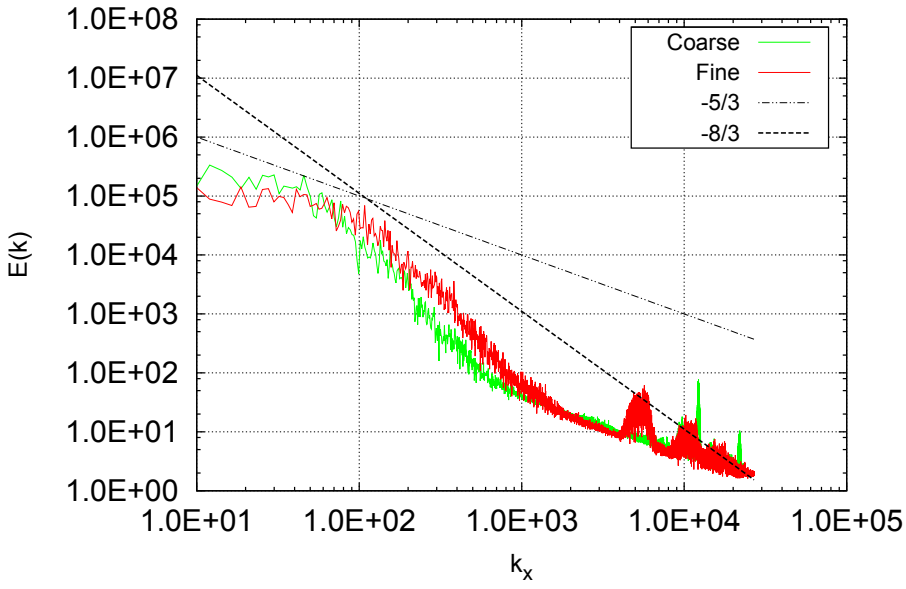

Figure 4.26: Kinetic energy spectra for coarse and fine simulations at center of computational domain

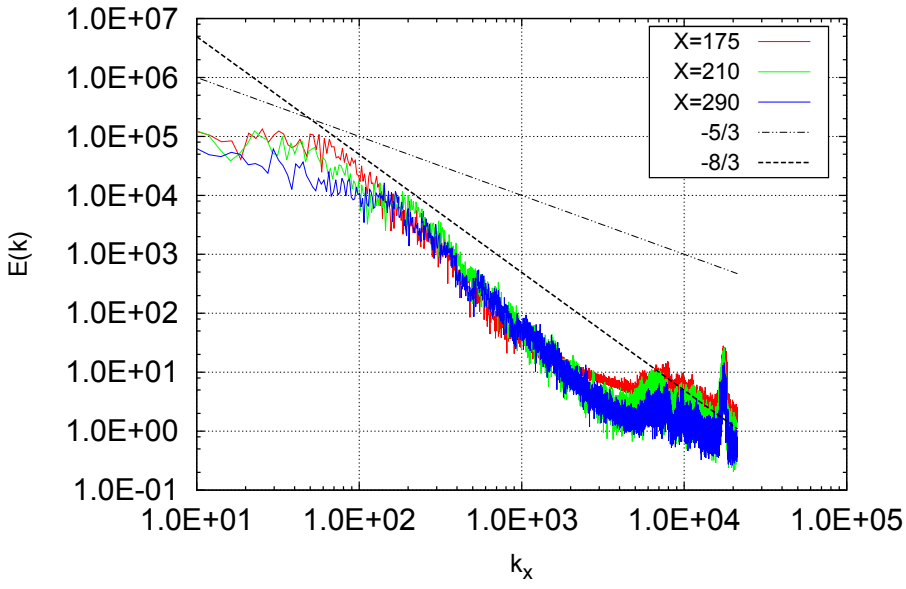

Figure 4.27: Kinetic energy spectra at 3 different axial centreline locations for the medium resolution

CHAPTER 5

Conclusion

The study presented a first approach for the novel application of the conditional moment closure model (CMC) for modelling supersonic combustion. The combustion model was applied to a fully compressible, shock capturing flow solver that utilised a finite volume based Godunov scheme, with MUSCL 5^{th} reconstruction, and low Mach number correction. The time integration used, was a robust TVD, 3-step, 2^{nd} order Runge-Kutta method. The study was broken into two steps: the first assessing the ability for the solver to capture supersonic turbulent mixing. The second step assessing the ability for the solver to model supersonic reacting flows.

This study firstly presented results for a non-reacting case where a hydrogen jet was injected into a supersonic co-flow at temperatures well below hydrogen autoignition temperatures. This test case was chosen in an attempt to validate the implementation of the CMC equations, and their applicability to model supersonic mixing. From the results it was seen that velocity appeared to decay quickly in certain regions of the jet, but still followed the trends of the experiential results. This excess jet decay was attributed to inaccurate modelling of mixture viscosity. Moreover, the H_2 mass fractions seemed to fit the experimental data well, with only a slight discrepancy downstream. This downstream discrepancy was attributed to the fact that the grid clustering functions used in this study was overly bias to the inlet portion of the domain. Any increases in grid resolution did not significantly increase the downstream resolution as they did to the upstream domain. Additionally, a small contribution to this discrepancy was placed on the misrepresented molecular transport utilised in the current numerical formulation of CMC.

Secondly, a supersonic lifted jet was presented. It was shown that too coarse of a CMC grid can cause un-realistic behaviour. Refining the CMC grid removed the non-physical behaviour, but still showed miniature discontinuances at the CMC cell interfaces when cross-stream averaging was applied. To achieve a smoother solution, further refinement of the CMC grid is hypothesised to be needed. However, further refinement begins to remove the primary advantage of CMC, and therefore could represent a practical limitation of this method in supersonic flows. It is also unclear if more accurate modelling of CMC terms is required and is in fact, the cause of these miniature discontinuities. The non-equilibrium effect, namely, flame lift-off height were also studied. A lift-off height of about 0.165-0.183m was calculated based on peak gradient of OH production, which compares well to an experimental lift-off height of about 0.170m. The similar lift-off height provides good confirmation to the feasibility of this method,

and gives reassurance that the results obtained for the reacting case may not be far off from the true flow.

The reactive scalar profiles of these simulations were more difficult to analyse as the experimental data was not reliable, nor readily available. However, qualitatively, trends similar to the numerical results of Karaca *et al.* and the experiment were shown. If the errors of the experiment were quantified, a better conclusion on the accuracy of the results of the simulations could have been made. Generally, the temperature results of the present simulations are lower than the presumably overestimated experimental results. This hints that the presented results could in fact be similar to the experimental conditions.

The recurring theme in the analyses of the results, was the influence of differential diffusion. It is well known in the combustion community that assuming constant unity Lewis number in reacting flows is a big assumption, but is commonly used for simplicity nonetheless. Variable Lewis is always important to model, as it allows for a better representation of the molecular transport. Based on the results of Karacas *et al.*s' Euler vs N-S study, and the results presented in this study, the effects of differential diffusion at these Reynolds numbers are not the same as those experienced in Low Reynolds flows and in the presented DNS studies. Therefore, at these Reynolds numbers, the influence of differential diffusion on the large scale flow field may not be as strong as some authors indicate. However, this is not to say that diffusion does not play an important role. The results shown from the same sources that the previous conclusion was deduced from, that there exist small differences which are concluded to be *due* to differential diffusion effects. Perhaps as the shift from advection-diffusion controlled mixing at low Reynolds numbers, to a more turbulent biased mixing that occurs at high Reynolds numbers, the influence of differential diffusion on the large scale flow field becomes smaller, and the assumption of constant/unity Lewis, is not as inaccurate as was previously believed.

Overall, the CMC method for supersonic combustion seems feasible, as good agreement was obtained from the limited data available. Naturally, the present work does not confirm, or refute, the detailed accuracy of the proposed method as concluding this requires better analysis and data. It does however, give confirmation to its feasibility and application, and gives rise to potential modelling uncertainties and areas of improvement both in the CHOC code, and also the CMC method. Potential drawbacks of the methods are also presented, such as CMC resolution issues, but it is uncertain whether these limitations are a function of the model or of the manner in which the model has been used. These vague conclusions also illustrate the need for more reliable, simple experimental data for supersonic reacting flows.

5.1 Future Research/Work

CMC

- To be certain on the validity of using CMC at is frozen limit, a test case similar to [27] of single-species mixing should be conducted to validate the method by removing the

uncertainty of variable molecular diffusion. If hydrogen is to be further investigated, CMC formulation needs to be expanded to accept non-unity Lewis.

- In this implementation, the conditional velocity is assumed to be its unconditional counterpart. Typically, the contribution of this term is not as dominant as the diffusion term, or the source term, however, when approaching supersonic velocities, the influence of advection increases. Using this closure for this term was deemed adequate for most CMC-LES simulations as the gradient model [58] has not been validated for LES to date. This closure may have been satisfactory for the low speed, subsonic flows previously analysed with CMC, but it is unclear if different modelling is required, or if this assumption holds for high speed flows.

- The scalar dissipation model needs to be further investigated. The scalar dissipation modelling used in this study assumed the unconditional scalar dissipation is the conditional scalar dissipation. Other popular models are the Amplitude Mapping Closure(AMC) [67] and the Girimaji model [36], where explicit conditioning of the scalar dissipation is used to condition the scalar dissipation before conditional averaging. Simulations should be conducted with these scalar dissipation models to assess their influence.

- To test the hypothesis of the smoothness of the CMC solution illustrated in Fig. 4.25, a simulation utilising 1 CFD/CMC should be conducted to isolate whether this effect comes from a coarse CMC solution or inadequate modelling.

  - A block structured CMC grid should be implemented. This would remove the current algebraic dependence of the CMC grid on the CFD grid, and clustering of CMC cells in regions of expected large gradients can result in a smoother solution while still maintaining the advantage of CMC's modelling method

- A simulation utilising a 3D CMC grid should be conducted. Although a 1D-CMC grid is sufficient in the case of an axis-symmetric jet, it may also suppress asymmetric non-equilibrium effects such as extinction and re-ignition at different radial locations of the jet.

- Clustering of conditional space around stoichiometry would greatly reduce computational time, as it has been stated that when clustering, as few as 50 points in conditional space are needed for accurate results

- In the present formulation, term R_1 in Eqs. 3.5 and 3.6 is neglected. This assumption was based on a methane-air flame however, [18] shows that this term is not as negligible as previously assumed.

CFD

- Another major area of concern is the turbulent inflow used. It was shown by Rana [77] that white noise turbulence is a poor approximation to the perturbations required for accurate

turbulence generation. However, in the time frame of this study, it was not a priority, but more to demonstrate the validity of this model and method. The next steps should involve implementing a synthetic turbulence generator.

- Given the turbulence model, the present simulations should have been run with a similar time step at all resolutions. This would have reduced the influence of the white noise turbulence on the relative resolution level of the grid, and would have eliminated the changing boundary conditions upon grid refinement. It would have kept the inflow turbulence as consistent as possible.

Bibliography

[1] "Web Reference: Image downloaded 13th November 2012 from: http://commons.wikimedia.org/wiki/File:KHI.gif".

[2] "Web Reference: Image downloaded 13th November 2012 from: http://photojournal.jpl.nasa.gov/catalog/PIA06502".

[3] "Web Reference: Image downloaded 23rd November 2012 from: http://www.dfrc.nasa.gov/Gallery/Photo/X-43A/HTML/EC04-0092-32.html".

[4] "Web Reference: Image downloaded 29th October 2012 from: http://www.af.mil/shared/media/photodb/photos/100520-F-9999B-111.jpg".

[5] "Web Reference: Image downloaded 29th October 2012 from: http://www.uq.edu.au/hypersonics/index.html?page=19501".

[6] "Web Reference: Image downloaded 31st October 2012 from: http://modernistcuisine.com/wp-content/uploads/2010/12/Coffee-Cream.jpg".

[7] **Anderson, J.** *Hypersonic and High-Temperature Gas Dynamics, Second Edition*. American Institute of Aeronautics & Astronautics, 2006.

[8] **Ayache, S. and Mastorakos, E.** "Conditional Moment Closure /Large Eddy simulation of the Delft-III Natural Gas Non-premixed Jet Flame". *Flow, Turbulence and Combustion*, 2012:88(1-2):pp. 207–231.

[9] **Berglund, M., Fedina, E., and Fureby, C.** "Finite rate chemistry Large-eddy simulations of self–ignition in a supersonic combustion ramjet". *AIAA*, 2010:48:pp. 540–550.

[10] **Bilger, R.W.** "Advanced Laser Diagnostics: Implications of Recent Results for Advanced Combustor Models". *Aerothermodynamics in Combustors*, 1992:pp. 3–16.

[11] **Bilger, R.W.** "Conditional Moment Closure for turbulent reacting flows". *Physics of Fluids*, 1993:5:pp. 436–444.

[12] **Birbaud, A. and Pitsch, H.** "Compressible solvers for combustion noise simulations". *Center for Turbulence Research Annual Research Briefs*, 2007:pp. 265–275.

[13] **Branley, N. and Jones, W.** "Large eddy simulations of a turbulent non-premixed flame". In *Proceedings of the 11th Symposium on Turbulent Shear Flows, Grenoble, France*, 1997: pp. 21.1–21.6.

[14] **Burke, S.P. and Schumann, T.E.W.** "Diffusion Flames". *Industrial & Engineering Chemistry*, 1928:20(10):pp. 998–1004.

[15] **Chen, J., Chang, W., and Koszykowski, M.** "Numerical Simulation and Scaling of NOx Emissions from Turbulent Hydrogen Jet Flames with Various Amounts of Helium Dilution". *Journal of Combustion Science and Technology*, 1995:110-111:pp. 505–529.

[16] **Cheng, T.S., Wehrmeyer, J., Pitz, R.W., Jarrett, O., and Northam, G.** "Raman Measurement of Mixing and Finite Rate Chemistry in a Supersonic Hydrogen-Air Diffusion Flame". *Combustion and Flame*, 1994:99:pp. 357–393.

[17] **Colin, O., Ducros, F., Veynante, D., and Poinsot, T.** "A thickened flame model for large eddy simulations of turbulent premixed combustion". *Physics of Fluids*, 2000:12:pp. 1843–1863.

[18] **Cook, W.A.** "Enthalpy diffusion in multicomponent flows". *Physics of Fluids*, 2009:21.

[19] **Cuenot, B. and Poinsot, T.** "Effects of curvature and unsteadiness in diffusion flames. Implications for turbulent diffusion flames". *Proceedings of the Combustion Institute*, 1994:25:pp. 1383–1390.

[20] **Davidson, P.A.** *Turbulence: an Introduction for Scientists and Engineers*. Oxford University Press, 2004.

[21] **Desjardins, O., Blanquart, G., Balarac, G., and Pitsch, H.** "High-order conservative finite difference scheme for variable density low Mach number turbulent flows". *Journal of Computational Physics*, 2008:227:pp. 7125–7159.

[22] **Devaud, C. and Bray, K.** "Assessment of the applicability of conditional moment closure to a lifted turbulent flame: first order model". *Combustion and Flame*, 2003:132:pp. 102–114.

[23] **Domingo, P., Vervisch, L., and Veynante, D.** "Large-eddy simulation of a lifted methane jet flame in a vitiated coflow". *Combustion and Flame*, 2008:152:pp. 415–432.

[24] **Doom, J. and Mahesh, K.** "DNS of auto-ignition in turbulent diffusion H2/air flames". *47th AIAA Aerospace Sciences Meeting Including The New Horizons Forum and Aerospace Exposition 5-8 January, Orlando, Florida, USA, AIAA Paper 2009-240*, 2009:.

[25] **Drazin, P. and Reid, W.** *Hydrodynamic Stability*. Cambridge University Press, 2004.

[26] **Eggers, J.** "Turbulent mixing of coaxial compressible hydrogen-air jets". *Tech. rep.*, NASA TN D-6487, 1971.

[27] **Eggers, J. and Torrence, M.** "An Experimental Investigation of the Mixing of Compressible -Air Jets in a Coaxial Configuration". *Tech. rep.*, NASA - TN D-5315, 1969.

[28] **Fairweather, M. and Woolley, R.** "first-order conditional moment closure modeling of turbulent, non-premixed hydrogen flames". *Combustion and Flamem*, 2003:133:pp. 393–405.

[29] **Floyd, J., Kempf, A., Kronenburg, A., and Ram, R.** "A simple model for the filtered density function for passive scalar combustion LES". *Combustion Theory and Modelling*, 2009:13(4):pp. 559–588.

[30] **Gardner, D. and Hannemann, K.** "Evaluation of Full-Engine Scramjet Technology". *Tech. rep.*, German Aerospace Center, DLR, 2004.

[31] **Garnier, E., Mossi, M., Sagaut, P., Comte, P., and Deville, M.** "On the use of shock-capturing schemes for large-eddy simulation". *Journal of Computational Physics*, 1999: 153:pp. 273–311.

[32] **George, E., Sabel'nikov, V., and Tretyakov, P.** "Numerical Simulations of Self-Ignition of Hydrogen-Hydrocarbons Mixtures in a Hot Supersonic Air Flow". *42nd AIAA/ASME/SAE/ASEE Joint Propulsion Conference and Exhibit 9-12 July, Sacramento California, USA, AIAA Paper 2006-4611*, 2006:.

[33] **Gerlinger, P.** *Numerische Verbrennungssimulation*. Springer, 2005.

[34] **Gerlinger, P., Nold, K., and Aigner, M.** "Investigation of Hydrogen-Air Reaction Mechanisms for Supersonic Combustion". *AIAA*, 2008:.

[35] **Giacomazzi, E., Bruno, C., and Favini, B.** "Fractal modeling of turbulent mixing". *Combustion Theory and Modelling*, 1999:3:pp. 637–655.

[36] **Girimaji, S.** "Assumed B-pdf model for turbulent mixing: Vadation and extension to multiple scalar mixing". *Combustion Science and Technology*, 1991:78:pp. 177–196.

[37] **Glassman, I. and Yetter, R.A.** *Combustion*. Elsevier Inc, 4th ed., 2008.

[38] **Grinstein, F., Margolin, L., and Rider, W.** *Implicit large eddy simulation: computing turbulent fluid dynamics*. Cambridge University Press.

[39] **Harten, A.** "High resolution schemes for hyperbolic conservation laws". *Journal of Computational Physics*, 1983:49:pp. 357–393.

[40] **Hinze, J.** *Turbulence: An Introduction to Its Mechanisms and Theory*. McGraw-Hill Book Company Inc, 1959.

[41] **Hoffmann, Klaus, A. and Chiang, S.T.** *Computational Fluid Dynamics Vol.III*. Engineering Education System, 4th ed., 2000.

[42] **Ihme, M. and Pitsch, H.** "Prediction of extinction and reignition in non-premixed turbulent flames using a flamelet/progress variable model 2. applications in LES of Sandia flames D and E". *Combustion and Flame*, 2008:155:pp. 90–107.

[43] **Ingenito, A. and Bruno, C.** "Recent Progress Towards a Large Eddy Simulation Code for Jet Aeroacoustics". *AIAA Paper 2002-2598*, 2002:.

[44] **Ingenito, A., Bruno, C., and Cecere, D.** "LES of the HyShot scramjet combustor". In *48th AIAA Aerospace Sciences Meeting Including the New Horizons Forum and Aerospace Exposition*, 2010: .

[45] **Jachimowski, C.** "An Analytical Study of the Hydrogen-Air Reaction Mechanism With Application to Scramjet Combubstion". *Tech. rep.*, Langley Research Center, NASA, 1988.

[46] **Karaca, M., Lardjane, N., and Fedioun, I.** "Implicit Large Eddy Simulation og high-speed non-reacting and reacting air/H2 jets with a 5th order WENO scheme". *Computers and Fluids*, 2012:62:pp. 25–44.

[47] **Karl, S., Hannemann, K., Mack, A., and Steelant, J.** "CFD Analysis of the HyShot II Scramjet Experiments in the HEG Shock Tunnel". *15th AIAA International Space Planes and Hypersonic Systems and Technologies Conference, Ohio*, 2008:AIAA-2548:pp. 1–16.

[48] **Kelvin, R.** "Hydrokinetic Solutions and Observations". *Phil. Mag.*, 1871:42:pp. 362–377.

[49] **Kerstein, A.R.** "Linear eddy model of turbulent scalar transport and mixing". *Combustion Science and Technology*, 1988:60:pp. 391–421.

[50] **Kerstein, A.R.** "Linear-eddy modelling of turbulent transport. Part 6. Microstructure of diffusive scalar mixing fields". *Journal of Fluid Mechanics*, 1991:231:pp. 361–394.

[51] **Kerstein, A.R.** "Linear-eddy modelling of turbulent transport. Part 4. Structure of Diffusion Flames". *Combustion Science and Technology*, 1992:81:pp. 75–96.

[52] **Kerstein, A.R.** "Linear-eddy modelling of turbulent transport. Part 7. Finite Rate Chemistry and multi-stream Mixing". *Journal of Fluid Mechanics*, 1992:240:pp. 289–313.

[53] **Kim, I. and Mastorakos, E.** "Simulation of Turbulent Lifted Jet Flame with Two-Dimensional Conditional Moment Closure". *Proceedings of the Combustion Institute*, 2005:30:pp. 911–918.

[54] **Kim, K. and Kim, C.** "Accurate, Efficient and Monotonic Numerical Methods for Multi-Dimensional Compressible Flows, Part II: Multi-Dimensional Limiting Process". *Journal of Computational Physics*, 2005:208:pp. 570–615.

[55] **Kim, S. and Huh, K.** "Use of Conditional Moment Closure Model to Predict NO Formation in a Turbulent CH4/H2 Flame over a Bluff-Body". *Combustion and Flame*, 2002: 130:pp. 94–111.

[56] **Kim, S., Huh, K., and Tao, L.** "Application of the elliptic conditional moment closure moidel to a two-dimensional non-premixed methanol bluff-body flame". *Combustion and Flame*, 2000:28:pp. 185–191.

[57] **Klimenko, A.** "Multicomponent diffusion of various admixtures in turbulent flow". *Journal of Fluid Dynamics*, 1990:25:pp. 327–334.

[58] **Klimenko, A. and Bilger, R.** "Conditional moment closure for turbulent combustion". *Progress in Energy and Combustion Science*, 1999:25:pp. 595–687.

[59] **Koo, H., Donde, P., and Raman, V.** "LES-based Eularian PDF approach for the simulation of Scramjet Combustors". *Proceedings of the Combustion Institute*, 2013:34:pp. 2093–2100.

[60] **Kronenburg, A.** "Double conditioning of reactive scalar transport equations in turbulent nonpremixed ames". *Physics of Fluids*, 2004:16:pp. 2640–2648.

[61] **Moin, P. and You, D.** "A Dynamic Global-Coefficient Subgrid-Scale Model for Large-Eddy Simulation of Turbulent Scalar Transport in Complex Geometries". *Tech. rep.*, Center for Turbulence Research, Stanford University, 2007.

[62] **Molkov, V., Verbecke, F., and Makarov, D.** "LES of hydrogen-air deflagrations in a 78.5m tunnel". *Journal of Combustion Science and Technology*, 2008:180:pp. 796–808.

[63] **Moureau, V. andBerat, C. and Pitsch, H.** "An efficient semi-implicit compressible solver for large-eddy simulations". *Journal of Computational Physics*, 2007:226:pp. 1256–1270.

[64] **Navarro-Martinez, S. and Kronenburg, A.** "LES-CMC simulations of a tubulent bluff-body flame". *Proceedings of the Combustion Institute*, 2007:11(4):pp. 527–552.

[65] **Navarro-Martinez, S. and Kronenburg, A.** "LES-CMC simulations of a lifted methane flame". *Proceedings of the Combustion Institute*, 2009:32:pp. 1509–1516.

[66] **Navarro-Martinez, S., Kronenburg, A., and DiMare, F.** "Conditional Moment Closure for Large Eddy Simulation". *Flow, Turbulence and Combustion*, 2005:75:pp. 245–274.

[67] **O'Brien, E. and Jiang., T.** "The conditional dissipation rate of an initially binary scalar in homogeneous turbulence." *Physics of Fluids*, 1991:3(12):pp. 3121–3123.

[68] **Passaro, A., Biagioni, L., and d'Agostino, L.** "Compressibility Effects in Weakly Turbulent Hypersonic Flow Fields". *EUROPEAN SPACE AGENCY -PUBLICATIONS- ESA*, 2002:487:pp. 709–716.

[69] **Pereira, F.N., Andreis, G.S.L., Bortoli, A.L.D., and Marcílio, N.R.** "Analyitical-numerical solution for turbulent jet diffusion flames of hydrogen". *Journal of Mathematical Chemistry*, 2012:pp. 1–13.

[70] **Peters, N.** "Local quenching due to flame stretch and non-premixed turbulent combustion". *Combustion Science and Technology*, 1983:30:pp. 1–17.

[71] **Peters, N.** "Laminar diffusion Flamelet models in non-premixed turbulent combustion". *Progress in Energy and Combustion Science*, 1984:10:pp. 319–339.

[72] **Pitsch, H.** "Improved pollutant predictions in large eddy simulations of turbulent non-premixed combustion by considering scalar dissipation rate fluctuations." In *Combustion Institute*, 2002: pp. 1971–1978.

[73] **Pitsch, H., Chen, M., and Peters, N.** "Unsteady flamelet modelling of turbulent hydrogen/air diffusion flames". In *Combustion Institute*, vol. 27, 1998: pp. 1057–1064.

[74] **Pitsch, H. and Fedotov, S.** "Investigation of scalar dissipation rate fluctuations in non-premixed turbulent combustion using a stochastic approach". *Combustion Theory and Modelling*, 2001:5:pp. 41–57.

[75] **Poinsot, T. and Veynante, D.** "Theoretical and Numerical Combustion":.

[76] **Pope, S.B.** *Turbulent Flows*. Cambridge University Press, 2000.

[77] **Rana, Z.A.** "Implicit LES of Turbulent Compressible High-Speed Flows with Transverse Jet Injection by". Ph.D. thesis, Cranfield University, 2011.

[78] **Ranga Dinesh, K., Jiang, X., van Oijen, J., Bastiaans, R., and de Goey, L.** "Hydrogen-enriched nonpremixed jet flames: Effects of preferential diffusion". *International Journal of Hydrogen Energy*, 2013:38:pp. 4848–4863.

[79] **Roomina, M. and Bilger, R.W.** "Conditional Moment Closure Modelling of a Turbulent Methane Air Jet Flame". *Combustion and Flame*, 2001:125:pp. 1176–1195.

[80] **Sankaran, V., Drozda, T.G., and Oefelein, J.C.** "A tabulated closure for turbulent non-premixed combustion based on the linaer eddy model". *Proceedings of the Combustion Institute*, 2009:32:pp. 1571–1578.

[81] **Segal, C.** *The Scramjet Engine: Processes and Characteristics*, 2009.

[82] **Shu, C.W.** "Total-variation-diminishing time discretizations". *SIAM Journal on Scientific and Statistical Computing*, 1988:9:pp. 1073–1084.

[83] **Smagorinsky, J.** "General circulation experiments with the primitive equations". *Monthly Weather Review*, 1963:91:pp. 99–164.

[84] **Smooke, M. and Giovangigli, V.** "Formulation of the premixed and non-premixed test problems". *Lect. Notes Physics*, 1991:384:pp. 1–28.

[85] **Thornber, B.** "Implicit Large Eddy Simulation for Unsteady Multi-Component Compressible Turbulent Flows". Ph.D. thesis, Cranfield University, 2007.

[86] **Thornber, B., Bilger, R., Masri, A., and Hawkes, E.** "An Algorithm for LES of premixed compressible flows using the Conditional Moment Closure model". *Journal of Computational Physics*, 2011:.

[87] **Thornber, B., Drikakis, D., Williams, R., Mosedale, A., and Youngs, D.** "An Improved Reconstruction Method for compressible Flows with Low-Mach Number Features". *Journal of Computational Physics*, 2008:227(10):pp. 4873–4894.

[88] **Thornber, B., Drikakis, D., Youngs, D., and Williams, R.** "On Entropy Generation and Dissipation of Kinetic Energy in High-Resolution Shock-Capturing Schemes". *Journal of Computational Physics*, 2008:227(10):pp. 4853–4872.

[89] **Thornber, B., Mosedale, A., Drikakis, D., Williams, R., and Youngs, D.** "An improved reconstruction method for compressible flows with low Mach number features". *Journal of Computational Physics*, 2008:227:pp. 4873–4894.

[90] **Toro, E.** *Rieman Solvers and Numerical Methods for Fluid Dynamics*. Springer-Verlag, Cambridge, 1997.

[91] **Torrez, S., Driscoll, J., Matthias, I., and Fotia, M.** "Reduced Order Modeling of Turbulent Reacting Flows with Application to Ramjets and Scramjets". *Journal of Propulsion and Power*, 2011:27(2):pp. 371–382.

[92] **Veynante, D. and Vervisch, L.** "Tubulent Combustion Modelling". *Progress in Energy and Combustion Science*, 2002:28:pp. 193–266.

[93] **Vreman, B., Geurts, A., and Kuerten, H.** "A priori tests of large eddy simulation of the compressible plane mixing layer". *Journal of Engineering and Math*, 1995:29:pp. 299–327.

[94] **Williams, F.** *Combustion Theory*. Benjamin Cummings, Menlo Park, CA,, 1985.

APPENDIX **A**

Chemical Mechanism - Backward Rates

When utilising a published chemical mechanism, it is common for only the forward rates to be published. If detailed finite-rate chemistry is to be used in the combustion modelling, it is necessary for the backward rates to be calculated for the individual reactions. In order to increase efficiency, a program was developed to aid in the process of calculating the reverse rates, as the process of calculating the reverse reactions rates can be a tedious especially if the mechanism consist of hundreds of reactions. However, since the objectives of this study did not specify the mechanism to be used, the program was extended to allow the calculation of the reverse reaction rates for any chemical mechanism of n of reactions. The early version of this code is limited to basic reaction and cannot analyse complex chemical mechanisms with fall-off reactions. The expansion of this program to generic simple mechanisms was considered to be beneficial for future studies where comparisons of different mechanisms is required.

For consistency and illustrative purposes, consider the reaction,

$$\alpha A + \beta B \rightleftharpoons \eta C + \delta D \tag{A.1}$$

it is convenient to know the equilibrium constant for such a reaction because it would allow for the determination of specific information about the products of the species to be known at equilibrium, given a set of initial conditions.

There are two methods to calculate the equilibrium constant. One is using the partial pressures, the other is using the molar concentrations. The pressure based equilibrium constant can be calculated by

$$K_p = \frac{(C)^{\eta}\dot{(}D)^{\delta}}{(A)^{\alpha}\dot{(}B)^{\beta}} \tag{A.2}$$

where the terms in parenthesis are the partial pressures of the products and reactants. It is important to note that the partial pressures used in Eq. A.2 are only those of gaseous phase compounds. From the ideal gas law, knowing that

$$PV = nRT \tag{A.3}$$

we can conclude that the partial pressure is equal to the molar concentration multiplied by a concentration correction in the form RT. Therefore Eq. A.2 can be reformulated to represent

the equilibrium constant considering the molar concentrations of the reaction.

$$K_p = \frac{[C]^{\eta} \cdot [D]^{\delta}}{[A]^{\alpha} \cdot [B]^{\beta}} \frac{RT^{\eta} \cdot RT^{\delta}}{RT^{\alpha} \cdot RT^{\beta}} \tag{A.4}$$

When calculating the equilibrium constant, the obvious assumption is that the mixture is at equilibrium and therefore, the second term can be grouped, and the exponents summed. Thus, Eq. A.4 becomes

$$K_p = \frac{[C]^{\eta} \cdot [D]^{\delta}}{[A]^{\alpha} \cdot [B]^{\beta}} RT^{\Delta n} \tag{A.5}$$

where Δn

$$\Delta n = \sum moles of Products - \sum moles of Reactants \tag{A.6}$$

and it can be stated that

$$K_p = K_c \cdot RT^{\Delta n} \tag{A.7}$$

Based on the above formulations, it can be seen that in order to obtain the equilibrium constant, information about both products and reactions must be know. This can sometimes be difficult especially when considering large systems of reactions at various states. Therefore a different formulation must be used where information of final states is not required.

The method used to calculate the reverse rates in the present work follows the Gibbs free energy approach. Gibbs free energy is a measure of the thermodynamic potential (or chemical potential) of an isobaric, isothermal system. The change in free energy of a reaction is given by

$$\Delta G = \Delta G^o + RT \ln Q \tag{A.8}$$

Where Q is the reaction quotient, ΔG^o is the standard-state Gibbs free energy at 1 atmosphere, and ΔG is the change in Gibbs free energy of the reaction. When the reaction reaches equilibrium, $\Delta G = 0$ and $Q = K_p$, thus we obtain an expression for the equilibrium constant as ,

$$K_{p_i} = \exp\left(\frac{-\Delta G_i{}^o}{RT}\right) \tag{A.9}$$

The Gibbs free energy change of a system (or reaction), is a state equation because is comprised of two state properties; Enthalpy and entropy. At standard-state (1 atmosphere)

$$\Delta G^o = \Delta H^o - T\Delta S^o \tag{A.10}$$

substituting Equation Eq. A.10 into Equation Eq. A.9, an expression for the pressure based equilibrium constant with respect to state functions can be shown to be

$$K_{p_i} = \exp\left(\frac{\Delta S_i^o}{R} - \frac{\Delta H_i^o}{RT}\right) \tag{A.11}$$

The changes of enthalpy and entropy respectively for a reaction are determined by

$$\frac{\Delta H_i^o}{RT} = \sum_{k=1}^{k} \alpha_{k_i} \frac{H_k^o}{RT} \tag{A.12}$$

$$\frac{\Delta S_i^o}{R} = \sum_{k=1}^{k} \alpha_{k_i} \frac{S_k^o}{R} \tag{A.13}$$

where alpha represents the number of moles of the specific compound in the reaction. The coefficient takes on positive values for products and negative values for reactants. In this study, the thermodynamic properties are assumed to be thermally perfect and therefore only depend on temperature. Therefore the standard state values are the values at temperature T and the individual contributions of enthalpy and entropy are determined using thermodynamic polynomials of the form

$$\frac{H_i^o}{RT} = a_{k1} + \frac{a_{k2}}{2} T_k + \frac{a_{k3}}{3} T_k^2 + \frac{a_{k4}}{4} T_k^3 + \frac{a_{k5}}{5} T_k^4 + \frac{a_{k6}}{T_k} \tag{A.14}$$

$$\frac{S_i^o}{R} = a_{k1} \ln T_k + a_{k2} T_k + \frac{a_{k3}}{2} T_k^2 + \frac{a_{k4}}{3} T_k^3 + \frac{a_{k5}}{4} T_k^4 + a_{k7} \tag{A.15}$$

From Eq. A.7 it is obvious that K_c does not equal K_p. This condition exists only when there is an equal number of mols for both reactants and products. Since CHOC utilises molar concentrations to calculate reaction rates, the K_c form is being considered. The reverse rate coefficient can be determined by

$$k_{r_i} = \frac{k_{f_i}}{K_{c_i}} \tag{A.16}$$

Although this equation is derived assuming equilibrium, it is a relation between the forward and reverse rate constants, and therefore holds in general for non-equilibrium conditions [7]. Using Eq. A.7, Eq. A.11, and Eq. A.16, the molar concentration based equilibrium constant can be expressed as

$$k_{r_i} = k_{f_i} \left[\exp\left(\frac{\Delta S_i{}^o}{R} - \frac{\Delta H_i^o}{RT} + \Delta n \ln\left(\frac{1}{RT} \right) \right) \right]^{-1} \tag{A.17}$$

The final formulation used was derived simply by substituting Eq. A.12 and Eq. A.13 into Eq. A.17 to yield,

$$\begin{aligned} k_{r_i} = k_{f_i} \Bigg[& \sum_{k=1}^{k} \nu_{k_i} a_{k7} - \sum_{k=1}^{k} \nu_{k_i} a_{k1} + \frac{T_k}{2} \sum_{k=1}^{k} \nu_{k_i} a_{k2} + \frac{T_k^2}{6} \sum_{k=1}^{k} \nu_{k_i} a_{k3} + \frac{T_k^3}{12} \sum_{k=1}^{k} \nu_{k_i} a_{k4} \\ & + \frac{T_k^4}{20} \sum_{k=1}^{k} \nu_{k_i} a_{k5} - \frac{1}{T_k} \sum_{k=1}^{k} \nu_{k_i} a_{k6} + \ln(T_k) \sum_{k=1}^{k} \nu_{k_i} a_{k1} + \Delta n \ln\left(\frac{1}{RT} \right) \Bigg]^{-1} \end{aligned} \tag{A.18}$$

Another good thing about this formulation is that the code can be modified to output the gibbs free energy as a function of time or temperature. this can be done to analyse a reaction mechanism and determine spontaneity of an individual reaction. or it can be done to determine the driving reaction without having to preform a a sensitivity analysis.

A.1 Validation

A simple test case is presented to validate the calculated reverse rates. The test case involves utilising a 0D combustion evolution of temperature for both the published reverse rates, and the reverse rates from the program. The reference data was obtained from [33].

Table A.1: Initial conditions

T_o[K]	P_o[atm]	Y_{H_2}	Y_{O_2}	Y_{N_2}
1200	1	0.029126	0.23301	0.73786

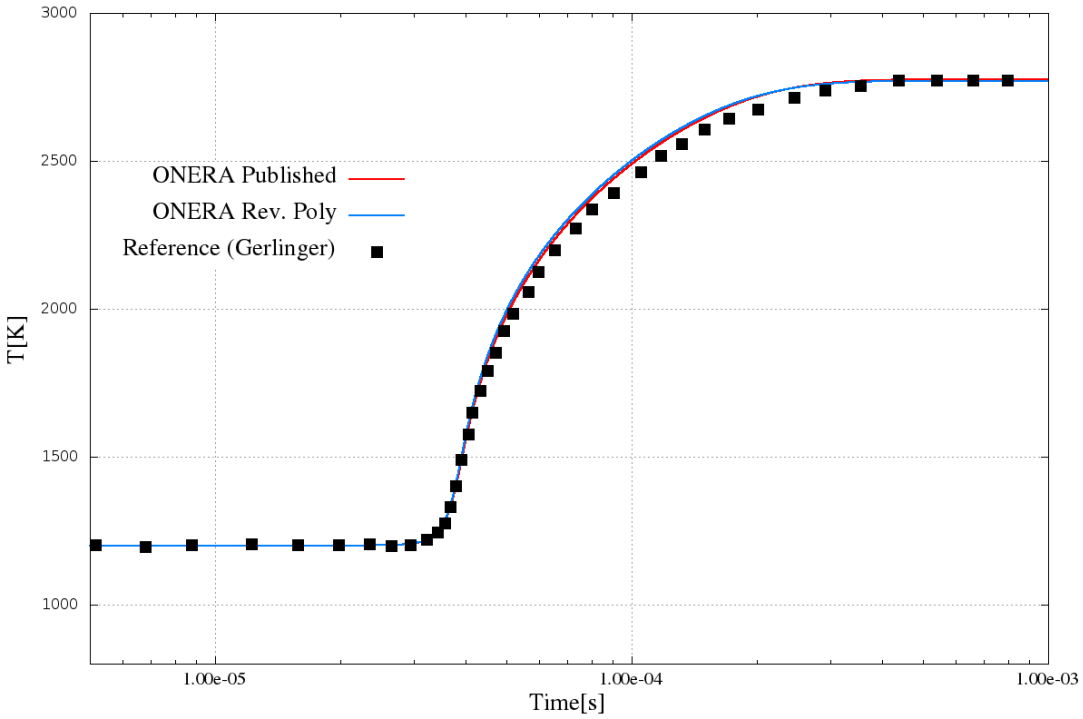

Figure A.1: Evolution of temperature comparing published vs calculated reverse rates